Summer 4-18-2021

GROWTH AND CHARACTERIZATION OF MOLECULAR FERROELECTRIC THIN FILMS

Yifan Yuan
University of Nebraska-Lincoln, yifan.yuan@huskers.unl.edu

GROWTH AND CHARACTERIZATION OF MOLECULAR FERROELECTRIC THIN FILMS

by

Yifan Yuan

A DISSERTATION

Presented to the Faculty of

The Graduate College at the University of Nebraska

In Partial Fulfillment of Requirements

For the Degree of Doctor of Philosophy

Major: Engineering

(Materials Engineering)

Under the Supervision of Professor Xiaoshan Xu

Lincoln, Nebraska

May, 2021

GROWTH AND CHARACTERIZATION OF MOLECULAR FERROELECTRIC THIN FILMS

Yifan Yuan, Ph.D.

University of Nebraska, 2021

Advisor: Xiaoshan Xu

Compared with inorganic ferroelectrics, organic ferroelectrics have advantages of low cost and low toxicity, are in increasing demand in capacitors, piezoelectric, and memory devices to reduce the environmental load. This work focuses on two types of organic molecular ferroelectric materials, croconic acid (CA) and 2-methylbenzimidazole (MBI). The work here introduces several origins of ferroelectricity in typical organics and their switching mechanism. We then investigated the nucleation, growth, and ferroelectric measurements of CA thin films. We explored the effect of substrate temperature and an external electric field on the nucleation and growth processes. The results can be used to improve the surface characteristics of ferroelectric films fabricated by the physical vapor deposition (PVD) method.

Next, we focus on the growth and electric measurements of MBI thin films. We realize the fabrication of MBI thin films by PVD in vacuum. By exploiting the extreme anisotropic growth of MBI crystals, a preferential crystalline orientation along (110) plane and one polarization axis along the out-of-plane direction are acquired. Finally, *in situ* electrical measurements are performed to gain insights into the amorphous-to-crystalline phase transition in MBI films.

ACKNOWLEDGMENTS

Time goes by so quickly. This long journey is fraught with difficulties, risks, and challenges. Sometimes it is hard to brace me up and see a promising future. But finally, I have made it with the support and assistance of many people in the process.

I would firstly like to express my deepest gratitude to my advisor Dr. Xiaoshan Xu for his excellent mentoring, professional advice, and patient guidance. His intelligence and profound knowledge taught me how to become a successful scientist and to do good research to benefit others. Moreover, his unparalleled diligence in working encourages me to work hard, and his noble virtue in life plays an exemplary role to instruct my behaviors and makes me recognize what a good advisor would look like. I am thankful to him for the opportunities he provided in my hard time, his tolerance for my inconsiderate mistakes, and how he makes me feel cared for. My gratitude knows no bounds.

I would secondly like to thank my committee members (Dr. Stephen Ducharme, Dr. Li Tan, and Dr. Jeffrey Shield) for instructing me through my dissertation, reviewing my dissertation, and giving me helpful comments. I would like to express my gratitude to Dr. Florin Bobaru for allowing me to work in his group.

I am also grateful for the help of my lab members, Jing, Yu Yun, Haohan, Detian, Xuanyuan, Corbyn, Yuanyuan, Xin, etc. It's a pleasant time to work and discuss with you. I also want to thank a lot of friends who helped me with my research and gave me advice in life.

Last but not least, I would like to thank my mother for her unreserved support of my academic pursuit, and lots of kind-hearted people, though not listed here, who have helped me in my journey.

Table of Contents

CHAPTER 1 INTRODUCTION

The promising role of inorganic ferroelectrics in the semiconductor electronics has long been recognized. Over the past two decades, with the advantages of being environmentally benign, mechanical flexibility, and low cost, the need for lead-free organic ferroelectrics has motivated some breakthroughs in these materials. These developments involve organic ferroelectrics with flexibility and easier synthesis method than their inorganic counterparts[1], and supramolecular ferroelectrics with non-covalent, reversible supramolecular interactions as dipole origins.[2] Some organic ferroelectrics are thermally robust up to approximately 380 K,[3] but the thermal stability of organic ferroelectrics is not as good as that of inorganics whose melting point can be larger than 1000 K (e.g., 1898 K for $BiTiO_3$).

The first organic ferroelectric crystal, known as Rochelle salt ($KNaC_4H_4O_6$), exhibits spontaneous polarization from the ordering of hydrogen bonds.[4] Hydrogen bonding drives molecules to form ordered assemblies; the reversible proton transfer between the hydrogen-donating molecule and the hydrogen-accepting molecule creates electrical dipoles. This mechanism inspired researchers to search for ferroelectricity in hydrogen-bonded organics, such as the recent efforts on croconic acid[5], 2-methylbenzimidazole[6] (MBI), and 3-hydroxyphenalenone[7] (3-HPLN) shown in Figure 1.1. As the interest in searching for ferroelectric molecular systems grows, it is increasingly necessary to understand the physical phenomena in organic ferroelectrics, such as the origins of ferroelectricity, switching mechanism, and negative capacitance.[8] The work presented here will focus on molecular organic ferroelectric and the self-assembly processes.

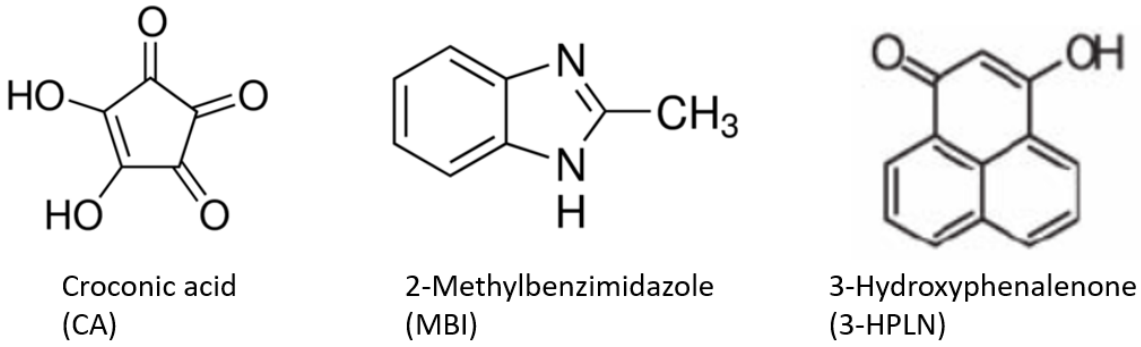

Croconic acid (CA) | 2-Methylbenzimidazole (MBI) | 3-Hydroxyphenalenone (3-HPLN)

Figure 1.1 Single-component organic ferroelectrics containing hydrogen bonds.

1.1 Organic Ferroelectrics

1.1.1 Introduction of Organic Ferroelectrics

The first example organic ferroelectric crystal, Rochelle salt, containing organic tartrate ions ($C_4H_4O_6^{2-}$) was discovered in 1920.[4] Compared with inorganic ferroelectrics, organic ferroelectric materials generally have smaller ferroelectric polarization and lower Curie temperature. For example, poly(vinylidene fluoride-trifluoroethylene) (PVDF-TrFE (70/30)) has a spontaneous polarization[9] ($P_s = 13$ μC cm^{-2}) and Curie temperature ($T_c \approx 122$ ℃, smaller than those[10] of $Pb(Zr_{0.52}Ti_{0.48})O_3$ ($P_s = 82$ μC cm^{-2}, $T_c = 450$ ℃). On the other hand, they have the advantages of lightness, flexibility, and non-toxicity which may lead to novel applications in organic electronics.

Among a large number of organics, ferroelectricity rarely occurs, even though their structures tend to be anisotropic with low lattice symmetry. Generally, there are three mechanisms that lead to ferroelectricity in organics, i.e., proton transfer, the relative displacement of charged entities, and permanent dipole reorientation. Proton transfer is also called hydrogen displacement. The first type of ferroelectricity, belonging to the order-disorder phase transition, is achieved by the proton transfer which occurs in the

crystalline state via a cooperative proton tautomerism mechanism (called prototrophy)[11]. The induced dipole moment originates from supramolecular interactions. Many organics have hydrogen bonds between molecules, such as common NH···O, OH···O, and NH···N hydrogen bonds. The transformation of hydrogen bonds via proton transfer may lead to a change of polarity. One example is the first single-component organic ferroelectric with above-room-temperature ferroelectricity, croconic acid, shown in Figure 1.2a, where polarity reversal is related to the cooperative transformation from OH···O bond to O···HO bond.[5] The combined hydrogen-bond network form the single polar axis which gives them the large remanent polarization P_r of 21 μC cm^{-2} and the coercive field E_c of about 14 kV cm^{-1} among organic ferroelectrics which are shown in Table 1. Good performance only occurred in single crystals which need repeated purification making them very costly. Another single-component ferroelectric example is 2-methylbenzimidazole (MBI) and 5,6-dichloro-2-methylbenzimidazole (DC-MBI) shown in Figure 1.2b, which use heterocyclic -N=C-NH- moieties in proton tautomerism. At room temperature, MBI single crystal has a remanent polarization as large as 5.2 μC cm^{-2} and the coercive field E_c of 11 kV cm^{-1}. Different from croconic acid, MBI has two polar axes which are from hydrogen bonds along either $[110]_{tetra}$ or the crystallographically equivalent $[1\bar{1}0]_{tetra}$ direction shown in Figure 1.2c. Polarity switching over two dimensions in MBI is significantly advantageous for the macroscopic polarization of randomly oriented polycrystalline thin films, compared with the uniaxial polarity of other organics.[6] DC-MBII single crystals at 373 K have a large remanent polarization of 10 μC cm^{-2} and coercive field of about 60 kV cm^{-1}. The high coercive field of DC-MBI reflecting the hard switching is due to the large hydrogen bond length.[11]

N···N distance (2.98 Å) in DC-MBI is longer than that in MBI (2.86 Å) and O···O distance in croconic acid (2.62 Å).

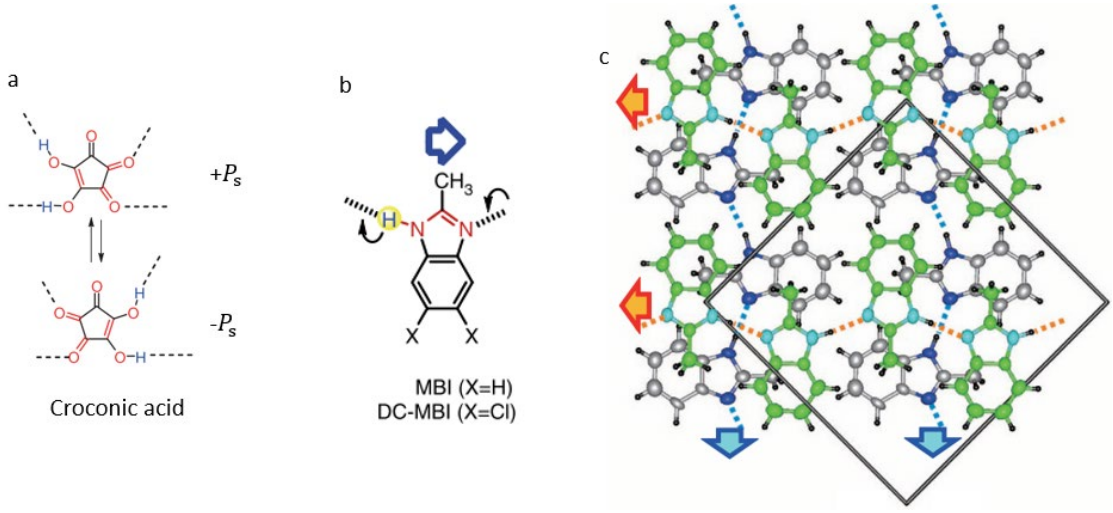

Figure 1.2 Molecular structure of (a) croconic acid ($H_2C_5O_5$), (b) MBI, and DC-MBI. (c) The crystal structure of MBI projected on the $(001)_{tetra}$ plane. Orange and blue arrows represent two directions of hydrogen bonds.[6]

The second origin of organic ferroelectricity is the relative displacement of charged entities in organics, also called charge-transfer complexes.[2] The mechanism is analogous to many displacive ferroelectric oxides, such as $BaTiO_3$. In the crystal, the multi-component molecule system is composed of electron donor (D) and acceptor (A) molecules. The charge transfer process results in a supramolecular dipole. When D and A are equally spaced apart, the mixed crystal is paraelectric with centrosymmetry, e.g., at high temperature. The relative movement of D and A with each other breaks the symmetry into pairs of D and A (dimerization), which results in intermolecular dipole moments. The most thoroughly studied system is the tetrathiafulvalene (TTF) complexes with p-chloranil (tetrachloro-p-benzoquinone; ChA) shown in Figure 1.3. At room

temperature, TTF-ChA co-crystals are paraelectric with a centrosymmetric structure. When the temperature decreases below 81 K for TTF-ChA, a Peierls transition ionizes the molecules to form DA dimers and changes the monoclinic lattice (space group $P2_1/n$) into a polar one (space group Pn).[4] No genuine *D-E* hysteresis loop has yet been reported because the CT complexes experience current-induced resistance switching to a low-resistance state, which would degrade spontaneous polarization.[12]

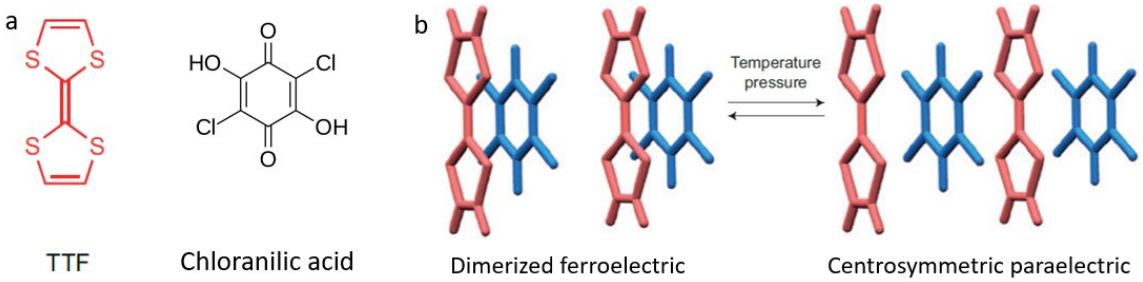

Figure 1.3 (a) Chemical structures of tetrathiafulvalene (TTF), chloranilic acid (ChA). (b) The canonical CT ferroelectric with alternated donor-acceptor dimers transitions into the paraelectric phase with centrosymmetric structure as temperature increases.[2]

Another origin of organic ferroelectricity is the reorientation of the intrinsic dipole of molecules. For example, the polymer polyvinylidene fluoride (PVDF) (CH_2–CF_2) and its copolymer with trifluoroethylene (TrFE) are the representative and the only commercially available organic ferroelectrics which are used in acoustic transducers and microphones.[13] The ferroelectricity in PVDF and P(VDF-TrFE) originates from the permanent dipoles of polar molecules associated with electropositive hydrogen atoms and electronegative fluorine atoms, which are switchable upon an external field, shown in Figure 1.4.[13] The molecular dipole moment can be rotated around the length of the polymer by an external field, producing polarization switching. Such dramatic

reorientation needs large energy resulting in the high coercive field. The typical copolymer P(VDF-TrFE 70/30) made by Langmuir-Blodgett deposition has a maximum spontaneous polarization P_s of 10 μC cm^{-2} and the coercive field E_c of about 9300±1000 kV cm^{-1}.

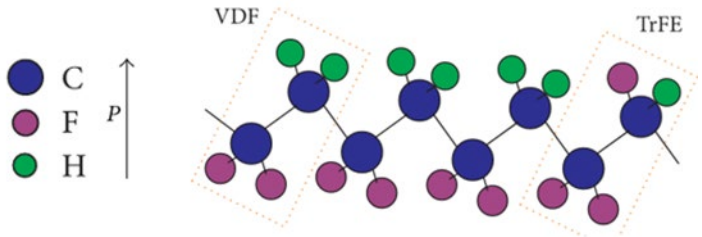

Figure 1.4 Schematic of molecular structure of P(VDF-TrFE) in the β phase.[13]

Table 1 Properties of purely organic ferroelectrics compared with inorganic compounds

Materials	P_r (μC cm^{-2}); temperature	Coercive field E_c (kV cm^{-1})
Organic molecules		
Croconic acid[5]	21; RT	14
MBI[6]	5.2; RT	11
DC-MBI[6]	10; 100 ℃	60
PVDF-TrFE (70/30)[9]	13; RT	50
3-HPLN[7]	3; RT	8-15
Inorganic compounds[1]		
$BaTiO_3$	26	10
$PbTiO_3$	50	5

In summary, the single-component organic ferroelectrics have a rather low dielectric

constant and spontaneous polarization. This is because their ferroelectricity is the side-effect of a ferroelastic or structural instability rather than dipole-dipole interaction such that they are classified as improper ferroelectrics where spontaneous polarization is not taken as the primary phase transition order parameter.

1.1.2 Polarization Switching Mechanism in Ferroelectrics

The switching behavior of ferroelectrics has been widely investigated to understand the kinetics of polarization switching, i.e., $P(t)$, which is very important for the different purposes of materials. The domain wall motion was formulated in $BaTiO_3$ by Mertz, etc..[14] Then based on domain nucleation and domain wall motion, many analytical models were created to describe the process of ferroelectric switching. The classical model describing the switching kinetics of single crystals is the Kolmogorov–Avrami–Ishibashi (KAI) model, which was based on the classical approach of nucleation and subsequent growth of reversed domains. Later, it was found that the KAI model could not explain the $P(t)$ behaviors of some polycrystalline PZT films where the switching kinetics are monitored in a broad time interval. To explain these behaviors, the nucleation-limited switching (NLS) model was developed by Tagantsev et al..[15] Here the existing models are summarized.

1.1.2.1 Kolmogorov-Avrami-Ishibashi (KAI) Model

When the electric field is applied on the ferroelectrics whose initial polarization direction is opposite the electric field, polarization starts from the nucleation of reversed domains, shown in Figure 1.5a, proceeds with the growth of domains in all directions, and finally saturates with the coalescence of domains. Usually, small nuclei of domains appear at the interfaces or grain boundaries. Defects and grain boundaries will impede the growth of

domain walls.

The basic idea of KAI model is that independent domain nuclei unrestrictedly grow under the applied field until they fill up the entire volume. Assuming τ_i as the typical waiting time of the elementary region, $1/\tau_i$ being the nucleation rate in the region (i) with the area S_i, the fraction of the region switched by time *t*, polarization *p*(*t*) is given by the obvious relation,

$$p(t) = 1 - \frac{\sum_{\mathrm{NS}} S_i}{\sum_{\mathrm{all}} S_i}, \tag{1.1}$$

where NS refers to nonswitch by time *t.*

The special case is that all the elementary regions are the same, i.e., $\tau_i = \tau$, $S_i = S$. Then the problem follows the classical decay equation for the number of nonswitched regions

$$dN_{\mathrm{NS}} = -N_{\mathrm{NS}} \frac{dt}{\tau}. \tag{1.2}$$

With the initial condition $N_{\mathrm{NS}} = N_0$ at $t = 0$, the solution is $N_{NS} = N_0 e^{-t/\tau}$, which leads to the KAI model for the case of one-dimensional growth,

$$p(t) = 1 - e^{-t/\tau}. \tag{1.3}$$

A general KAI model is written as[13]

$$P(t) = 2P_s \left\{1 - \exp\left[-\left(\frac{t}{t_0}\right)^{n_d}\right]\right\} \tag{1.4}$$

where P_s is spontaneous polarization, n_d is the dimensionality of domain growth, which for thin films can be taken as about 2, and t_0 is the characteristic switching time and a decreasing function of electric field.

KAI model applies for the case that only one domain nucleates and unrestrictedly

expands, or that many domain nuclei have the same switching time t_0. Using KAI model, several studies have succeeded explaining the $P(t)$ behavior in single crystals and epitaxial PZT films, where switching occurs in a 2-decade interval of time (Figure 1.5b).[15] It is also applicable to P(VDF-TrFE) copolymer films.[16] However, it fails when it comes to describe the behavior in polycrystalline PZT films where switching time has a broad distribution. Therefore, new models are created to give a reasonable description of polarization switching.

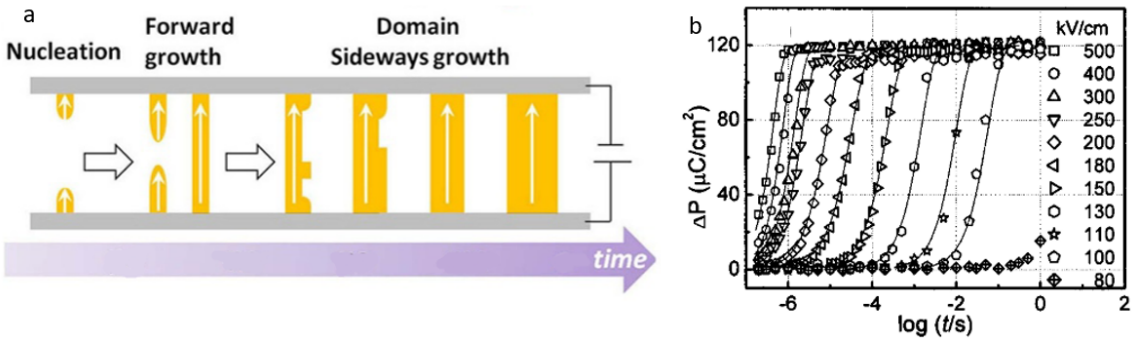

Figure 1.5 (a) General process of domain-mediated polarization switching. (b) The switching polarization in epitaxial PZT thin films at different electric fields and pulse widths. Solid lines are the fitting lines according to the KAI model.[16,17]

1.1.2.2 Nucleation-Limited Switching (NLS) Model

NLS model was firstly applicable to polycrystalline PZT films.[15] This model assumes the film consists of an ensemble of independent elementary region. The ensemble of regions has different nucleation waiting times which form a distribution function. The time dependence of polarization is written as

$$P(t) = 2P_s \int_{-\infty}^{\infty} \left\{1 - \exp\left[-\left(\frac{t}{t_0}\right)^{n_d}\right]\right\} F_d(\log\ t_0) d(\log\ t_0) \qquad (1.5)$$

where $F_d(\log\ t_0)$ is the distribution function for $\log\ t_0$ and meets the normalizing condition,

$$\int_{-\infty}^{\infty} F_d(\log\ t_0) d(\log\ t_0) = 1\ . \quad (1.6)$$

The distribution function has extended the applicability of the NLS model. The difference in the distribution functions leads to various switching behaviors. In particular, KAI model corresponds to the delta distribution function. The switching behavior of polycrystalline PZT films at different temperatures were explained by assuming the Lorentzian distribution function.[18] Gorbunov et al. also used the NLS model with a normal distribution to explain the behavior of trialkylbenzene-1,3,5-tricarboxamide (BTA) thin films.

1.2 Amorphous-to-crystalline phase transition

1.2.1 Crystallization mechanisms

Self-assmebly of organic molecules involves the process in which molecules spontaneously organize into large ordered domains e.g. monolayers on the surface. The interaction between molecules and the surface can be strong through a strong affinity of the head group of molecules to the surface, such as thiols on Cu substrates. Such systerm is termed as self-assembled monolayers (SAM).[19] In this thesis, we will focus on the system where molecules do not interact strongly with the substrate, and they can assemble into supramolecular networks.[20]

An amorphous or non-crystalline solid can be produced by fast cooling of liquid (Figure 1.6a). At sufficiently low cooling rate, usually the crystalline solid is formed. The fundamental difference between amorphous solids and crystals is in the basic nature of

their microscopic structure. The molecules in the crystals are positioned periodically exhibiting long-range order, but the equilibrium positions of the molecules in amorphous solids are strongly disordered. Amorphous phases can also be prepared by condensation on cold surface from the vapor phase (Figure 1.6b). When a vapor stream formed within a chamber by thermal evaporation of a source, impinges upon the surface of cold substrate, atoms or molecules are quenched on the surface before they can migrate to crystalize.

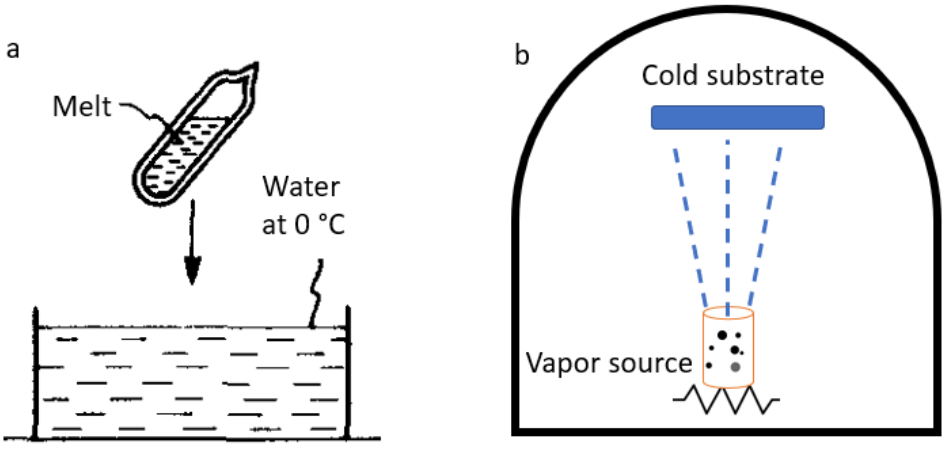

Figure 1.6 Amorphous solids from (a) liquid phase and (b) gas phase.

Crystallization from amorphous solids or glasses is of great importance in the formation of glass ceramics[21] and to obtain ultrafine grained microstructure with desired properties in alloys[22]. Not all amorphous solids can crystallize. The amorphous state is ubiquitous: nearly all materials can form glass if cooled fast enough, but for some traditional “glass formers”, (e.g., organic polymer) crystallization is difficult due to considerable complexity on a molecular scale[22]. The topological constraints, such as polymer chains having bulky dangling sidegroups, prevent molecules from being in

crystalline configuration. The crystallization process involves the formation of crystal nuclei and their subsequent growth. It can be well described by classical nucleation theory[23].

Nucleation starts with some building units coalescing as nanometer-sized areas. Nucleation can be either homogeneous inside the phase volume or heterogeneous at some sites on external surface or impurities. Nuclei can either dissociate by thermal motion if smaller than the critical size (Figure 1.7a) or continue to grow if larger than the critical size[24]. The thermodynamic driving force for this process is caused by undercooling, and the resultant energy barrier for homogeneous nucleation[24] is,

$$\Delta G^* = \left(\frac{16\pi\sigma^3 T_x^2}{3L_v^2}\right)\frac{1}{\Delta T^2} \tag{1.7}$$

where σ is the interfacial energy, T_x the phase transition temperature, L_v the latent heat, and ΔT the temperature difference of undercooling. In contrast to the nucleation from a liquid phase, nucleation from the amorphous phase is slower due to the low atomic mobility and the crystallization can be interrupted at any transformed fractions[22].

The growth of nuclei is achieved by adding more atoms or molecules on the nuclei. Growth rate increases with the increase of temperature due to enhanced diffusion length. In terms of amorphous thin films, its crystallization, e.g. from the amorphous solid water, can proceeds by a “top-down” mechanism[25], i.e., nucleation appears preferentially at the vacuum interface rather than at the substrate interface, and growth front propagates faster than bulk nucleation (Figure 1.7(b)). It is likely because the surface molecules have higher mobility than those in the bulk.

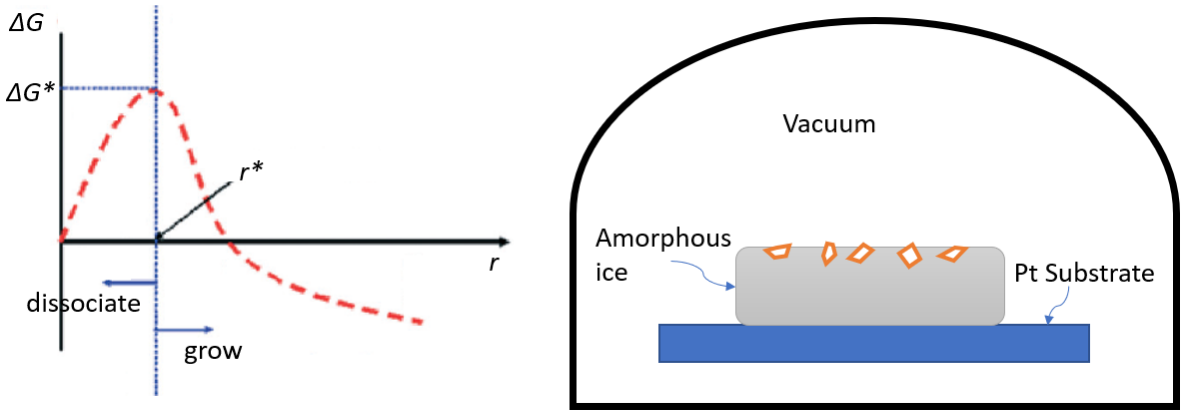

Figure 1.7 (a) Plot of the free energy (Gibbs' thermodynamic potential), Δ*G*, versus cluster radius, *r*. Δ*G** = max determines the radius of the critical nucleus *r**. (b) Schematic of the crystallization of amorphous ice.[23]

Except through classical theory, the self-assembly of organic molecules is also described by the nonclassical mechanisms. For example, the growth of DL-glutamic acid monohydrate[26] proceeds through the attachement of preformed nanoscopic species from solution and subsequent transformation into crystalline 2D nuclei that finally builds new molecular layers by further monomer incorporation. Its scheme is shown in Figure 1.8.

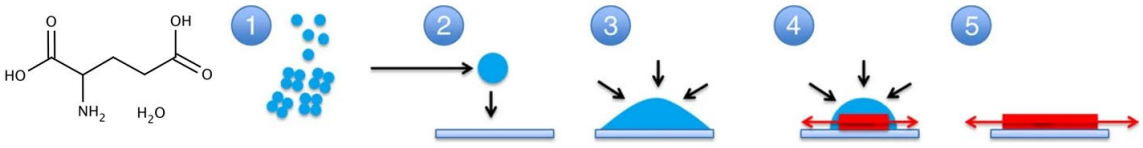

Figure 1.8 The growth of DL-glutamic acid monohydrate undergo 5 stages, 1) the aggregation of prenucleation clusters into large nanodroplets; 2) the attachment of droplets on the surface; 3) spread of droplets; 4) the transformation into 2D nuclei; 5) the growth of a new molecular layer.[26]

1.2.2 Kinetics of nucleation and phase transition

Steady-state nucleation rate

The amorphous phase can be viewed as a highly undercooled liquid with large viscosity. In spite of its large driving force from undercooling for crystallization, the nucleation rate is also restricted by atomic mobility. The nucleation rate for homogeneous nucleation is therefore given by[24]

$$I(T) = v^{*+}C^* = \omega C_0 \exp\left(-\frac{\Delta G_m}{k_B T}\right)\exp\left(-\frac{\Delta G^*}{k_B T}\right) \text{ nuclei m}^{-3}\text{s}^{-1} \qquad (1.8)$$

where v^{*+} is the attachment probability to the clusters of critical size, C^* the concentration of critical-sized nuclei, $C^* = C_0 \exp(-\Delta G^*/k_B T)$, ω is a factor related to atomic vibration frequency and the area of the critical nucleus. C_0 the number of atoms per unit volume, k_B the Boltzmann constant, ΔG_m the activation energy of atomic migration, which is assumed independent of temperature, and ΔG^* the nucleation barrier. The term $\exp\left(-\frac{\Delta G_m}{k_B T}\right)$ is essentially the atomic mobility and the term $\exp\left(-\frac{\Delta G^*}{k_B T}\right)$ is the potential concentration of nuclei. As shown in Figure 1.9, the nucleation rate varies nonlinearly with the temperature. At extreme low temperature, nucleation rate is negligible because diffusion is too slow, whereas at high temperature close to the equilibrium transition temperature I is also negligible due to small driving force.

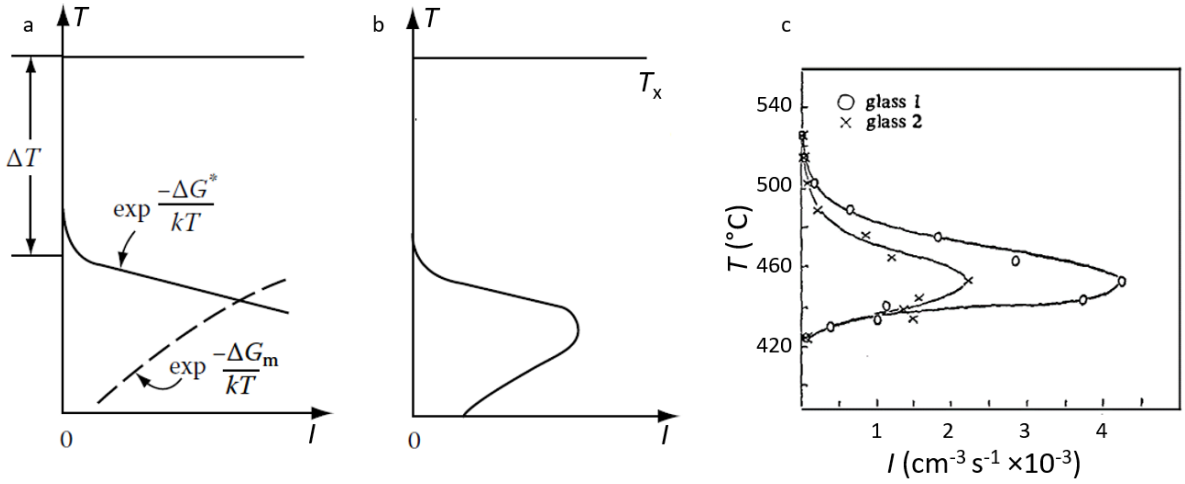

Figure 1.9 (a) The two exponential terms determine the nucleation rate I in (b).[24] (c) Steady state nucleation in two kinds of glass as a function of temperature.[21]

Evidence of this nonlinear relationship between I and T is shown in the system of crystallization from lithium silicate glasses[21] (Figure 1.9c). The maximum-nucleation-rate temperature (≈450 °C) is close and higher than the glass transition temperature (T_g≈410 °C).

Non-steady-state nucleation rate

The above discussion is limited to steady state nucleation rate. Actually, during the whole nucleation and growth process, steady-state nucleation only occurs for a short period of time with the conditions that the system must be large enough and supersaturation and/or undercooling are only affected by nucleation in the nearest proximity of nuclei. Before reaching steady-state nucleation, there exist transition periods of non-steady-state nucleation process which are explored by many researchers[27,28]. As shown in Figure 1.10, the nucleation rate is a function of time, reaching steady state gradually. The physical picture behind this process according to classical nucleation

theory (CNT) is that: at a specific instant with undercooling ΔT, there is an equilibrium size distribution of clusters which corresponds to different free energy in the system (Figure 1.7a), e.g., for spherical nuclei, $\Delta G(r) = \frac{4\pi\sigma}{3}(3r^2 - \frac{2r^3}{r^*})$, where r^* is the critical cluster size. The equilibrium size distribution is given by the equation,

$$C(n) = C_1 \exp\left(-\frac{\Delta G(n)}{k_B T}\right) \tag{1.9}$$

where C_1 is the number of single atoms in the equilibrium system, n the number of molecules for a cluster, $C(n)$ the equilibrium concentration of clusters of size n. When new undercooling is established in the system, cluster size distribution has to change. Larger clusters take more time to emerge than small ones. A new set of steady-state size distribution consisting of subcritical and critical clusters is inherited from the previous one. The transient distribution function $c(n,t)$ satisfies the partial differential equation[27]:

$$\frac{\partial c(n,t)}{\partial t} = \frac{\partial\left\{v_n^+ C(n) \dfrac{\partial\left[\dfrac{c(n,t)}{C(n)}\right]}{\partial n}\right\}}{\partial n} \tag{1.10}$$

where v_n^+ is the probability for the attachment of a molecule from the amorphous phase to the surface of a crystal of size n.

Once the solution $c(n,t)$ is found, the transient nucleation rate $J(n,t)$ can be obtained by the expression,

$$J(n,t) \cong -v_n^+ C(n) \frac{\partial\left[\dfrac{c(n,t)}{C(n)}\right]}{\partial n} \tag{1.11}$$

Kashchiev[27] derived an approximate analytical solution with avoiding assumptions which concern the physical picture of the process. The non-steady nucleation rate he obtained is:

$$J(n,t) = I\left[1 + 2\sum_{l=1}^{\infty}(-1)^{i}\exp\left(-\frac{i^2 t}{\tau_{\mathrm{N}}}\right)\right] \tag{1.12}$$

where I is the steady-state nucleation rate, and τ_{N} is called the induction time which reflects the speed for the system to reach steady state. The integration of Eq. (1.12) leads to $c(t)$ which can be easily measured from the experiments. As shown in Figure 1.10a, the experimental points agree well with the theoretical curve.

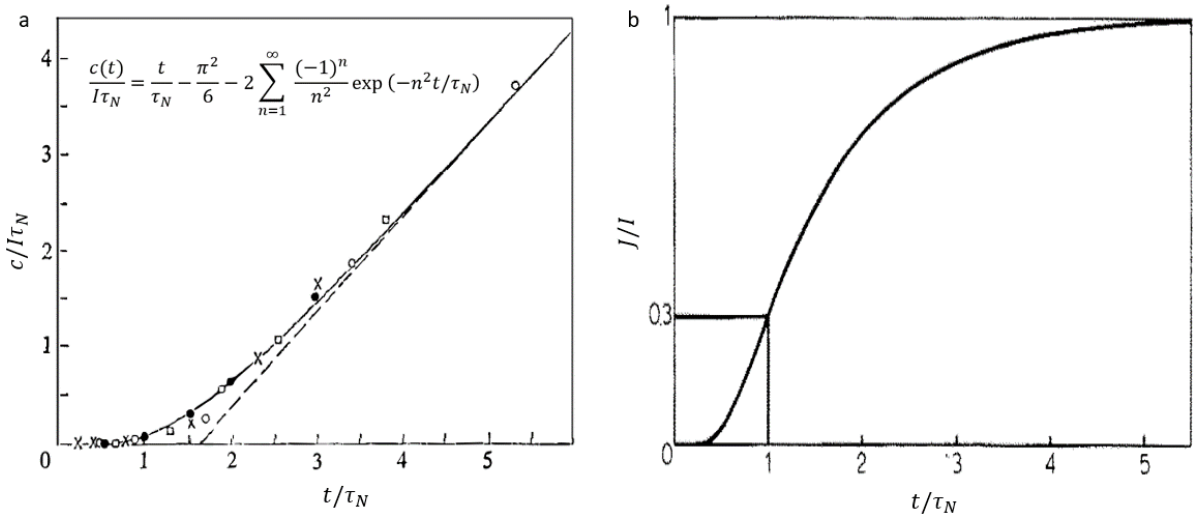

Figure 1.10 (a) Comparison of experimental nuclei density as a function of time with the theory of transient nucleation. (b) Theoretical nucleation rate as a function of time.[21]

The induction time of the system depends significantly on the attachment probability v^{*+} to the clusters of critical size by the equation,

$$\tau_{\mathrm{N}} = \frac{8k_{\mathrm{B}}T}{\pi^2 \lambda v^{*+}} \tag{1.13}$$

where $\lambda = -[\mathrm{d}^2\Delta\mathrm{G}(n)/\mathrm{d}n^2]_{n=n^*} > 0$. The attachment probability v^{*+} is much different for various system. Therefore, the induction time can be several milliseconds in solidification of liquid but may be years in glass crystallization. According to

Kashchiev's deduction,

$$\tau_{\mathrm{N}} = \frac{16}{\pi^2} \cdot \frac{ha^2\sigma}{V^2(\Delta G_{\mathrm{V}})^2} \exp\left(\frac{\Delta G_m}{k_{\mathrm{B}}T}\right) \tag{1.14}$$

$$v^{*+} = \frac{k_{\mathrm{B}}TV_f^2(\Delta G_{\mathrm{V}})^2}{2\lambda ha^2\sigma} \exp\left(-\frac{\Delta G_m}{k_{\mathrm{B}}T}\right) \tag{1.15}$$

where h is the Planck's constant, a the jump distance of an atom, σ the interfacial energy per unit area, V_f the volume occupied per formula unit, and ΔG_{V} the difference between free energy of the mother phases and crystal phases per unit volume. The temperature dependence of τ_{N} is mainly determined by the exponential term, so at high temperature the induction time will be small. ΔG_{V} varies with temperature, $\Delta G_v = \frac{L_v \Delta T}{T_x}$, but its effect on τ_{N} is much smaller than the exponential term. By plotting $\log(\tau_N \Delta G_v^2)$ against $1/T$, the value of ΔG_m can be obtained. James[21] showed that the relation between experimentally measured τ_{N} and T can be described fairly accurately by Eq. (1.14).

Following the steady-state nucleation, nucleation driving force ($\Delta\mu \approx L_{\mathrm{V}}\Delta T/T_{\mathrm{x}}$) and nucleation rate constantly drop due to the growth of nuclei. Experimentally, it was *in situ* observed in the electron microscope that the nucleation density increases initially, saturates for a short time, and then decreases due to coalescence of clusters as time proceeds[29].

Kinetics of phase transformation

Except the nucleation rate, the rate of phase transformation, i.e., the relation between the fraction of the transformed assembly and the time also attracts much attention. The theory of transformation involving nucleation and growth is applicable to many systems regardless of different mechanisms of transformation, such as order-to-disorder transition

(ferroelectric-to-paraelectric), single phase change (recrystallization), etc.

The physical picture of transformation includes the incessant nucleation in untransformed region, the growth of nuclei and the impingement of transformed regions. The theoretical purpose is to establish the relation between transformed volume fraction f and time *t*. Before we proceed to formulate the process, some basic assumptions have to be made:

1. The growth rate in any dimension of the transformed cluster is constant at constant driving force. It is confirmed experimentally in polarization reversal[30,31] (known as Mertz's Law), and other reactions where the composition of new phase is the same as that of the mother phase[32].
2. The growth rate of nuclei, Υ, is isotropic so that the shape of nucleus is spherical for three-dimensional growth.
3. The reaction is homogeneous, i.e., the nucleation rate is the same in all parts of untransformed regions.

Suppose that the transformation starts at time $t = 0$, and the untransformed volume of the mother phase is V^{α}. After the first short time $t = \Delta t_1$, a number of nuclei appear from the untransformed volume with the steady-state nucleation rate *I*, so the number of nuclei is $IV^{\alpha}\Delta t_1$. The transformed volume at time *t* due to the growth of one nucleus originating at time $t = \Delta t_1$ is $v_r = \left(\frac{4\pi}{3}\right)\Upsilon^3(t - \Delta t_1)^3$ and the total transformed volume for those nuclei is $v_r IV^{\alpha}\Delta t_1 = \left(\frac{4\pi}{3}\right)\Upsilon^3(t - \Delta t_1)^3 IV^{\alpha}\Delta t_1$. In the initial stage of transformation, the mutual interference of nuclei is negligible since the untransformed region is much larger than transformed region, so the total volume of transformed region at time *t* resulting

from the growth of clusters nucleated at numerous time intervals is

$$V^{\beta} = \left(\frac{4\pi}{3}\right)\Upsilon^3 \sum_{i=1}^{n}\left(t - \sum\nolimits_{j=1}^{i}\Delta t_j\right)^3 IV^{\alpha}\Delta t_i$$
$$= \left(\frac{4\pi}{3}\right)\Upsilon^3 \sum_{i=1}^{n}(t-\xi_i)^3 IV^{\alpha}\Delta t_i$$

where ξ_i is the time within Δt_i. With $\max(\Delta t_1, \Delta t_2, \ldots, \Delta t_n)$ infinitely small, the transformed volume can be written as

$$V^{\beta} = \left(\frac{4\pi}{3}\right)\Upsilon^3 \int_0^t IV^{\alpha}(t-\tau)^3 d\tau\,. \tag{1.16}$$

To treat the process more exactly, the mutual impingement of different regions has to be considered since it must happen in all transformations after a long time. Avrami treated this geometrical problem by introducing the concept of an "extended" transformed volume with the only assumption of random distribution of nuclei centers throughout the volume regardless of the shape[33]. The extended volume which is the independently transformed volume unaffected by the impingement is defined by the relation,

$$V_e^{\beta} = \left(\frac{4\pi}{3}\right)\Upsilon^3 \int_0^t IV(t-\tau)^3 d\tau \tag{1.17}$$

where $V = V^{\alpha} + V^{\beta}$. V_e^{β} is also called the phantom regions because the nucleation within the transformed region is considered as well. V_e^{β} may be larger than the total volume of the material *V*.

Based on the assumption that nucleation is random, Avrami derived the relation between the actual transformed volume V^{β} and the extended volume V_e^{β} in the form

$$\frac{V_e^{\beta}}{V} = -\ln\left(1 - \frac{V^{\beta}}{V}\right). \tag{1.18}$$

Combining Eq. (1.17) and (1.18), the transformed volume fraction in general cases is

$$f = \frac{V^{\beta}}{V} = 1 - \exp\left[-\frac{4\pi}{3}\Upsilon^3 \int_0^t I(t-\tau)^3 d\tau\right] \tag{1.19}$$

It is obvious that nucleation rate has significant effect on the transformation fraction and in different circumstances the nucleation rate has distinct variations. For example, in small undercooling, nucleation could only be activated at some preferential sites, such as grain boundary, interface. Those sites for heterogeneous nucleation with limited number are exhausted gradually so that nucleation rate is decreasing with time. Avrami supposes that if the concentration of initial sites is N_0 and the number of sites decay exponentially by the relation $N(t) = N_0 \exp(-vt)$, where v signifies the decay rate of sites, the nucleation rate can be written as

$$I(t) = -\frac{\mathrm{d}N}{\mathrm{d}t} = N_0 v \exp(-vt). \tag{1.20}$$

Combining $I(t = \tau)$ with Eq. (1.19) produces

$$f = 1 - \exp\left\{-\left(\frac{4\pi N_0 \Upsilon^3}{3}\right)\left[t^3 - \frac{3}{v^3}(v^2t^2 - 2vt + 2) + \frac{6}{v^3 \exp(vt)}\right]\right\} \tag{1.21}$$

We can discuss two cases about this equation. When potential nucleation sites exhaust very fast, i.e., v is very large, Eq. (1.21) is approximately

$$f = 1 - \exp\left\{-\left(\frac{4\pi N_0}{3}\right)\Upsilon^3 t^3\right\}. \tag{1.22}$$

The transformation proceeds approximately with the third power of t. Avrami proposed a simple generalized equation for application,

$$f = 1 - \exp(-kt^{n_d}) \tag{1.23}$$

where n_d is named as the Avrami exponent[34]. Actually, as long as *v* is larger than zero, n_d is always less than 3 because $\left[t^3 - \frac{3}{v^3}(v^2t^2 - 2vt + 2) + \frac{6}{v^3\exp(vt)}\right] < t^3$ in Eq. (1.21). On the other hand, if the sites decrease slowly with small v, smaller *v* results in smaller n_d.

Another general assumption which is practical in some film depositions[29] is that initially N_{n0} nuclei preexist at $t = 0$ and the nucleation rate is some decreasing function of time, $I(t) = k_0/t^{n_d}$. In this case, Eq. (1.19) can be reduced to

$$f = 1 - \exp\left[-\frac{4\pi}{3}\Upsilon^3(N_{n0}t^3 + k_0t^{4-n_d})\right]. \quad (1.24)$$

In this case, the Avrami exponent $3 < n_d < 4$.

CHAPTER 2 METHODS

This chapter describes the experimental methods exploited in this thesis, including the characteristics and the underlying principles of the instruments. All the methods can be categorized into two parts: the fabrication methods of samples and characterization techniques for them. We begin with section 2.1 describing details of the physical vapor deposition method in this thesis. Section 2.2 includes atomic force microscopy, crosse-polarized optical microscopy and laser scanning microscopy to characterize the morphology of organic thin-film samples, and x-ray diffraction technique for structural characterization. Then this chapter ends with the description for methods of in situ electrical measurements for ferroelectric materials, including displacement-voltage loops, double wave method, current-voltage curves, and impedance measurement in section 2.3.

2.1 Physical Vapor Deposition

Some common techniques to fabricate organic thin films include spin coating, chemical vapor deposition (CVD), and physical vapor deposition (PVD). Spin coating is a procedure in which a small amount of solution including organic deposits and volatile solvent is put on the substrate center, then rotation of the substrate at high speed spreads the solution into uniform films. The thickness of the film depends on the rotation speed, viscosity of the solution and surface tension. CVD is a family of processes whereby materials is deposited on the substrate by a chemical reaction of vapor on or in the vicinity of the substrate under low pressure of 0.1 to 100 torr. Chemical reactions can be caused by resistive heating, plasma, or laser with continuous flow of gaseous reactants.

PVD is characterized by a process in which a solid phase is converted to the vapor phase by sublimation or sputtering in vacuum, then condensed onto substrates. Compared with other coating processes, the high vacuum, gives PVD method a much cleaner environment. Even if the source consists of a small number of impurities, different sublimation temperatures can be exploited to minimize impurities from depositing onto the substrate.

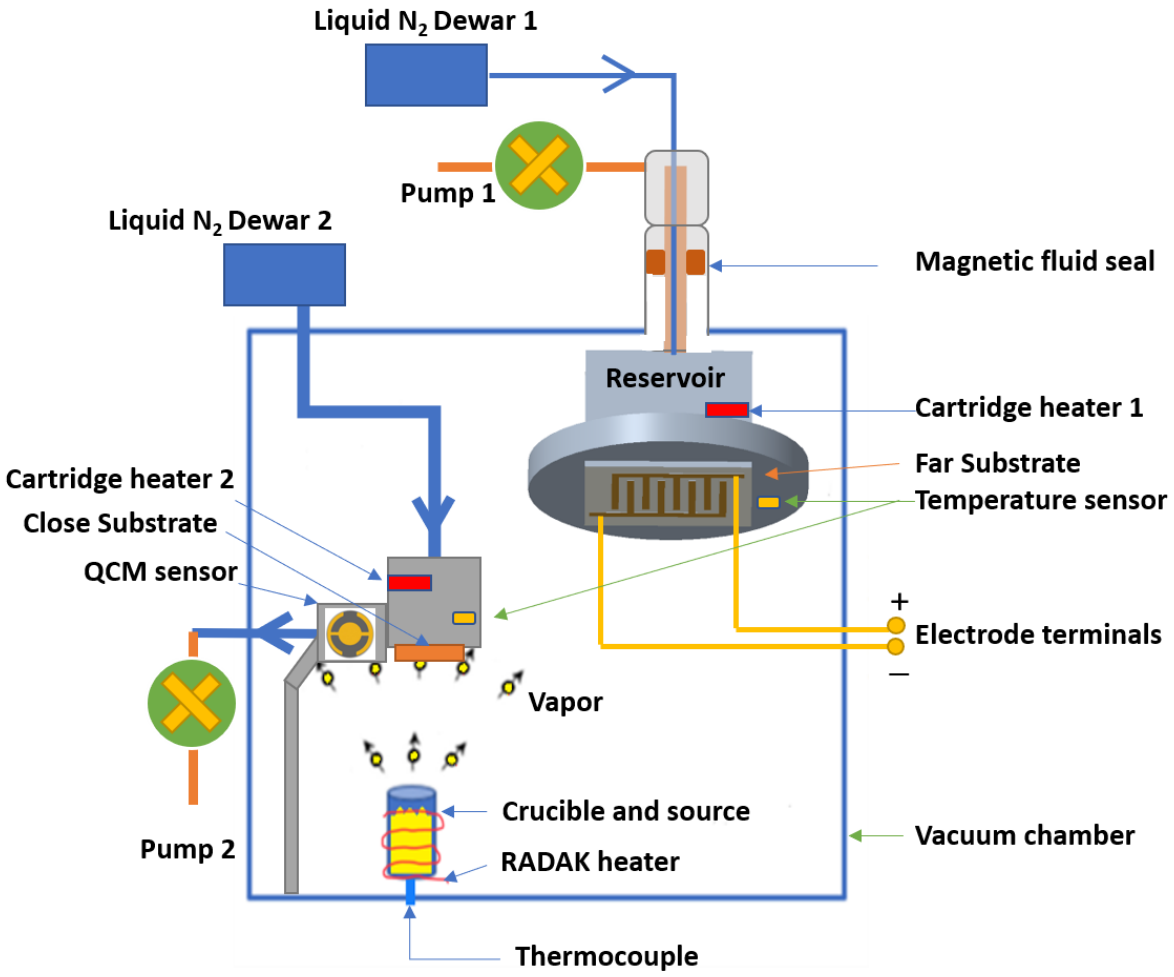

Figure 2.1 The schematic of PVD setup in this thesis.

In this thesis, the EvoVac PVD platform was used for the thermal evaporation.

Organic materials usually have lower melting point than inorganics. Therefore, uniform and precise heating is required for deposition of organics. LUXEL RADAK heater can increase temperature up to 1500 °C with the precision better than 0.2 °C, suitable for organics. As shown in Figure 2.1, the crucible containing an organic source is heated by the RADAK furnace and an integrated K-type thermocouple provides precise temperature feedback to the Watlow EZ-ZONE controller which utilizes proportional–integral–derivative (PID) algorithm to stabilize the temperature within 0.2 °C. When the solid organic source are heated over the sublimation point under high vacuum of less than 1×10^{-6} Torr, molecular beams are generated, followed by deposition onto the substrates. As a common practice, source materials are often degassed at around 100 °C to remove moisture due to the previous exposure to the air.

Since the substrate temperature plays an important role in the quality of films[29], it is also controlled accurately in our experiments by the cooling system. In Figure 2.1, the substrate can be put at two positions, “Close Substrate” and “Far Substrate”. Compared to the far substrate, the substrate near the source is used to grow films with large thickness where its molecular beam flux is six times (0.12 Å/s for croconic acid) higher than that at far position (0.02 Å/s for croconic acid). The two substrate locations use two separate cooling systems, which consist of the same components: a liquid nitrogen (LN2) Dewar, pipelines, a reservoir, a heater, a temperature sensor, and a pump. In principle, cooling is implemented by drawing liquid nitrogen which is stored in a 20L Dewar through the reservoir by a pump (Instec, Inc.). The pump itself has a band heater wrapped around its inlet to protect from freezing. The cartridge heater of 50 W power can assist liquid nitrogen to control temperature precisely in the range 100 - 350 K. A platinum RTD

sensor (Cryo-Con XP-100) is used to monitor substrate temperature. Combined with heater and temperature sensor, the temperature controller (Lakeshore 335) can stabilize the temperature within 0.5 °C. As a built-in function, the EvoEvc system has the rotation mechanism for the far substrate position. A magnetic fluid seal provides dynamic sealing action between the feedthrough (rotor) and the chamber (stator) which allows simultaneous cooling and rotation.

During the deposition process, the thickness of the film and the deposition rate can be monitored by the INFICON quartz crystals of 6 MHz. It is a quartz crystal microbalance (QCM) which in fact measures the real-time variation of frequency of a quartz crystal resonator. When an alternating current is applied to the quartz disk, it will oscillate at its resonance frequency due to the piezoelectric effect. The deposits will cause the mass change in QCMs, which is linearly related to the change in resonance frequency by the equation[35]

$$\Delta f = -\frac{f_0^2}{F_q \rho_q} \frac{\Delta \mathrm{m}}{\mathrm{A_{el}}} \tag{2.1}$$

where f_0 is the resonance frequency of the unperturbed quartz resonator, F_q the frequency constant of the crystal, ρ_q the quartz density and A_{el} the electrode area. The frequency of quartz can be measured with a precision of 0.01 Hz in a vacuum, so nanograms of mass and angstroms of thickness can be measured. On the other hand, since the resonance frequency is also affected by the temperature, the quartz monitor crystal is connected to water cooling system.

Water cooling is suitable for the deposition of most organics. However, in view of the small sticking factor of some organic molecules at room temperature due to its low

melting temperature, the sensor has to be cooled to a lower temperature by liquid nitrogen. As shown in Figure 2.1, in our experimental setup, the QCM sensor is connected with the reservoir so that it can be kept at the same low temperature down to 100 K with the substrate.

The measured thickness from the QCM sensor has to be calibrated with the actual film thickness. Then the correct tooling factor is entered into the device. The tooling factor is calculated by $F_m = F_i t_a / t_i$, where F_i is the original tooling factor, t_a the actual thickness which can be measured by the surface profiler, t_i the thickness indicated by QCM. When all the sensed parameters including the deposition rate, source temperature, substrate temperature and chamber pressure are incorporated into one LabVIEW program, we can control the deposition process by different parameters. For example, usually at a specific temperature, deposition rate will decrease as the source in the crucible is consumed gradually. If a constant deposition rate is required, we can use a LabVIEW program to control the source temperature with reference to the deposition rate.

2.2 Characterization methods for film morphology and structure

2.2.1 Atomic Force Microscope

The atomic force microscope (AFM) has much higher resolution, down to fractions of a nanometer than optical microscope. Other microscopies use photon, electron, etc. to produce image, and AFM is a scanning probe which produces image by the interaction between a tiny tip and the surface atoms.

The principles of topological imaging in an AFM are shown in Figure 2.2. AFM works by running the ultra-fine needle tip over the sample surface. The interaction

between tip and surface leads to a bending of cantilever. The deflection of the reflected laser is measured by the four-quadrant photo detector known as Position Sensitive Detector (PSD). The system records the topography for each scan line. Multiple scan lines are combined to produce one image with three-dimensional topography. Depending on the force between the tip and the surface, such as mechanical contact force, van der Waals forces, electrostatic forces, and magnetic force, etc., there are several operation modes. Here, we elaborate on three basic imaging modes: contact mode, tapping mode and non-contact mode.

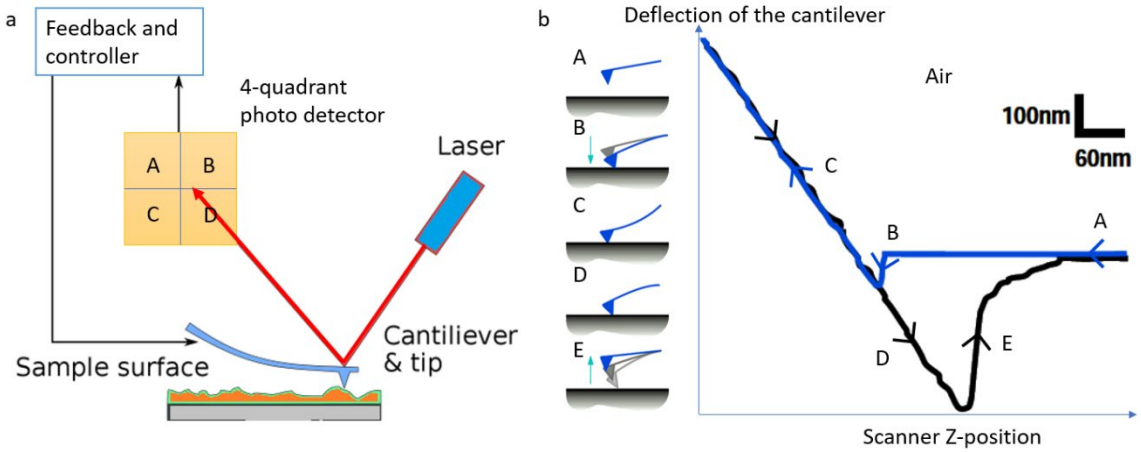

Figure 2.2 (a) Schematic drawing of the AFM. (b) Measurement of the forces between an AFM tip and a mica surface in air.[36]

Contact mode

In contact mode, which is the basis for all AFM techniques, one imaging method is to keep a constant force on the cantilever tip, i.e., constant force mode. An adjustment to the tip to maintain a specific deflection of the tip is used to display an image. When the tip is approaching in the vicinity of the surface atoms, firstly it is drawn by an attractive force and then pushed up by a repulsive force. For example, in Figure 2.2b, the tip is

approaching a mica surface in air starting from (A) point.[36] As the tip is very close to the surface, ~10 nm, it jumps down (B) as it feels a large adhesive force due to capillary forces from the liquid contamination layer on the surface. Once the tip touches the surface, the deflection increases (C) as the fixed end of the cantilever continues falling down. When a desired force is achieved, the tip is pulled off the surface and the adhesion formed during contact causes a large deflection (D) at some distance past the initial contact point. When the scanner on which the cantilever is fixed arrives point (E), the adhesion is disconnected, and the tip is free from the surface. Figure 2.2b is known as a force curve, actually showing "PSD voltage versus scanner position and PSD voltage can be converted into a deflection distance. The contact force can be calculated from the deflection d_D through the equation, $F = kd_D$. The spring-constant k of the cantilever is known from the manufacturer. The force is usually in the scale of nanonewton which is enough to dent the surface of some soft organic materials.

Force curve is very useful for the selection of an appropriate deflection setpoint. To clarify the point, firstly we need to understand the role of the setpoint. In constant force mode (i.e., the system tries to maintain constant deflection value), when the scanner moves along x-y grid over the sample, the deflection values of the tip due to the surface height variations is changed. The feedback loop using deflection values as input signals adjusts the height of the scanner (z value) to maintain a constant deflection value which is defined by the user as the deflection setpoint. A force curve can exhibit intuitively the relation between the total force applied onto the sample and the setpoint. In Figure 2.3, when the tip touches the sample, i.e., the scanner is at Z_0 position, the total force on the sample has two sources, one is from the pressure of the tip, the other from the adhesion

force. It is the sum of spring force and adhesion force. The deflection setpoint from the user's input determines the amplitude of the spring force. Large setpoint voltage will bring the scanner close the surface, lead to high spring force and may result in the damage of the surface and contamination of the tip. Therefore, a proper setpoint is selected to minimize the cantilever spring force and can be visualized from the force curve in Figure 2.3.[36]

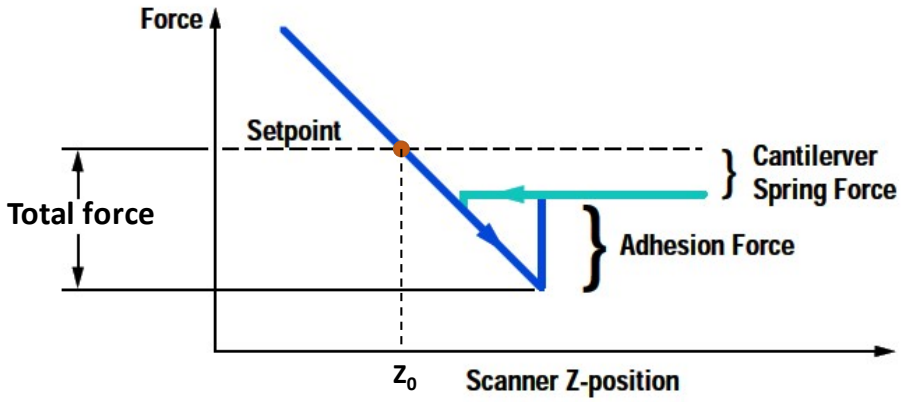

Figure 2.3 Schematic of AFM force measurement

Tapping mode

In contact mode, the pressure of the tip may damage the surface, and if the tip is in the vicinity of the surface, the adhesion force from a liquid meniscus layer will disturb the measurement. Therefore, tapping mode is developed to solve this problem.

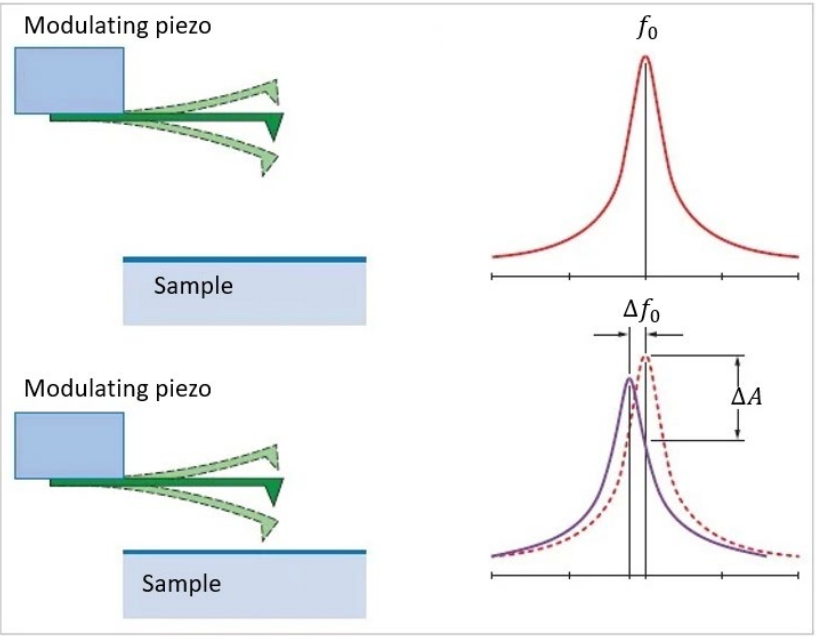

Figure 2.4 Tapping mode AFM. the cantilever is oscillating vertically at high frequency during raster scanning. Interaction of the tip with the sample causes attenuation of the oscillation amplitude, which is used to monitor changes in sample height.

In tapping mode, a piezo stack excites the cantilever substrate vertically, causing the cantilever to vibrate. Usually, the cantilever has to be tuned to work at or close to the resonance frequency. When the tip comes close to the sample, the tip-sample interaction forces, such as Van der Waals forces, electrostatic force, etc. change the amplitude and phase of the cantilever (Figure 2.4). New amplitude enters the feedback loop as input signals, then the system adjusts the scanner height to maintain the amplitude setpoint. In this way, tapping mode can image the topography by sensing the interaction force.[37]

Although the peak force from the resonance of cantilever as the tip “taps” along the surface is larger than in contact mode, tapping mode (dynamic force mode) is less destructive than contact mode because it frees the lateral force. On the other hand, the

phase shift by the interactions provides useful information about the stiffness or the adhesion. Principally, attractive forces lower the frequency and repulsive forces increase it. In the situation where a sample is composed of several components, different components can be easily differentiated by the phase contrast image (Figure 2.5).

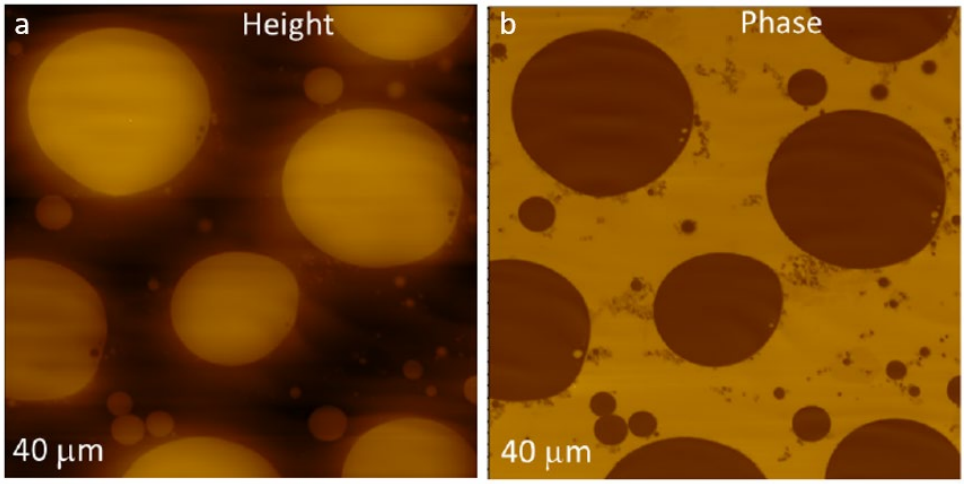

Figure 2.5 AFM height and phase images of a film of polystyrene/ polybutadiene blend.[38]

Peak force tapping mode

In this thesis, AFM images were produced by Dimension Icon Scanning Probe Microscope (SPM) using ScanAsyst mode. It is essentially based on the peak force tapping mode. The system performs a very fast force curve at every pixel in the image and exploits the peak force at every point as the feedback input to maintain a user-defined peak force setpoint. It is easier to extract information as to materials from the force curve than the oscillating waves in typical tapping mode, so intelligent algorithms can adjust automatically scan parameters, such as set point, feedback gains, and scan rate, to optimize the image. It not only lessens the damage of contact mode but simplifies the user's actions.

2.2.2 Polarized Light Microscopy

A polarized light microscope (PLM), i.e., an optical microscope equipped with polarizing filters, is usually used to observe specimens that have strong optical anisotropy, e.g., birefringent crystals. The principles of PLM is shown in Figure 2.6. Unpolarized light pass through the first filter, called polarizer, which selects a polarization among all waves of light. In position 1 in Figure 2.6, in-phase east-west (E-W) plane polarized light enters a uniaxial crystal assuming a positive uniaxial indicatrix and is split into two beams, a fast ordinary ray (lower refractive index) and a slow extraordinary ray (high index), and ψ is the angle between the optical c axis ($\hat{x}$ axis, n_e direction) and the polarizer axis. n_o direction is the $\hat{y}$ axis perpendicular to $\hat{x}$ axis. The biaxial ellipsoid shape of the indicatrix belongs to the tetragonal crystal system (a=b≠c, α=β=γ=90°). The direction of the extraordinary index is known as the major axis, and the other as the minor axis. The intensity of the split rays depends on the angle ψ. Assuming the transmittance along $\hat{x}$ and $\hat{y}$ axis is t_x and t_y, the incident light passing through the polarizer has the polarization as

$$\vec{E} = E(\cos\psi\,\hat{x} + \sin\psi\,\hat{y})$$

After passing through the crystal, the polarization becomes

$$\vec{E}_1 = E(t_x\cos\psi\,\hat{x} + t_y\sin\psi\,\hat{y})$$

The analyzer axis, which is perpendicular to the polarizer axis, is

$$\hat{A} = (\sin\psi\,\hat{x} - \cos\psi\,\hat{y}).$$

After the analyzer the light amplitude becomes:

$$\vec{E}_1 \cdot \hat{A} = \frac{1}{2}E\left(t_x - t_y\right)\sin(2\psi)\,. \tag{2.2}$$

When $\psi = n\left(\frac{\pi}{2}\right)$, n is an integer, there is no transmitted light.

The maximum light is expected when $2\psi = \frac{\pi}{2} + n\pi$ or $\psi = \frac{\pi}{4} + \frac{n\pi}{2}$.

On the other hand, there will be a phase shift between the ordinary ray and the extraordinary ray following the crystal refraction. At the position 2 in Figure 2.6, the fast ray is one wavelength ahead of the slow ray, and the analyzer only allows the N-S vibration components to transmit. If the crystal is positioned with the optic axis parallel or perpendicular with the polarizer, it will appear black in cross polarized light as $\psi = n\left(\frac{\pi}{2}\right)$.

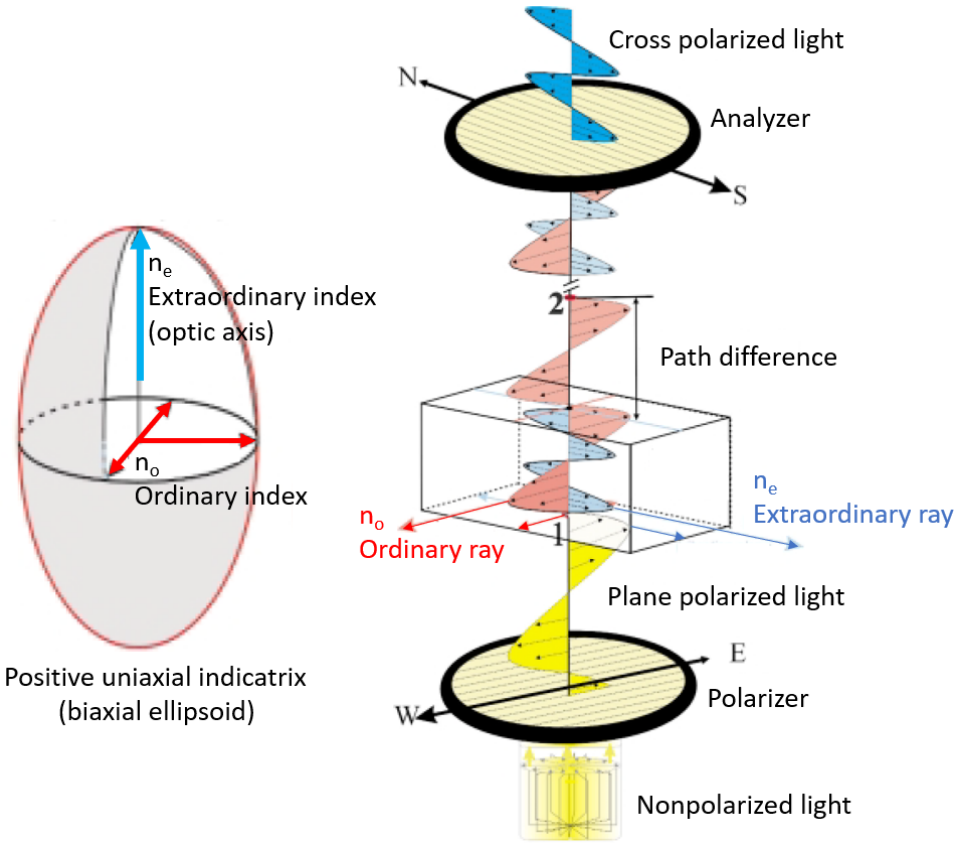

Figure 2.6 Schematic of a polarized light microscope.

2.2.3 Laser Scanning Confocal Microscopy (LSCM)

Different from the conventional wide-field optical microscope where the entire sample is shone in light, a confocal microscope only focuses on one depth level at a time. As shown in Figure 2.7, two pinhole apertures are positioned at confocal positions. A laser beam passes through the pinhole, then is focused by the objective lens into a small part of the sample. The scanning unit can move the laser light precisely and quickly. The emitted light from the sample then travels back through the dichroic mirror. The second pinhole positioned in the focal plane chooses only the light from the targeted point of the sample. Because the light may have a very low intensity, the photomultiplier (PMT) is exploited

amplify the photon signal. The output signals from the PMT are then converted into an image shown in the computer. The surface of the sample at a specific height is scanned continuously by moving the sample or the light. Finally, all pixels are combined to produce a 2D image. The focal plane can also move vertically to do optical section. In this case, laser is used to scan the sample at different heights, then reconstruct a three-dimensional image using proper software. Confocal microscope has a better spatial resolution than the conventional optical microscope.

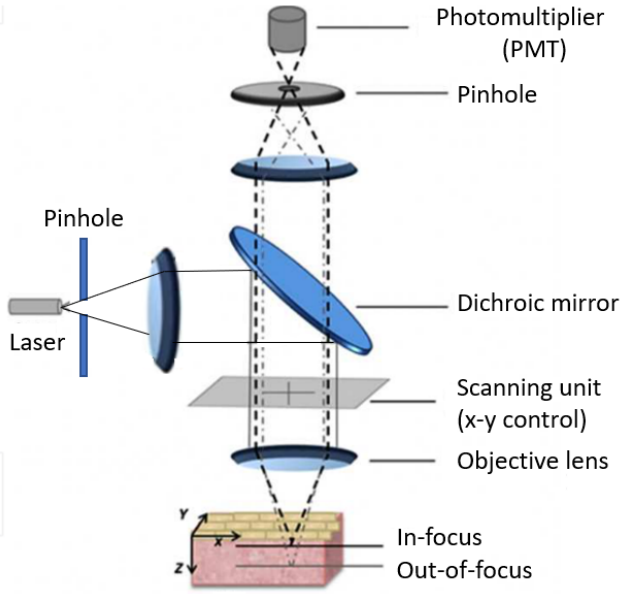

Figure 2.7 Schematic of a confocal microscope.

2.3 In situ electrical measurement

Most electrical transport measurements are performed *ex situ*, i.e., the samples have to be taken out of the growth chamber after deposition, and transfers to other instruments such as, Cryostat, physical property measurement system (PPMS). This process inevitably exposes samples in air and may change the structure and properties of the materials,

especially for some low-dimensional materials, organics which are highly sensitive to air. To overcome this problem, a system for *in situ* electrical measurement during or immediately after the sample growth in ultra-high vacuum (UHV) is highly desirable.

One common technique is to use the micro-four-point probe (M4PP) to perform the four-point measurement.[39] One M4PP consists of a probe chip with four isolated cantilever covered with a conductive layer as a metal electrode (Figure 2.8). The electrode spacing ranges from 5 to 30 μm. Four electrodes can be arranged linearly or in square shape depending on whether the anisotropic measurement is required.[40] By connecting an independent transport measurement chamber (TC) equipped with the M4PP to a deposition chamber (e.g., molecular beam epitaxy (MBE) chamber in Figure 2.8b), electrical transport measurement can be performed *in situ* under the same UHV environment.[41] One drawback using M4PP is that the tip may damage the sample surface by exerting too large pressure. When the temperature changes, the tip has to be withdrawn in advance so as not to scratch the surface due to distinct temperature-induced strain, and it makes the electrical measurement under varying temperatures troublesome.[41]

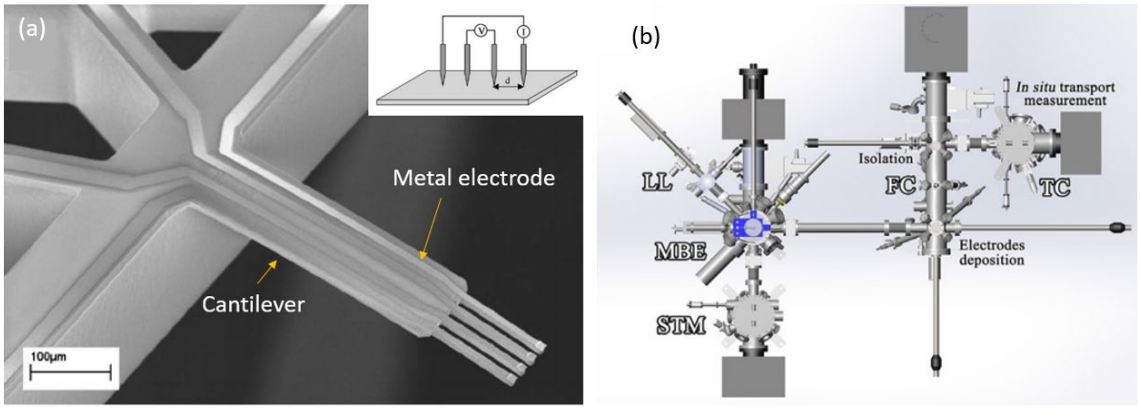

Figure 2.8 (a) SEM image of an microscopic four-point probe.[39] (b) An *in situ*

measurement system. LL: Load Lock; STM: Scanning tunneling microscope; FC: Function chamber.[41]

2.3.1 In situ measurement with in-plane electrodes

In this thesis, the *in situ* electrical transport measurement is implemented by exploiting substrates with interdigitated electrodes which are prepared before placing them in the deposition chamber. A typical substrate with interdigitated electrodes (IDE) which can be purchased from Metrohm DropSens Inc., is indicated in Figure 2.9. IDEs are composed of two gold electrodes with two connection tracks on glass substrates. The thickness of gold is approximately 150~200 nm, underneath which there is an adhesion layer of Ti of several nanometers. The spacing between two digits is ~4 μm. Figure 2.9 shows an optical image of the Pt electrodes on the glass.

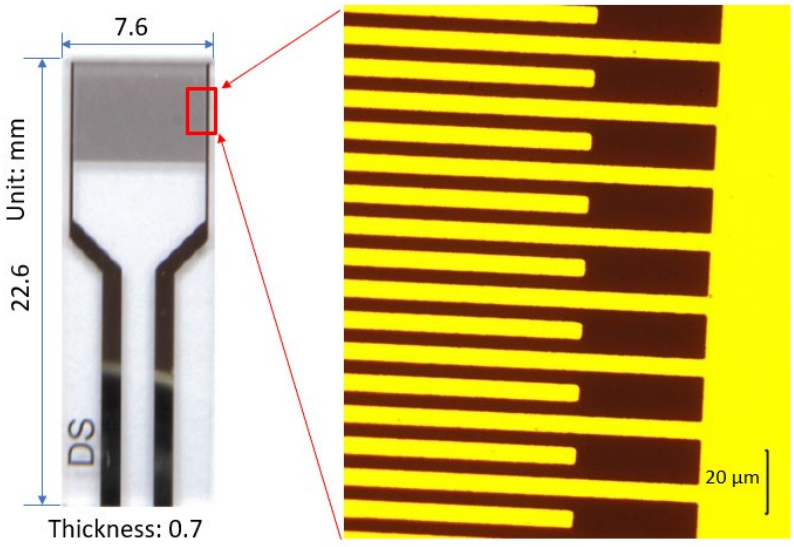

Figure 2.9 The macroscopic and microscopic view of an IDE substrate

IDE substrates are typically adhered to a copper holder (Figure 2.10) by a thin layer of varnish, then the holder can be mounted either at close or far substrate position in the

deposition chamber (Figure 2.1). Al/Si wires of diameter 25 μm are used to electrically connect the IDE bands to the printed circuit board (PCB) with the help of conductive silver paint. Then Kapton UHV shielded cable which can reduce the noise signals is connected through an electrical feedthrough to other instruments, such as a ferroelectric tester, an impedance analyzer, etc., outside the chamber for transport measurement. Since the electrical transport measurements can be carried out during the deposition, it can be used to monitor the growth process. The LN2 cooling system allows to decrease the temperature down to 100 K.

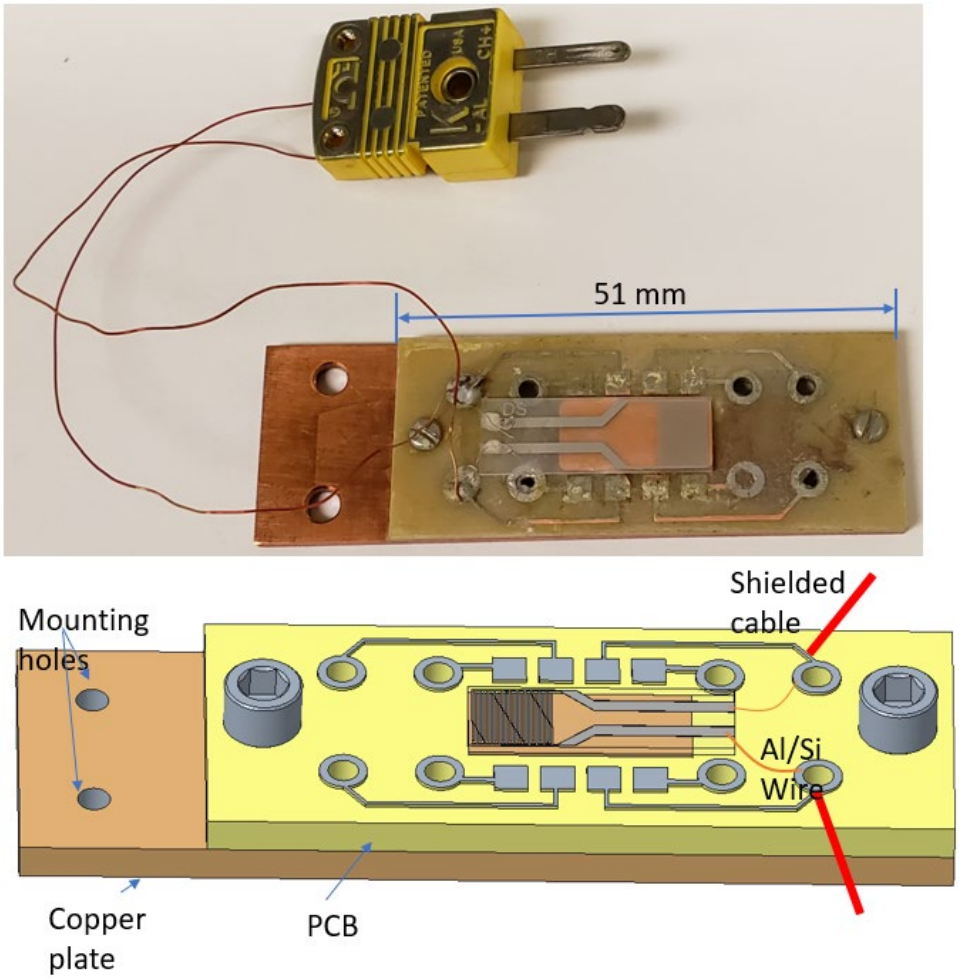

Figure 2.10 the macroscopic image and 3D model of the substrate holder

Although the prepared IDE substrate frees the experiment from the deposition of electrodes in the chamber, some tiny dusts sticking to the electrodes have large effect on the electrical measurement. Even one dust adhered to the 7×4.8 mm^2 area of electrode arrays with 4 μm spacing will generate the leakage currents. Hence, in the cleanroom, the substrate is firstly cleaned ultrasonically in 1 mol/L $FeCl_3$ solution for 15 minutes and in isopropanol for another 15 minutes, then assembled onto the holder. After mounting the holder with the substrate onto the deposition position in the Evovac chamber, the status of the substrate is examined by the D-V_{app} loop (electric displacement - applied voltage loop) in vacuum. A good IDE substrate free of dusts demonstrates a hysteresis loop (Figure 2.11) for a linear capacitor with a small leakage current. Irregular hysteresis loops indicate dust particles on the substrate, which can be resolved by repeating above steps.

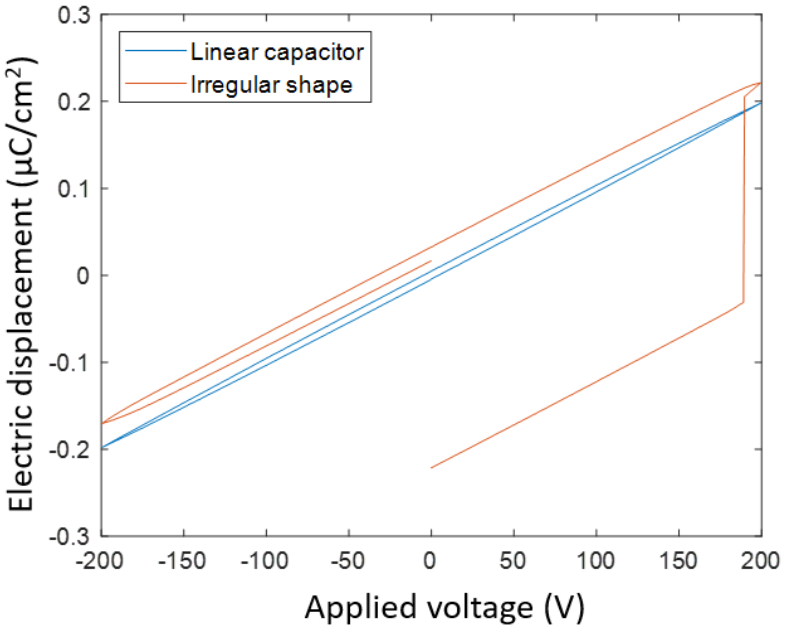

Figure 2.11 Hysteresis loops of perfect IDE substrate free of dust and the one with some dust particles.

2.3.2 Electric displacement field-electric field (*D*-E_{app}) loop measurement

In early days, most hysteresis loop measurements are based on traditional Sawyer-Tower circuit[42] shown in Figure 2.12a which is useful to characterize ferroelectrics. The sample capacitor (C_{ferro}) is in series with a reference capacitor (C_0) of a much larger capacitance. Since the accumulated charge across the sample and the reference capacitor are equal, $Q = C_{\text{ferro}}(V_i - V_0) = C_0 V_0$, if C_0 is much larger than C_{ferro}, the voltage drop across the reference capacitor (V_0) can be neglected. The input voltage (V_i), sample thickness (z), sample area (A), and C_0 are known parameters, so the applied electric field is

$$E_{app} = \frac{V_i}{z} \tag{2.3}$$

And the electric displacement is calculated as

$$D = \frac{Q}{A} = \frac{C_0 V_0}{A} \tag{2.4}$$

By measuring the voltage across the reference capacitor (V_0), the *D*-E_{app} loop can be acquired. In most studies, the intrinsic polarization of one material is more desired, and the polarization (P) is calculated with the equation

$$P = D - \varepsilon_0 E_{\text{app}} \tag{2.5}$$

The term $\varepsilon_0 E_{\text{app}}$ is much smaller than P, so *D*-E_{app} loops have similar shape with *P*-E_{app} loops. When one period of triangular wave is applied to a ferroelectric capacitor, a typical ferroelectric *P*-E_{app} hysteresis loop is indicated in Figure 2.12b. The first preset loop is used to initialize the capacitor. When E_{app} is equal to zero, the polarization is the remanent polarization P_{r}.

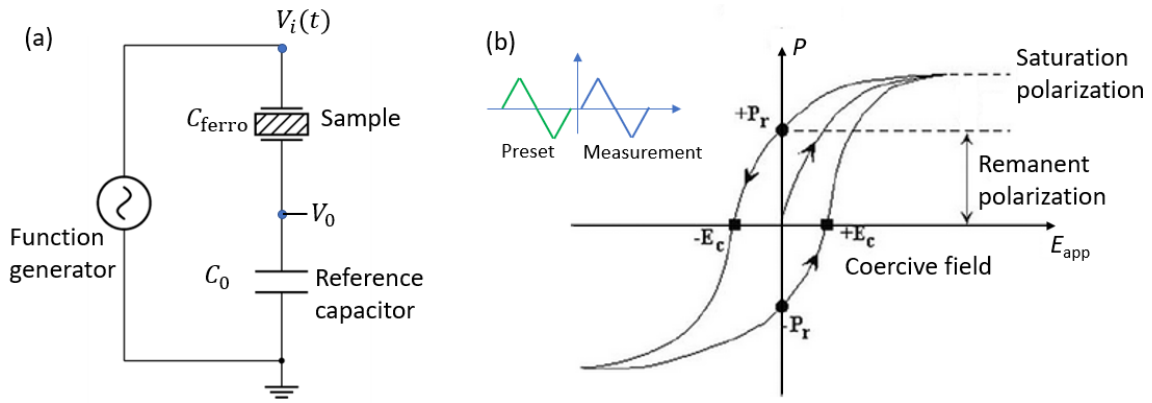

Figure 2.12 (a) Schematic of the Sawyer-Tower circuit. (b) A typical ferroelectric hysteresis loop.

With the development of the modern microelectronics, the accumulated charge can be measured accurately using virtual ground operational amplifier, e.g., in Radiant RT66C Ferroelectric Tester, instead of the reference capacitor.[43]

Another common waveform to measure polarization is the double-wave method (DWM), shown in Figure 2.13a. Most ferroelectric D-E_{app} loops by the waveform in Figure 2.12b include three parallel components: ferroelectric, dielectric, and conductive components.[44] The dielectric component will increase D linearly with E_{app}, slanting the hysteresis loops. The DWM can distinguish non-hysteresis components from intrinsic ferroelectric hysteresis loops by applying identical unipolar waves twice. As shown in Figure 2.13, after the initialization of preset half-wave, the dipole moments in ferroelectrics are along "down" direction. The first positive half-wave bias switches dipoles from "down" to completely "up" if the magnitude of the positive bias is large enough, and this produces hysteresis in Figure 2.13b. Ideally the second positive half wave bias only causes the displacement of the dielectric and conductive components as the ferroelectric polarization has been saturated by the first half wave. The intrinsic

ferroelectric displacement (remanence in Figure 2.13b) can be obtained by subtracting non-switching displacement from the switching displacement.

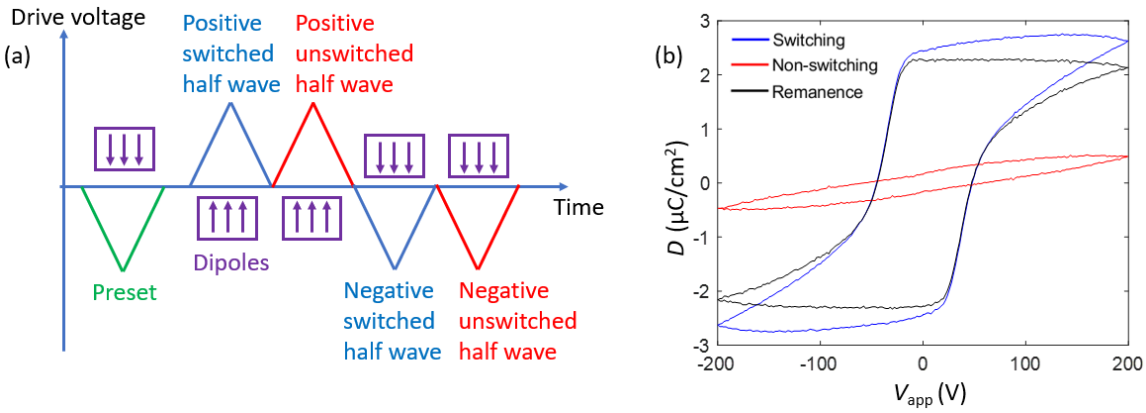

Figure 2.13 (a) The displacement measurement waveform for the double-wave method. (b) Three loops obtained from one cycle of the DWM: switching, non-switching and remanent loops.

The DWM demonstrates the advantages that it can measure non-hysteresis components, and extract hysteresis components, e.g., ferroelectric loops and antiferroelectric loops, without manual compensation.[45]

CHAPTER 3 ELECTRIC-FIELD ASSISTED NUCLEATION PROCESSES AND ELECTRICAL MEASUREMENT OF CROCONIC ACID FILMS

This chapter is reproduced from [CrystEngComm 21 (48), 7460-7467; DOI: 10.1039/C9CE01493D], with the permission of RSC Publishing.

3.1 Introduction

Croconic acid ($C_5H_2O_5$ or CA) as a single-component organic ferroelectric compound that exhibits a large spontaneous ferroelectric polarization[5], is a promising candidate to substitute or supplement inorganic ferroelectrics for future electronic and optoelectronic devices, with advantages of light weight, flexibility, and environment-friendly characteristics. The application potential of ferroelectric CA depends on the possibility of fabricating films of well-defined morphology and electric polarization. Various material-processing techniques, such as spin coating[46], matrix-assisted pulsed laser evaporation[47], inkjet printing[48], and physical vapor deposition (PVD), have been employed to prepare CA films. Thermal evaporation as one type of PVD has the advantages of precise thickness control, possibility for ultrathin organic film, and free from contamination. However, two fundamental issues still need to be addressed. First, due to the weak interaction at the organic/inorganic interface, the growth of organic films on inorganic substrates tend to adopt an island-formation mode[49], resulting in a rough surface[50,51], which affect the device performance.[52] For instance, the carrier mobility and On/Off ratio were significantly reduced with the film roughness in organic thin film transistor.[53]

Second, non-epitaxial growth typically leads to polycrystalline films, which undermines the net electric polarization.

Here we attack the problem using physical vapor deposition assisted by an electric field. The dipole moment carried by the CA molecules and the spontaneous polarization of the CA crystals offer an additional knob in controlling the film growth and aligning the molecular dipoles by varying the energetics of the growth. An electric field E may contribute to the electrostatic energy of a dipole D_m by ED_m. For CA (D_m=2.5018×10^{-29} C·m)[5] in an electric filed 2 MV/m, which is lab-achievable, the electrostatic energy is equivalent to the thermal energy at temperature about 4 K. On the first look, this energy is not expected to generate a large impact on film growth unless at very low temperature. However, this estimation is based on fully equilibrium state of the film/substrate. In fact, the film growth on a substrate involves a sequence of inequilibrium processes, such as deposition, surface diffusion, and desorption, followed by nucleation and post-nucleation growth[24,54], as illustrated in Figure 3.1.[55] In particular, from the classical nucleation theories (CNT), the dynamic nucleation process is governed by competition between the volume enthalpy change, surface, and interfacial energies[56], which leads to its strong temperature dependence. It is possible that an electric field may impact this dynamic process, especially when the electrostatic energy of the dipoles can tip the balance in a close energy competition. Indeed, previous experiments validated that the external electric field promoted nucleation in different systems.[57] For instance, the electric field produced nucleation of bubbles at lower superheat ΔT (temperature of the liquid minus the boiling point) of organic liquids.[58] He et al.'s experimental research indicated that the external electric field largely increased the ion-induced nucleation rate.[59] In terms of

nucleation in aqueous medium[60], it is shown that the nucleation rate of NaCl crystal is increased by 233% by an electric field strength of 0.1 MV/m.

In this work, we studied temperature-dependent CA film growth in a 2.1 MV/m out-of-plane electric field, focusing on the nucleation process using a 5 nm nominal thickness to avoid grain coalition. The results confirm the non-monotonic temperature dependence predicted by CNT, where a maximum nucleation rate occurs in the intermediate temperature. The electric field clearly shifts the temperature dependence of the nucleation rate. An analysis in terms of CNT reveals the substantial effects of electric field on the critical gas-solid transition temperature, film/substrate interfacial energy, and surface diffusion energy.

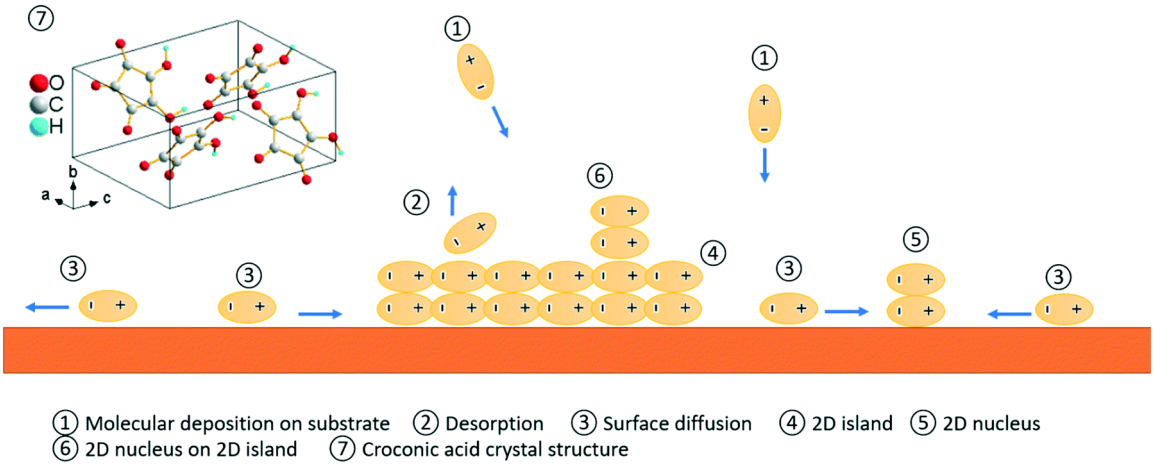

Figure 3.1 Atomic model of CA molecular crystal and the film growth processes on a substrate where the CA molecules are represented by dipoles. The plus and minus signs represent the positive and negative poles of polar molecules respectively.

3.2 Experimental

Preparation of CA films with and without the electric field

Croconic acid powders from Alfa Aesar, with purity of >98%, were used as the source material. The melting point is larger than 300 °C and its crystal starts to decompose at ~177 °C.[5] The substrates are 100 nm Au(111)/10 nm Ti(111)/Si(100). Films were deposited in pairs simultaneously, one with and one without electric field, at various temperatures. Their deposition time (42 min) and distance (~50 cm) between the source and the substrate were the same. The configuration for each film is shown in Figure 3.2a, where the conductive meshes (46 μm hole) is separated from the substrate by 100 μm. A voltage bias of 210 V was applied to the mesh of one of the films, corresponding to an electric field 2.1 MV/m. All films were deposited at far position (Figure 2.1) by thermal evaporation using an EvoVac deposition system from Angstrom Engineering with a rate of 0.02 Å/s, an initial pressure 1.3×10^{-4} Pa, and a nominal thickness of 5 nm. The source-substrate distance was 50 cm. The substrate temperature was controlled using a liquid-nitrogen flow cryostat. Before deposition, the substrates were rinsed with isopropanol and deionized water three times. After the deposition, the substrate temperature was warmed up slowly to room temperature before the films were taken out of the growth chamber.

Morphology and structural characterizations

Atomic force microscopy images with a resolution of 512×512 pixels and an area of 1 μm^2 were collected by the Bruker Dimension Icon system in a ScanAsyst automatic image optimization mode and analyzed using Gwyddian software. X-ray diffraction (XRD) was carried out using a Bruker D8 Discover diffractometer with the fixed incident angle ω=10° to verify the crystal structure of grown films using a thick (950 nm) film due to the small structural factor of the light elements in croconic acid, as shown in Figure 3.2b. The diffraction peaks of the film, which were normalized to the intensity of (210)

plane, matched well with the standard pattern of croconic acid from CCDC no. 147324[61]. All the measurements were performed at room temperature and ~60% RH within one day after the films were deposited.

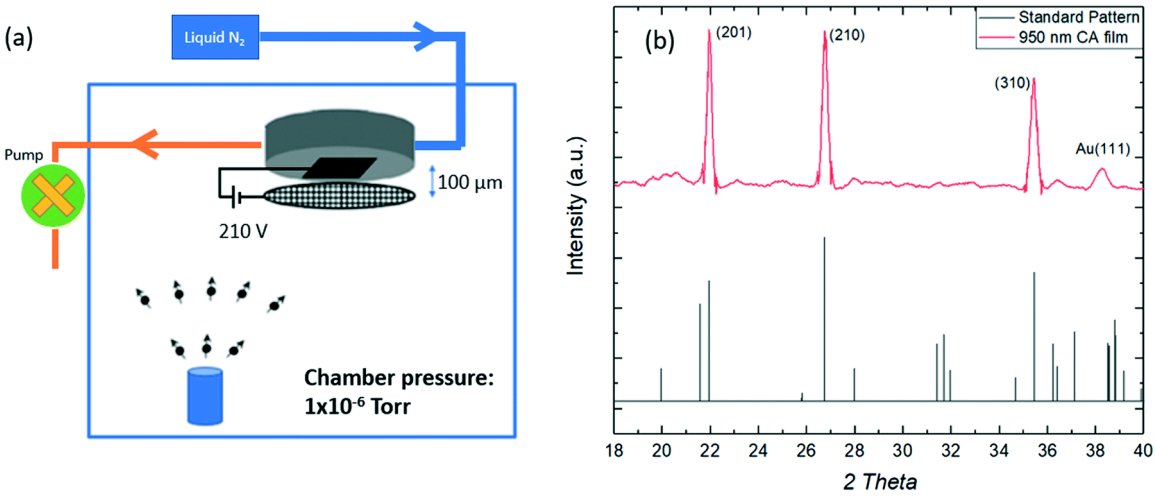

Figure 3.2 (a) Experimental setup of the film growth under the electric field. (b) XRD patterns of the croconic acid films with a thickness of 950 nm, compared with the calculated patterns (see text).

3.3 Results and Discussion

Morphology of CA films

Figure 3.3 shows the AFM images of films grown with and without the electric field at three different temperatures, and the corresponding height histograms $P^h(z)$ as the insets, where P^h is probability and z the height. All images have the same color and length scale. The height histogram of each film can be decomposed into the substrate and film peaks at smaller and larger height respectively. The position of the substrate peak is set to zero as the reference.

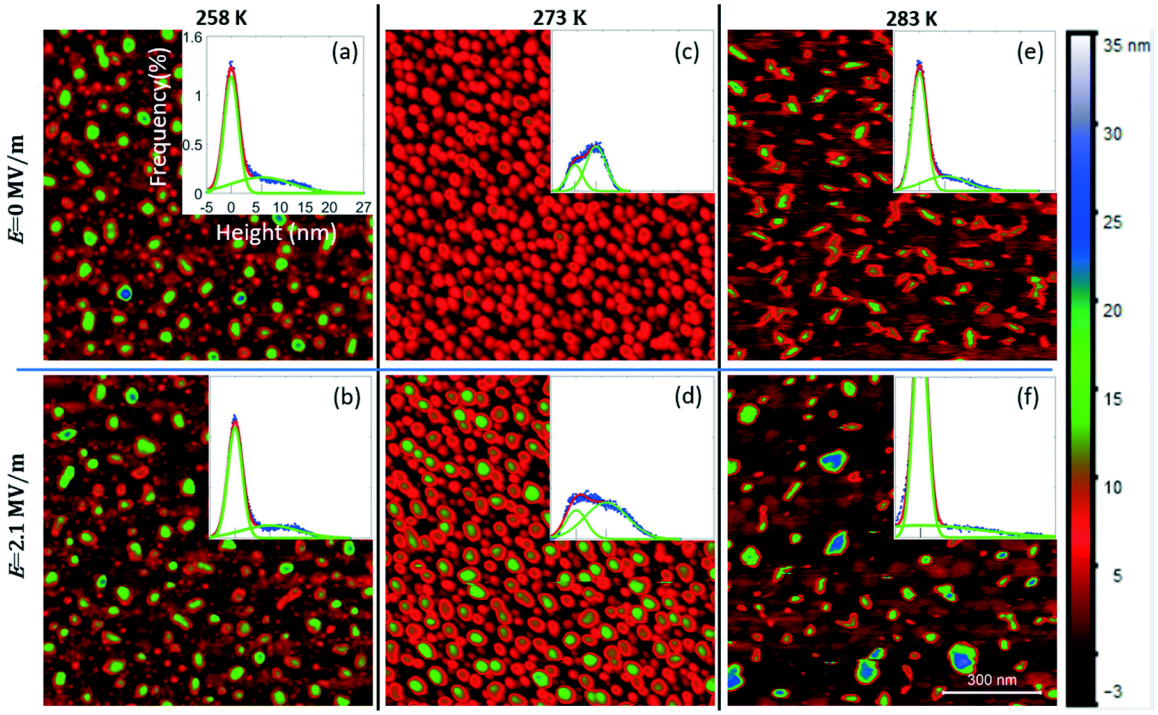

Figure 3.3 AFM images of CA films grown with different substrate temperatures with and without the electric field under the same deposition time and distance. (a) and (b) 258 K; (c) and (d) 273 K; (e) and (f) 283 K and different electric field strengths. The insets are the corresponding height histograms whose horizontal and vertical axes are the height and frequency, respectively. Green lines are deconvoluted Gaussian peaks whose peak positions are marked with short vertical lines on the x-axes. All the images have the same scale bar as in (f).

Overall, the film consists of well-separated CA grains due to the small nominal thickness. The film morphology changes dramatically with temperature, at both low (258 K) and high (283 K) temperature, the coverage of the substrate surface is low, as seen from the intense substrate peak, although at high temperature the CA grains tend to have more facets. In contrast, at intermediate temperature, such as 273 K, a large number of

CA grains were found on the substrates, leading to a larger coverage, as seen from the weak substrate peak. When the substrate temperature is increased to 293 K, the number of grains is too small to distinguish CA film from the substrate using an optical microscope. For higher temperatures, no CA grains could be found.

The effect of electric field is also visible from Figure 3.3. In particular, at 273 K, the CA grains grown within the electric field has a larger dispersion of height, as indicated by the wider film peak in Figure 3.3d compared with that in Figure 3.3c. This larger dispersion of height remains at 283 K when the growth is under the electric field, as indicated by the longer tail of the histogram and apparently larger grain size in Figure 3.3f compared with that in Figure 3.3e. At 283 K, the impact of electric field on the shape of the grains is also discernable: without electric field, the grains are more elongated than those grown with the electric field.

Nucleation process

In the case of low coverage and not so high temperature, the nucleation rate is proportional to the grain density, assuming no coalition of nuclei. It is observed that at 293 K, large grains are surrounded by small clusters by Ostwald ripening,[62] as shown in Figure 3.4. It only appeared at very high temperature due to the sufficiently large diffusion length of molecules. Therefore, to quantify the effect of temperature and electric field on the nucleation process of CA films, we analyzed the grain density of the films using the height histogram $P^h(z)$. The grains were identified above a threshold height z_0 which was determined as the intersection point of the substrate peak and the film peak and above which grains were clearly differentiated from the background. Each data point is the average of three AFM measurements on different areas of the same film.

Error bars show the standard deviation from the mean.

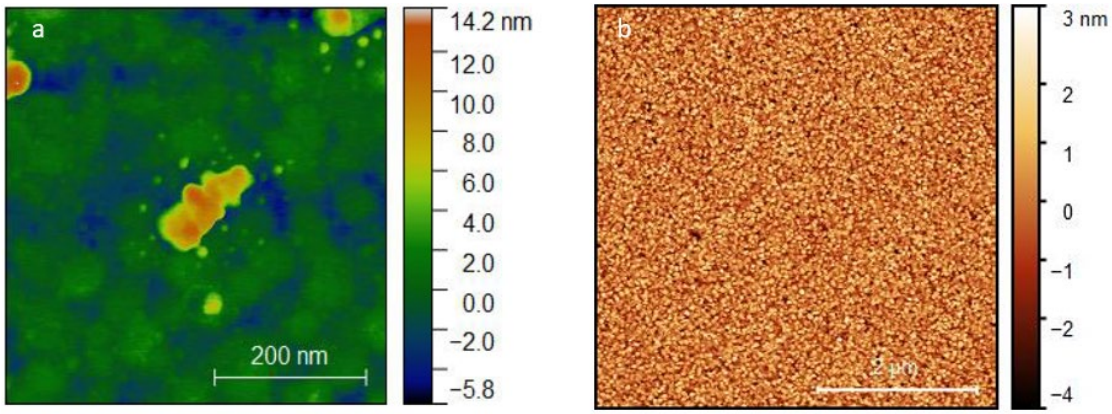

Figure 3.4 (a) AFM image of CA film at 293 K without electric field. The lateral dimension of image is 500 nm. (b) AFM image of the Au/Si substrate before deposition.

The grain densities are plotted against temperature with and without electric field in Figure 3.5a respectively. Regardless of the presence of an electric field, the grain density as a function of temperature shows a maximum. The electric field has a clear effect that shifts the maximum grain density from about 273 K to about 258 K. The largest impact of the electric field occurs at 243 K, where the average grain density changes from 234 to 452 μm^{-2}, corresponding to 93% increase, whereas it decreases from 59.6 to 0 μm^{-2} at 293 K.

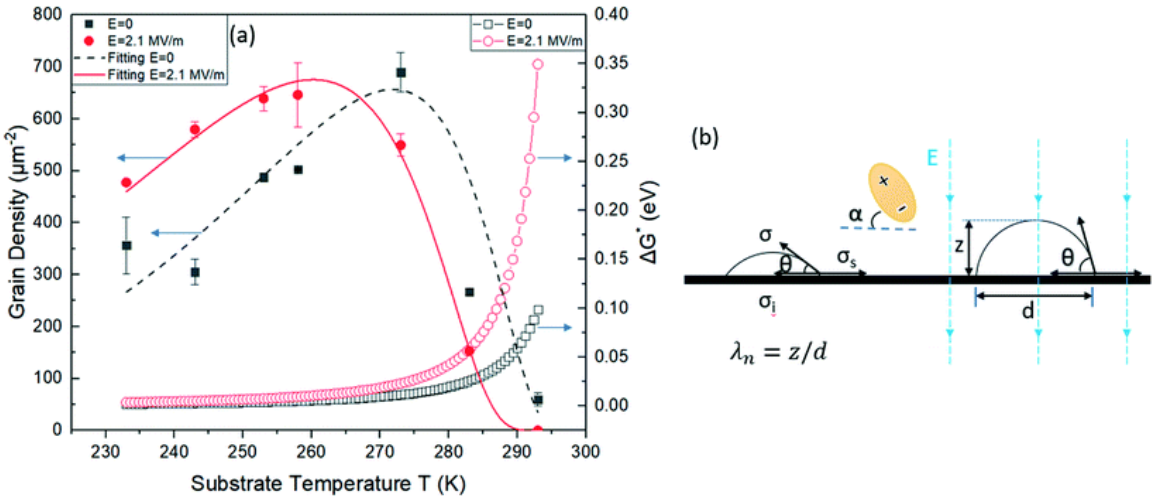

Figure 3.5 (a) Grain density and nucleation barrier as a function of the substrate temperature with and without the electric field. (b) The diagram of the heterogeneous nucleation process with and without the electric field.

The temperature dependence of the nucleation rate has been studied previously[63–65], especially on the steady-state nucleation rate *I*. In case of the heterogeneous nucleation from vapor with a constant impinging rate[66], the nucleation rate is related to the transport barrier ΔG_m and nucleation barrier ΔG^*:

$$I(T) = \frac{1}{(k_B T)^{\frac{1}{2}}} \Gamma \exp\left(-\frac{\Delta G_m}{k_B T}\right) \exp\left(-\frac{\Delta G^*}{k_B T}\right) \tag{3.1}$$

$$\Gamma = 2\sigma^{\frac{1}{2}} v_c \frac{\lambda_f l}{v_g^2} (1 - \cos\theta) \tag{3.2}$$

$$\Delta G^* = \Lambda \frac{T_m^2}{(\Delta T)^2} \tag{3.3}$$

$$\Lambda = \frac{16\pi\sigma^3 v_c^2 \phi(\theta)}{3L_V{}^2} \tag{3.4}$$

where θ is the wetting angle (Figure 3.5b), λ_f is a frequency factor, l is the mean free

path of molecules in the gas, $1/v_g$ is the number of gaseous molecules in unit volume, Δh_m is the enthalpy change of sublimation (latent heat), T is the temperature, T_m is the equilibrium gas-solid transition temperature, $\Delta T=T_m-T$, v_c is the molar volume of the crystal phase, σ is the surface energy, $\Delta G_m= E_{sd} - E_{des}$, E_{des} is the activation energy for desorption, E_{sd} is the activation energy for surface diffusion, k_B is Boltzmann constant, and the wetting function is

$$\phi(\theta) = \frac{1}{4}(1-\cos\theta)^2(2+\cos\theta) \tag{3.5}$$

One can understand the temperature dependence of the nucleation rate $I(T)$ from Eq. (3.1). Since the nucleation barrier $\Delta G^* \propto 1/(\Delta T)^2$, when $T \rightarrow T_m$ ($\Delta T \rightarrow 0$), ΔG^* approaches infinity, corresponding to the diverging barrier around the gas-solid phase transition temperature. Therefore, at high temperatures, increasing temperature decreases nucleation rate; this is the nucleation-barrier-limited region. At low temperatures, the nucleation barrier ΔG^* approaches a constant. The factor $\exp(-\Delta G^*/kT)\exp(-\Delta G_m/kT)$ then determines the temperature dependence of the nucleation rate. In other words, at low temperature, the reduced thermal energy reduces the chance of molecules overcoming the diffusion and nucleation barrier, which leads to the diminishing nucleation rate; this is the diffusion-limited region. The different temperature dependences at low and high temperature ranges then result in a maximum nucleation rate at the intermediate temperature, as observed in Figure 3.5a.

To gain quantitative understanding of the nucleation process, i.e., the critical parameters that govern the nucleation rate $I(T)$, one may fit the experimental observation in Figure 3.5a with the classical nucleation theories. The fitting is carried out using Eq.

(3.1) with four fitting parameters Γ, ΔG_{m}, T_{m}, and Λ. The fitted curves are plotted in Figure 3.5a and the fitting parameters are shown in Table 3.1. To the best of our knowledge, these parameters for CA grown on Au (111) haven't been reported before.

Table 3.1 Fitted parameters for the model function with and without the electric field.

E (MV/m)	Γ ($\times 10^5$)	ΔG_{m} (eV)	Λ (10^{-4} eV)	T_{m} (K)
0	4.7 ± 0.6	0.19 ± 0.01	1.2 ± 0.1	303.4 ± 0.2
2.1	0.8 ± 0.1	0.139 ± 0.003	1.9 ± 0.2	299.9 ± 0.9

For the barrier coefficient Λ, the fitted value with electric field is larger than that without electric field, as seen in Table 3.1, implying the increased nucleation barrier by the electric field. At high temperature or nucleation-barrier-limited region, the diffusivity of molecules is large enough. The direct consequence of the increased nucleation barrier by the electric field is the reduced nucleation density at the higher temperature as shown in Figure 3.5a. At 273 K, the electric field increases the nucleation barrier ΔG^* from 0.012 eV to 0.023 eV. To further analyze the reasons for the increased Λ, we examine the relation between the surface energy and the sublimation energy[67],

$$\sigma = k_{\mathrm{c}} \left(\frac{L_{\mathrm{v}}}{N_{\mathrm{A}}^{1/3}} \frac{1}{v_c} \right)^{2/3} \tag{3.6}$$

where N_{A} is Avogadro's number, k_{c} is a constant. Substituting Eq. (3.6) into Eq. (3.4), one has $\Lambda = \frac{16\pi {k_{\mathrm{c}}}^3}{3{N_{\mathrm{A}}}^{2/3}} \phi(\theta)$. In other words, the increase of Λ is directly caused by the increase of $\phi(\theta)$, corresponding to the increase of wetting angle θ. If we assume that the nucleus has the shape of a spherical cap, the wetting angle θ is related to the aspect ratio λ_{n} of the nucleus, whose definition is seen in Figure 3.5b,

$$\cos\theta = (1 - 4\lambda_n^2)/(1 + 4\lambda_n^2) \quad (3.7)$$

The fact that θ increases in the electric field implies that λ_n also increases.

According to the well-known relation of Young[66], $\cos\theta = (\sigma_s - \sigma_i)/\sigma$, the wetting angle θ is the balanced result of free surface energy of nucleus σ and the substrate σ_s, and of the substrate-nucleus interface σ_i (Figure 3.5b). It is unlikely that a change in σ_s is the underlying factor for the shift in the wetting angles. Therefore, the large increase of θ could be attributed to the increase of σ_i and σ in the electric field. It was found[50] that the planar CA molecules tend to lie down on the Au substrate with their polar axes in the film plane.[68] As shown in Figure 3.5b, if α is the angle between molecules and the surface, the fact that molecules tend to lie down on the surface implies that σ_i is minimal when α is zero. When there is an out-of-plane electric field, the molecules tend to align their polar axis along the field direction, which means increasing α and σ_i. Therefore, wetting angle θ tends to increase with the out-of-plane electric field according to the relation of Young.[66] Similarly, the wetting angles of some polar droplets, such as alcohols, alkanes, and octanol, increase in the out-of-plane electric field as well which is also attributed to the increase of interface energy σ_i.[69]

For the diffusion barrier ΔG_m, 0.19 eV and 0.14 eV were found from the fit for E=0 and E=2.1 MV/m respectively. These values are comparable with that of H atomic diffusion on the Cu (001) surface (0.197 eV)[70], and water monomer on Pd(111) (0.13 eV)[71], in agreement with the analysis reported by Hooper et al. [68] concerning the diffusion of CA molecules on Au (11) and Ag (111). The reason that the electric field reduces the transport barrier of nucleation may be related to the increase of the interfacial energy σ_i by the electric field. As discussed above, the out-of-plane electric field tends to

pull the molecular polar axis away from the substrate surface and increase σ_i; this leads to a weaker binding between the molecules and the substrate surface and lower diffusion barriers.

For the solid-gas transition temperature T_m, the fit suggests that the value reduces from 303 K to 300 K in the E=2.1 MV/m out-of-plane field. In particular, at 293 K, no CA grains formed on the substrate with the electric field compared with a few grains on films grown without the electric field. Similar results were found earlier regarding the decreased melting temperature of gold in strong electric field.[72] From classical thermodynamics, the change of Gibbs free energy in the phase transformation is $\Delta g = \Delta h - T\Delta s$. At equilibrium transition temperature T_m the free energies of gas and solid are equal, i.e. $\Delta g = 0$. Consequently

$$T_m = \Delta h/\Delta s \tag{3.8}$$

where $\Delta h = h_{gas} - h_{solid}$, h_{gas} and h_{solid} are the enthalpy of the gas and solid phases respectively. Naturally, one may expect that the electric field would lower h_{solid} since the solid CA consists of aligned electric dipoles which may reduce the energy. However, since the in-plane dipole moments of the CA molecules are mostly perpendicular to the out-of-plane electric field, the contribution of electrostatic energy to the enthalpy in the solid CA is minimized. In contrast, in the gas phase, molecules can be aligned by the electric field and reduce h_{gas}. The reduced h_{gas} leads to decreased T_m.

Thus, the out-of-plane electric field decreases the surface diffusion barrier (ΔG_m) of CA on Au (111), increases the interface energy (σ_i), and increases T_m. These factors cause the shift of temperature profile of the nucleation rate. It is expected that when the system size increases, e.g., when the films are thick enough to cover the whole substrate,

the nucleation rate will increase because the underlying CA film instead of Au becomes the effective substrate. Unfortunately, we could not predict the scaling of the electric field's effect with thickness under current model. Generally, the effect of electric field in the phase transformation depends on the nature of the transitions. Radacsi's review[73] demonstrated the positive effect of DC/AC electric field toward crystallization from solution including reducing nucleation time, and orienting crystallites. In terms of nucleation from vapor phase, Ghosh[74] demonstrated the increase of transient nucleation rate of charged droplets in the water vapor. The electric field can also align molecules in the deposition from vapor.[75]

The above analysis uses the intersection point of the substrate peak and the film peak (Figure 3.3) to define grains. However, very small particles, e.g., with ~10 nm diameter and ~ 1 nm height in Figure 3.3a, exist as well; they are included in the substrate peak. Their nucleation mechanism is different from the above-discussed process that requires diffusion. Instead, those particles nucleate on the substrate defects, such as step edges, corresponding to much lower nucleation barriers; desorption factor then plays a major role in the process. The diagram for this process is illustrated in Figure 3.6c. The desorption process limits the growth rate according to the factor $\exp(E_{\mathrm{des}}/\mathrm{k}T)$, which predicts monotonic increase of film thickness or coverage with temperature. This can be seen in Figure 3.6a, where excluding the peaks, the mean thickness increases as temperature decreases.

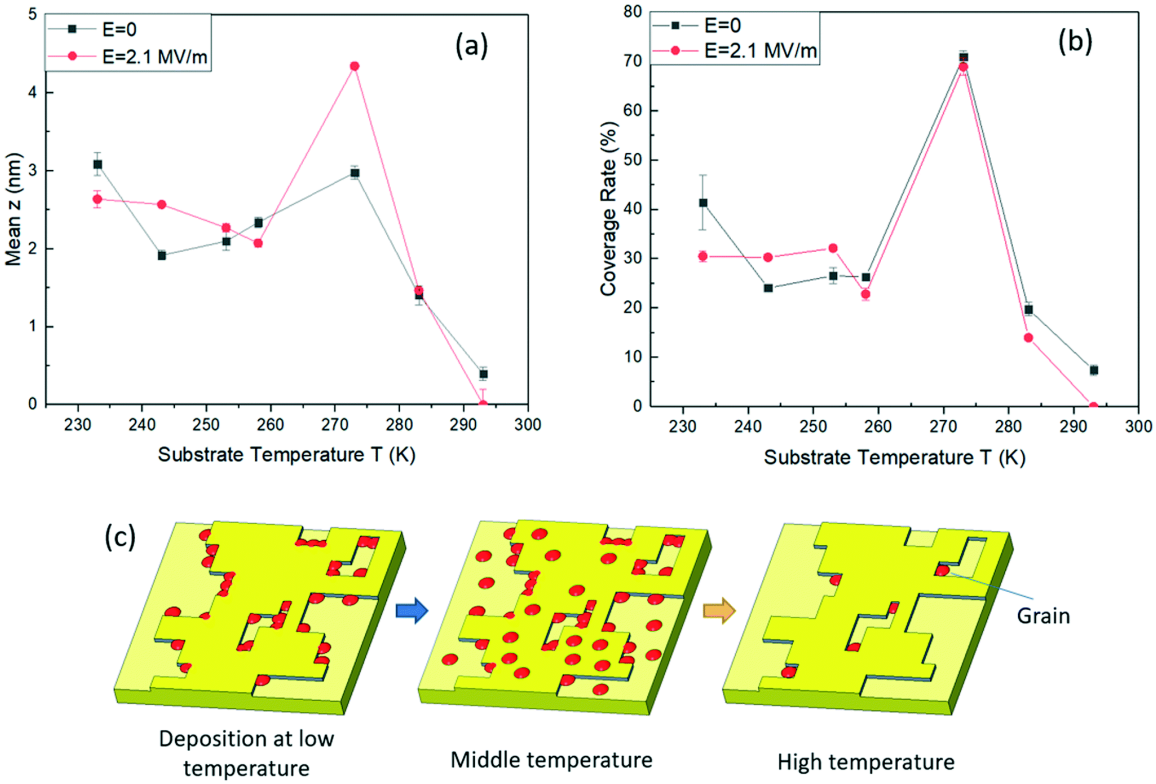

Figure 3.6 (a) The average thickness and (b) the coverage rate of CA films versus substrate temperature with and without *E*. (c) The diagram of growth processes at different temperatures.

Post-nucleation growth process

After nucleation, the nuclei continue to grow with influx of molecules and cover the substrate. We obtained coverage as $\int P^h(z)dz$ ($z_0<z<\infty$) for the film peak. The coverage rate of films is calculated by the projected area of grains divided by the whole area. The largest coverage rate is at 273 K shown in Figure 3.6b. The electric field has no obvious effect on film coverage.

On top of the background of monotonic temperature dependence, there is a peak in the temperature dependence of $<z>$ between $T = 260$ and 285 K (Figure 3.6a). Naturally, this

can be related to the peak in the temperature dependence of the grain density. On the other hand, the peak position appears to be independent of the electric field, although the peak intensity is clearly enhanced by the electric field. Therefore, the electric field may affect not only the nucleation process (grain density), but also the growth of the crystallites, especially the shape of the grains, as observed by comparing Figure 3.3(e) and (f).

To further demonstrate whether the electric filed will facilitate the preferential growth, we define d_e as the equivalent diameter of a grain's projected area, $z_{\max}$ as the maximum height difference of the grain. Both d_e and $z_{\max}$ can be found once the grains are defined using the height threshold. The normal elongation ratio is:

$$\lambda = z_{\max}/d_e \tag{3.9}$$

The representative histogram of λ for temperature 273 K is shown in Figure 3.7a. The peak of λ is shifted from 0.132 to 0.22 by the electric field, indicating that the electric field indeed accelerated the growth along the out-of-plane direction for the temperature 273 K. The comparison of the mean λ for the electric field condition is plotted against the substrate temperature, as shown in Figure 3.7b. At higher substrate temperature (>270 K) the electric field induced a remarkable normal growth along the electric field direction. However, this kind of "electric" growth is not obvious for the lower temperatures.

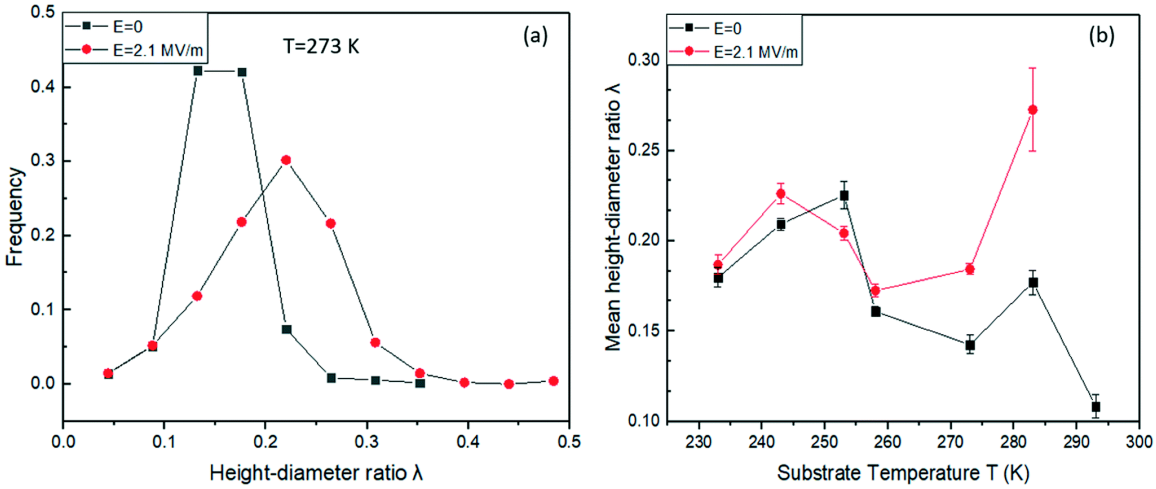

Figure 3.7 (a) The normalized histogram of the height–diameter ratio for the CA film deposited at 273 K. (b) The mean height–diameter ratio versus substrate temperature with and without the electric field.

The anisotropic growth of CA crystallites after nucleation is in agreement with the previous discussion for the nucleation process, where the electric field increases λ_n by increasing wetting angle θ. To quantitatively analyze its change, we assume that the grains have the shape of a spherical cap. At 283 K, λ is increased from 0.143 to 0.184 by the electric field (Figure 3.7b), corresponding to θ = 31.8° and 40.5° according to Eq. (3.7); $\phi(\theta)$ then increases by 2.45 times. On the other hand, from the fitting results in Table 3.1, Λ or $\phi(\theta)$ increases by 1.58 times. This agreement is fair considering that the final aspect ratio is also affected by the post-nucleation growth process.

In other words, the observation of the larger electric field effect on $\phi(\theta)$ than that analyzed in the nucleation process, suggest that the electric field also has a significant impact on the post-nucleation growth process. This effect appears to be larger at higher temperatures, according to Figure 3.7b. At high temperature, the surface diffusion is

enhanced by the thermal energy, which promotes post-nucleation growth. Therefore, the apparent larger effect of the electric field on the aspect ratio of the grains at higher temperatures is probably because of the more significant contribution of post-nucleation growth to the grain.

***In situ* electrical measurement of croconic acid thin films**

We performed in situ electrical measurement on CA thin films by exploiting the in-plane electrodes described in section 2.3.1. After depositing 995 nm thickness CA thin films on the IDE substrate (Figure 3.8) at 273 K, the electric displacement versus applied voltage, D-V_{app}, hysteresis loops were measured while the temperature was increased from deposition temperature (273 K) to 325 K at a constant rate of 0.2 K/min. All measurements were performed under high vacuum ($<10^{-6}$ Torr).

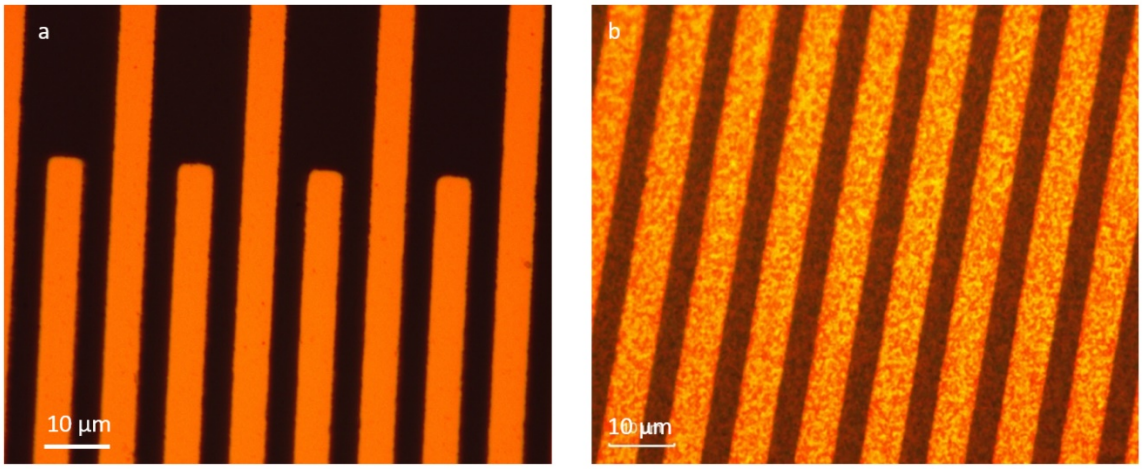

Figure 3.8 The morphology of (a) the IDE substrate and (b) CA thin films of 995 nm thickness on the IDE substrate by optical microscope.

In Figure 3.9, no D-E loop appears like typical ferroelectric features, i.e., negative $\frac{d^2D}{dE^2}$. Instead, they show typical shapes of Lissajous patterns from leaky capacitors under

triangle voltage waveform. The degree of expansion of loops can be reflected by the vertical intercept D_r in Figure 3.9b. The intercept depends mainly on the resistance rather than on the capacitance by the equation, $D_r = k_V \tau_t^2 / 16RA$, where k_V is the rate of increasing voltage, τ_t is the period of the triangle-wave voltage, A is the electrode area. Since the substrate resistance is much larger than that of the CA film, the variation of total resistance with temperature in Figure 3.9c is attributed to the contribution of CA films.

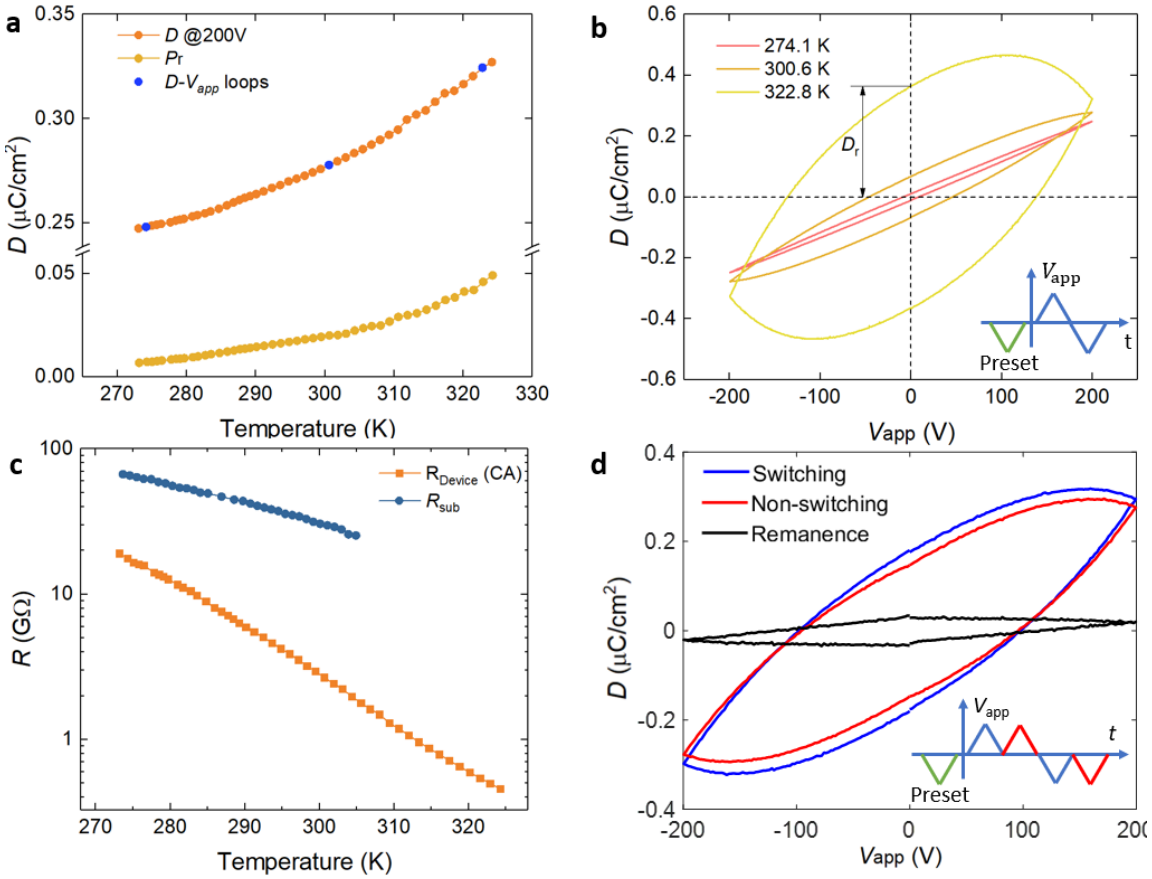

Figure 3.9 (a) The displacement at 200 V and the remanent polarization as a function of temperature. Remanent polarization P_r is acquired from the double-wave hysteresis loops. The blue spots mark the displacement corresponding to hysteresis loops in (b). (c) The

resistance of the device and the substrate as a function of temperature. (d) The double-wave hysteresis loop of CA at 321 K.

As temperature increases, in Figure 3.9a remanent polarization P_r only increases a bit, indicating a weak ferroelectricity in CA films. The increase in D_{max} is more significant than that in P_r, which is attributed to the large decrease in resistance. In others' work, ferroelectricity in CA films has been observed by local piezoresponse force microscopy (PFM)[50,76]. In our work, the hysteresis loops for CA films exhibit no ferroelectric features and the double-wave method shows small P_r. It is likely that the deposited CA films have very low crystallinity with crystal size of 50~100 nm which are not large enough to be measured by interdigitated electrodes with gap of 4 μm, and also the large leakage current screens the contribution of ferroelectric polarization. We note that the remanent polarization kept the same after annealing the CA film in vacuum at 325 K for 4 days.

3.4 Conclusions

In summary, we have studied the nucleation and growth behavior of croconic acid molecules under different substrate temperatures and the electric field. The heterogeneous nucleation could be described by classical nucleation theory. The mechanisms and parameters responsible for the nucleation rate with and without the electric field were quantitatively analyzed. We show that (1) The electric field shifts the peak position of the maximum nucleation rate toward the lower temperature. This is mainly due to the reduced transport barrier of nucleation from 0.19 eV to 0.14 eV, increased interface energy, and reduced equilibrium transition temperature from 303 K to

300 K by the electric field. (2) The electric field induces the preferred growth along the out-of-plane direction at higher temperatures. The anisotropic growth is consistent with the increased wetting angle of nuclei in the electric field. The D-V_{app} relationship for deposited CA films exhibit the characteristics of leaky capacitors. Weak ferroelectricity from the remanent polarization measurement in CA films may be attributed to low crystallinity of the films. These results provide insights into the effect of electric field on molecular crystal nucleation and growth on inorganic substrates, which could be utilized to improve the vacuum deposition process of organic films and achieve better surface morphology of organic films.

CHAPTER 4 THE DEPOSITION AND CHARACTERIZATION OF MOLECULAR FERROELECTRIC 2-METHYLBENZIMIDAZOLE

4.1 Introduction

The ferroelectricity in organic materials is in increasing demand in capacitor, piezoelectric, and memory devices as the lead- and rare-metal-free ferroelectric devices are required to be environment-friendly. The discovery of above-room-temperature ferroelectricity in single-component organic molecular crystals, such as croconic acid[5], 2-methylbenzimidazole (MBI)[6], in the 2010s has drawn much attention as they provide a low coercive field E_C and high remanent polarization P_r in contrast to commercially available ferroelectric polymer poly(vinylidene fluoride) (PVDF) and its related compounds. To date, poly(vinylidenefluoride-trifluoroethylene) (P(VDF-TrFE))[50] with a moderate P_s of ≈10 μC/cm^2 has to suffer from a high E_c of ≈500 kV/cm. Croconic acid has the highest recorded P_r of 21 μC/cm^2 among organic ferroelectrics and a small E_c of about 14 kV/cm owing to its O···HO hydrogen-bond network which forms single polar axis[5]. MBI single crystal with a P_r of 5.2 μC/cm^2 and E_c of 11 kV/cm has two polar axes[6].

Polycrystal croconic acid has large leakage current due to the adhesion of water molecules in air[50,51,76], which impede its development in future electronic devices. In contrast, MBI as another candidate for organic ferroelectric materials is chemically inert in air and has modest acidity[77]. Polarization switching over two dimensions in MBI is significantly advantageous for the macroscopic polarization of randomly oriented

polycrystalline thin films, compared with other uniaxial polarity of organics[6].

So far, MBI thin films have been fabricated successfully by two techniques, i.e. solution shearing[77] which produced single-crystalline thin films, and evaporation method from a MBI-ethanol solution[78] which is cheap and simple. However, the fabrication of MBI thin films into desired devices still faces many challenges. MBI precipitated from solution is inclined to inherently form needle-shaped crystals rather than desired plate, making the surface very rough. For instance, the surface of the single-crystal thin film with nominal thickness of 1 μm has some protrusions with height of ≈1 μm.

Here, we fabricate the continuous crystalline ferroelectric MBI thin films by the physical vapor deposition (PVD) method. Thermal sublimation in vacuum we utilized here, as one of PVD methods, have the advantages of precise thickness control, possibility for ultrathin organic film production, and being contamination-free[79]. By heating MBI power source in high vacuum, MBI gas molecules are deposited on an interdigitated Pt electrode (IDE) which is cooled down to 230 K. Then the thin-film devices are annealed slowly up to room temperature. Since this is the first time that MBI thin films have been deposited by the PVD method, we elaborate on the whole process in the Methods section.

Most of the studies have measured the ferroelectric and dielectric properties of organic materials by performing *ex situ* measurements. Although this may be the simplest approach to study the ferroelectric materials, some inherent properties of materials may be affected by the environments, e.g., CA is sensitive to the moisture in air. Therefore, measuring ferroelectric properties *in situ* is preferred. In this study, we performed *in situ* electrical characterization by employing IDE and the multidomain ferroelectric materials,

viz. polycrystalline MBI during deposition and heating processes, which provided considerable insights into the emergence and evolution of the ferroelectricity of organic ferroelectric materials. During the deposition process, the electric displacement versus applied voltage, D-V_{app}, hysteresis loops of IDE capacitors is measured as a function of thickness, from which the dependence of the capacitance on the film thickness is derived. The capacitance of interdigitated electrodes for the multi-layered structure is quantitatively described. During the annealing process following the deposition, D-V_{app}, hysteresis loops are measured as a function of substrate temperature, from which the amorphous to crystal phase transition is demonstrated and the transition temperature T_g is determined. The kinetics of the anisothermal amorphous-to-crystalline phase transition for MBI is discussed, revealing that the nucleation rate is increasing with temperature and MBI has a very low activation energy for the phase transition.

4.2 Experimental

Film sample fabrication and electrical measurement. The substrates with interdigitated Pt electrodes on glass were purchased from Metrohm; the electrode width and gap between electrodes are 6 and 4 μm respectively, as shown in Figure 2.9; there are 125 pairs of electrodes of 6760 μm long. The physical vapor deposition was performed in high vacuum (< 10^{-6} torr) using a EvoVac system (Angstrom Engineering Inc.) equipped with thickness monitor; the schematics of system is shown in Figure 2.1. Deposition was carried out with substrate temperature 230 K and 273 K, rate 1.8 and 1.2 nm/min, for MBI and CA respectively. The melting point of MBI is 175-177 ℃. The temperature of the thickness monitor was kept the same as the substrate during deposition. After the deposition finishes, the substrate is heated at an average rate of 0.2 K/min in high vacuum

(< 10^{-6} torr) and in ≈3 torr N_2 environment for MBI. It is confirmed that the change of pressure has no effect on the hysteresis loops and D_{max}. D-V_{app}, I-V_{app} loops were measured with Precision RT66C Ferroelectric Tester (Radiant Technologies, Inc.). The frequency was set to at 1 Hz to ensure saturated polarization. Before deposition, the D-V_{app} loop for the substrate was measured to ensure no breakdown of electrodes and exhibits the behavior of a linear capacitor. The capacitance of the device was acquired from the fitting of leakage polarization in double-wave hysteresis measurements (Figure 4.1). In terms of a lossy capacitor for which leakage resistance is in parallel with the capacitance, when a triangle waveform voltage is applied, $V_{app} = k_V t + V_0$, the relationship between the electric displacement and applied voltage can be described by the following equation,

$$D = \frac{V_{app}^2}{2RAk_V} + \frac{C}{A}V_{app} - \frac{V_0^2}{2RAk_V} - \frac{C}{A}V_0 + D_0 \tag{4.1}$$

where C is the capacitance of the lossy capacitor, R the resistance, D_0 the initial displacement, A the electrode area. By fitting Eq. (4.1) with the non-switching part of the data, $C_\uparrow$ and $C_\downarrow$ can be obtained, and the final capacitance is the average of $C_\uparrow$ and $C_\downarrow$. The fitted mean C has the similar value with the capacitance measured by the impedance analyzer shown in Figure 4.1.

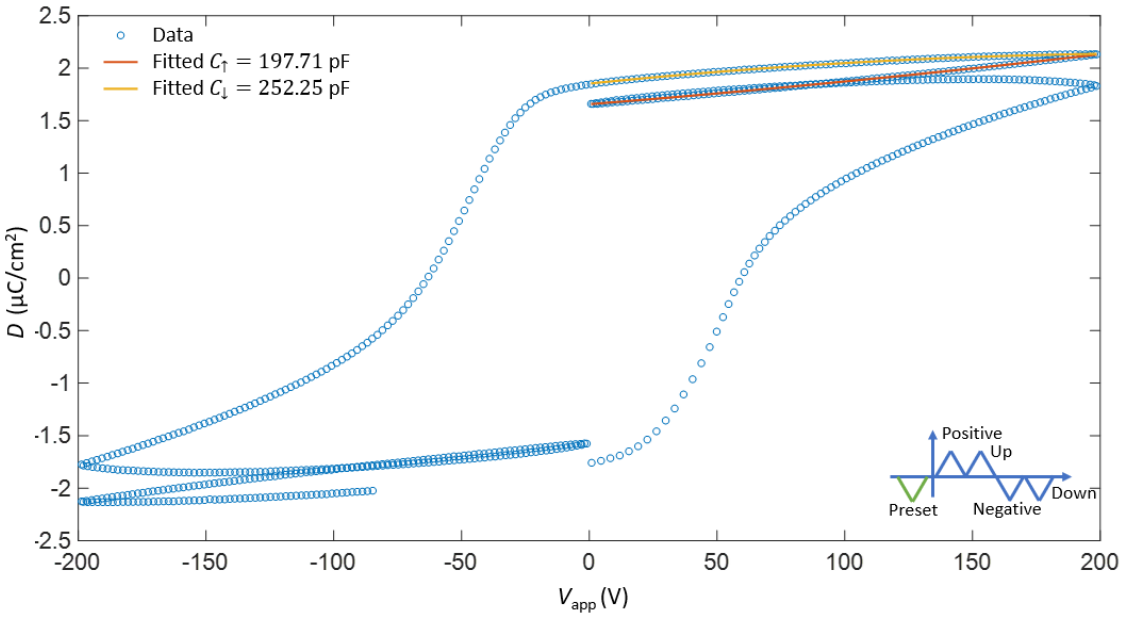

Figure 4.1 The hysteresis loop measured by the double-wave method. The mean capacitance is 224.98 pF which is close to the capacitance measured by impedance analyzer (227.33 pF).

Morphology and structural Characterization. X-ray diffraction pattern (XRD) was obtained with the PANalytical Empyrean Diffractometer at room temperature in atmosphere by θ-2θ scanning. The film thickness after deposition was also measured by the DektakXT stylus profiler (Bruker) to calibrate the thickness monitor. Atomic force microscopy (AFM) analysis was performed in air by using a Bruker Dimension ICON SPM in peak force tapping mode. Optical microscopy (OM) images with height profiles were obtained with Keyence laser scanning microscope VK-X200K. The MBI sample with thickness of 4.28 μm for XRD and OM measurements is deposited at 236 K on the IDE substrate; for AFM measurement the film was deposited at 253 K on the Al_2O_3 substrate.

The analytical model of the IDE sensor. The capacitance of the interdigital capacitor is given by[80]:

$$C_{\mathrm{IDC}} = (N-3)\frac{C_{\mathrm{I,IDC}}}{2} + 2\frac{C_{\mathrm{I,IDC}}C_{\mathrm{E,IDC}}}{C_{\mathrm{I,IDC}} + C_{\mathrm{E,IDC}}} \tag{4.2}$$

$$C_{\mathrm{I,IDC}} = \varepsilon_0 L\left(\frac{K(k_{\mathrm{I}\infty})}{K(k'_{\mathrm{I}\infty})} + (\varepsilon_1 - 1)\frac{K(k_{\mathrm{I},1})}{K(k'_{\mathrm{I},1})} + \varepsilon_{\mathrm{S}}\frac{K(k_{\mathrm{I}\infty})}{K(k'_{\mathrm{I}\infty})}\right) \tag{4.3}$$

$$C_{\mathrm{E,IDC}} = \varepsilon_0 L\left(\frac{K(k_{\mathrm{E}\infty})}{K(k'_{\mathrm{E}\infty})} + (\varepsilon_1 - 1)\frac{K(k_{\mathrm{E},1})}{K(k'_{\mathrm{E},1})} + \varepsilon_{\mathrm{S}}\frac{K(k_{\mathrm{E}\infty})}{K(k'_{\mathrm{E}\infty})}\right) \tag{4.4}$$

where N is the number of electrodes, L is the length of the electrode fingers (Figure 4.2), ε_0 is the vacuum permittivity, ε_1 and ε_{S} are the dielectric constant of film and substrate respectively, $K(k)$ is the complete elliptic integral of first kind with modulus k, k' is the complementary modulus through the equation $k' = \sqrt{1-k^2}$, and

$$k_{\mathrm{I}\infty} = \sin\left(\frac{\pi}{2}\eta\right) \tag{4.5}$$

$$k_{\mathrm{I},1} = \mathrm{sn}(K(k)\eta, k)\sqrt{\frac{\left(\frac{1}{k}\right)^2 - 1}{\left(\frac{1}{k}\right)^2 - [\mathrm{sn}(K(k)\eta, k)]^2}} \tag{4.6}$$

$$k_{\mathrm{E}\infty} = \frac{2\sqrt{\eta}}{1+\eta} \tag{4.7}$$

$$k_{\mathrm{E},1} = \frac{1}{\cos h\left(\frac{\pi(1-\eta)}{8r}\right)}\sqrt{\frac{\left[\cos h\left(\frac{\pi(\eta+1)}{8r}\right)\right]^2 - \left[\cos h\left(\frac{\pi(1-\eta)}{8r}\right)\right]^2}{\left[\cos h\left(\frac{\pi(\eta+1)}{8r}\right)\right]^2 - 1}} \tag{4.8}$$

$$k = \left(\frac{v_2(0, \exp(-4\pi r))}{v_3(0, \exp(-4\pi r))}\right)^2 \tag{4.9}$$

where $\mathrm{sn}(K(k)\eta, k)$ is the Jacobi elliptic function of modulus k, v_2 and v_3 are the Jacobi theta functions, η is the metallization ratio through equation $\eta = W/(W+G)$, W is the finger width, G is the gap (Figure 4.2), $r = h/(2W+2G)$, h is the thickness of the film. In summary, the capacitance of IDE sensor is a function of η, r, ε_1 and L (i.e., $C_{\mathrm{IDC}} = C_{\mathrm{IDC}}(\varepsilon_1, L, \eta, r)$).

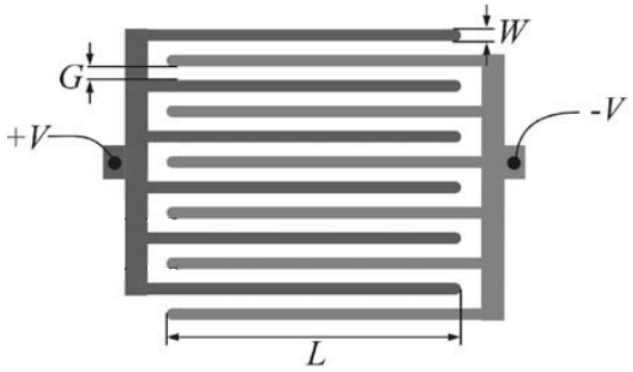

Figure 4.2 The dimensions of the interdigitated electrodes.[80]

4.3 Results and Discussion

Low-temperature deposition of the amorphous phase.

MBI and CA films were deposited at temperature T_{dep} = 230 K and 273 K respectively on the IDE substrates, while the electrical properties were monitored *in situ* (see the "Experimental" section). All *D*-V_{app} relations of MBI films are consistent with linear behavior of capacitors while those of CA are broadened by small leakage current, as shown in Figure 4.3, indicating no ferroelectricity during the low-temperature deposition process. The measured resistance at 200 V is 125 GΩ and 16.5 GΩ for the MBI/IDE device with thickness of 4.6 μm (230 K) and CA/IDE device with thickness of 732 nm (273 K) respectively. Because the origins of ferroelectricity of MBI and CA are long-range order of the hydrogen bonds in the crystalline phases[5,6], the as-deposited films

appear to be amorphous with no long-range structural order; this is expected for low-temperature deposition of MBI and CA whose sublimation temperatures in high vacuum are around 353 K and 433 K respectively. The quenching of molecular vapor onto the low-temperature substrates suppresses the motion of molecules, leaving no sufficient time and kinetic energy for crystallization.

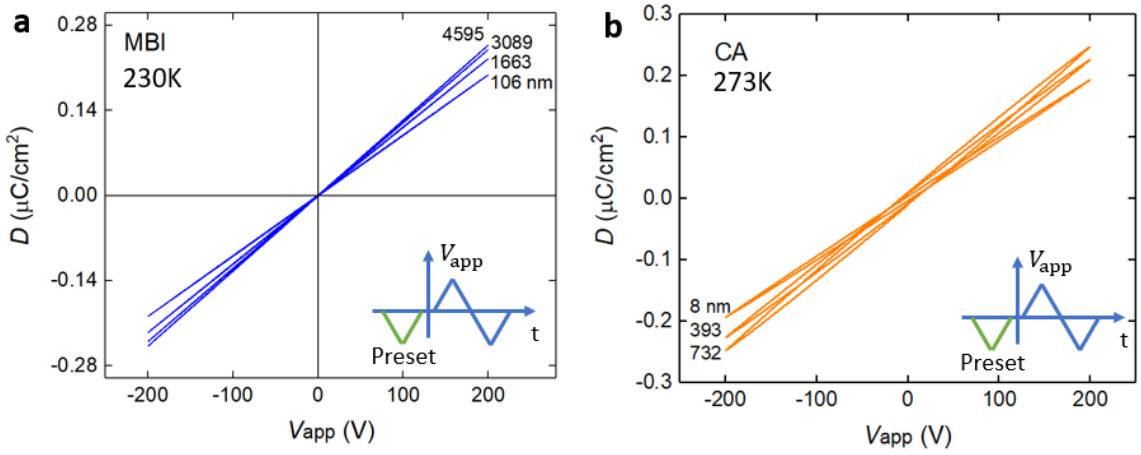

Figure 4.3 The D-V_{app} hysteresis loops for (a) MBI measured at 230 K, (b) CA measured at 273 K. All loops were measured in situ at constant temperature in high vacuum ($<1 \times 10^{-6}$ Torr) during deposition process at different thickness.

As the thickness of the films increases, the slope of the D-V_{app} relations for both MBI and CA increases (Figure 4.3), corresponding to increasing capacitance (Figure 4.4a). Multiple MBI samples with different final thickness were measured and the thickness dependence of capacitance distinguishes MBI from CA; the latter increases much faster. The capacitance of devices in Figure 4.4a includes three parts in parallel (see Figure 4.4b): C_{glass} from the glass substrate, C_{film} from the film, and C_{vacuum} from the vacuum contribution of the upper half plane ($C = C_{glass} + C_{film} + C_{vacuum}$). When the film thickness increases, C_{film} increases while C_{vacuum} decreases, leading to higher C since

the dielectric constant of the films is always higher than that of vacuum.

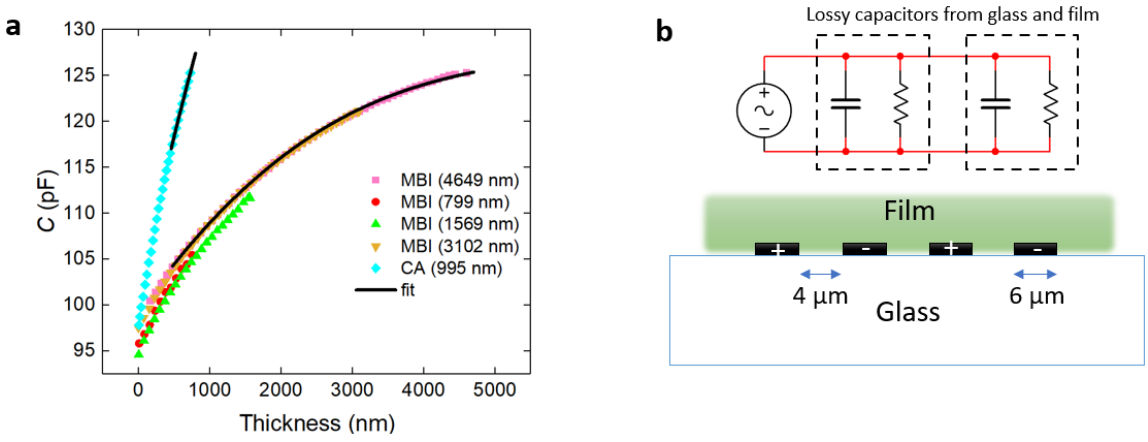

Figure 4.4 (a) Capacitive response of IDE devices for MBI or CA films with different final thickness. The fit was performed with the partial-capacitance model. Note that this model applies for r>0.05. (b) Schematic of the IDE devices and its equivalent circuit.

To separate the contributions to the device capacitance, we analyzed the thickness dependence using the partial-capacitance model[80,81]. Essentially, the capacitance is a function of the dielectric constant of the films, the electrodes length, L, and of two dimensionless geometric parameters: η as the ratio between the electrodes gap and finger widths, and r as the ratio between the thickness of the film and the IDE spatial period. The function $C(\varepsilon_{\mathrm{MBI}}, L, \eta, r)$ is summerized in the Experimental section. Fitting the thickness dependence of the device capacitance in Figure 4.4a, the dielectric constants are found as $\varepsilon_{\mathrm{MBI}}$=2.93, $\varepsilon_{\mathrm{CA}} = 7.28$, and $\varepsilon_{\mathrm{sub}}$ =5.63 for amorphous MBI, amorphous CA, and the glass substrates respectively. Notice that $\varepsilon_{\mathrm{MBI}}$ is much smaller than the single-crystal MBI value 33.2 (measured at 1 Hz, 230 K)[6], indicating the effect of long-range ferroelectric order.

Crystallization and emergence of ferroelectricity in post-deposition annealing.

After the deposition of MBI at 230 K, the films were heated up to 305 K at a 0.2 K/min rate, in a 3 Torr N_2 gas environment to minimize sublimation. Based on our experience, MBI film will sublime away if heating to room temperature in vacuum. Increasing the pressure from vacuum to 3 Torr has no effect on the hysteresis loop, and D_{max} (D measured at 200 V) keeps the same. In addition to the D-V_{app} relation, remanent polarization P_r and capacitance were measured using the double-wave method. As the temperature increases, the D-V_{app} relations undergo a transition from the reversible linear behavior to the typical ferroelectric hysteresis loops as shown in Figure 4.5a for a 3.1 μm film. To quantify the transition, we plot in Figure 4.5b the temperature dependence of P_r and D_{max}. D_{max} includes the contributions of both the dielectric layer and the ferroelectric layer of the film. Similar trends of P_r and D_{max} in Figure 4.5b indicate in the process of the phase transition; the contribution of ferroelectric polarization is much larger than the dielectric polarization for MBI films.

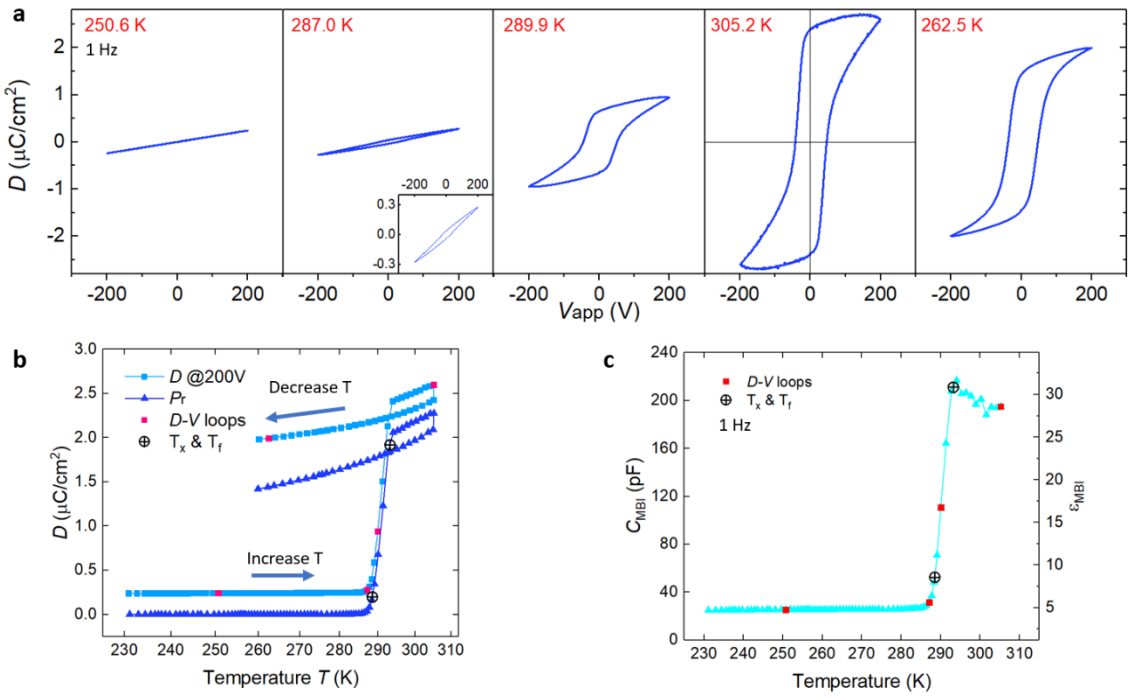

Figure 4.5 Panel (b) shows variation of the maximum electrical displacement and remanent polarization with the temperature immediately after deposition. The correspsonding D-V_{app} loops at 1 Hz, different temperatures are shown in (a). The inset in (a) is the zoomed plot. (c) Variation of capacitance of the MBI film with temperature. Thickness of the sample is 3.1 μm.

Obviously, the transition occurs in a narrow range near 290 K. Since ferroelectricity relies on long-range structural order in the crystalline phase, this transition of D-V_{app} relation suggests an amorphous-to-crystalline structural transition, or crystallization from the amorphous phase. In view of the definition of glass transition[82], the crystallization temperature T_x (whose definition is shown in Figure 4.6) for the MBI film of 3.1 μm is 288.5 K; the corresponding end temperature T_f of the transition is 293.2 K. We note that the crystallization temperature T_x depends on many factors, such as film thickness[83], heating rate[84], and deposition temperature[85]. Our results indicate that T_x of MBI increases

linearly with the film thickness (Figure 4.7). It is possible that interfacial energy between substrate and the film play an important role. It was also found that T_x increases with decreasing film thickness for some polymers when the interfacial interaction is strongly attractive[83,86].

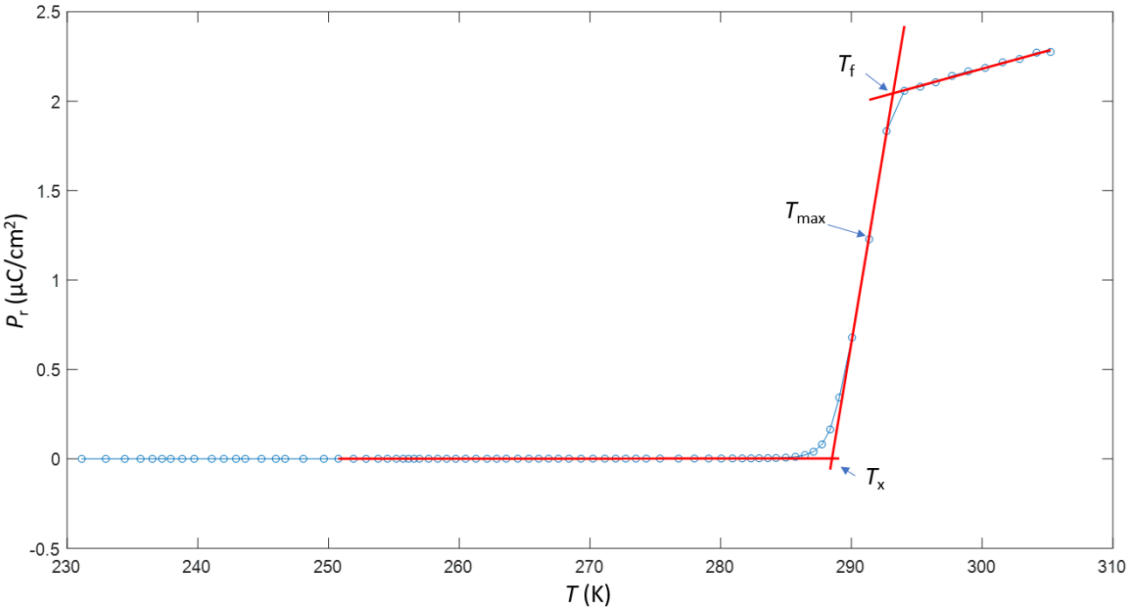

Figure 4.6 The crystallization temperature T_x is defined as the temperature at the intersection of the red regression lines which are the linear sections below and above T_x. T_f is the end temperature of the crystallization. T_{max} is the temperature with the largest derivative of P_r with respect to T.

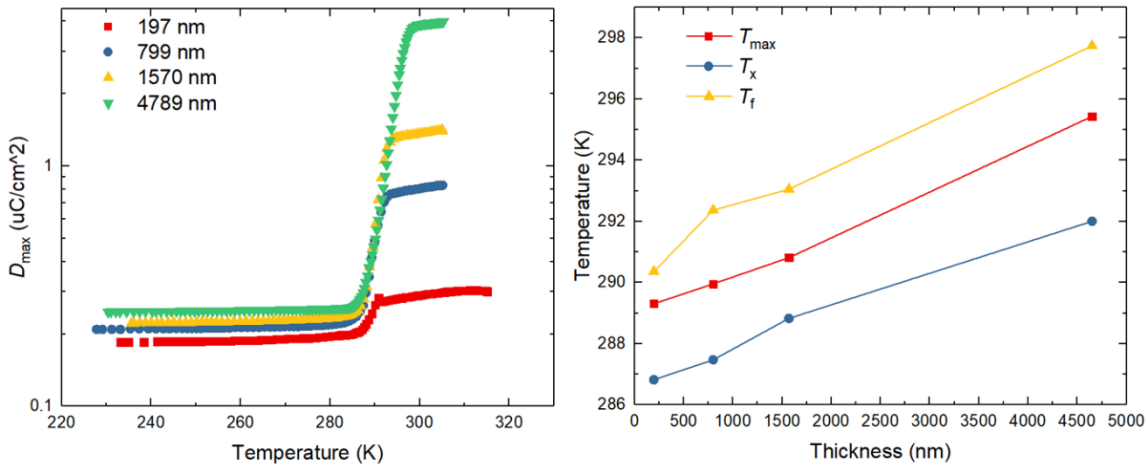

Figure 4.7 Variations of crystallization temperature with the thickness. T_x and T_f are the intersection points of the linear parts of the $D_{max} - T$ curves. T_{max} is the temperature with the largest transition rate.

As the temperature increases up to T_x, D-V_{app} loop opens up slightly, consistent with leaky capacitor behavior of amorphous phase, suggesting the reduction of resistance at higher temperature. During the crystallization from 288.5 K to 293.9 K, ferroelectric polarization increased rapidly due to the crystal nucleation and growth. Meanwhile, the hysteresis loops also exhibit visible leaky behaviors. After 293.9 K, the remanent polarization P_r increases linearly and slowly, reaching 2.60 μC/cm^2 at 305 K. The hysteresis loop at 305.2 K, 1 Hz has an averaged coercive voltage (V_c) 44.6 V and an effective $E_c \approx 87.1$ kV/cm.

After the substrate temperature reaches 305 K, the film was annealed at 305 K for 7.9 hours in 3 Torr N_2 environment. Measurement after the annealing shows a small reduction of P_r and D_{max} (Figure 4.5b), which is consistent with the small fraction of film sublimation (with a rate of 5.7 nm/h in average) indicated by the thickness monitor.

Temperature dependence of P_r and D_{max} were also plotted in Figure 4.5b during the cooling from 305 K at a constant rate of 0.5 K/min. Above T_f, P_r and D_{max} reduce linearly with a rate similar to that during the warming process. This reversible behavior indicates that the temperature dependence is intrinsic to ferroelectric MBI crystal. Further cooling through T_x, continues the near-linear reduction of P_r and D_{max}, in contrast to the irreversible phase transition in this temperature range during the warming process. In most ferroelectrics, P_r decreases with temperature since it is expected to vanish at the ferroelectric-to-paraelectric phase transition temperature. However, for proton-transfer type ferroelectricity that relies on long-range order of hydrogen bonds, like MBI and CA, since the elongation of hydrogen bonds dominates the thermal expansion, a near-linear relationship between in-plane strain and ferroelectricity is expected[87], which has also been observed previously in MBI[88] and CA.[5]

Electrical capacitance and resistance of MBI films. As shown in Figure 4.1, the MBI film capacitance was measured by fitting the non-switching part of the D-V_{app} relation from the double-wave hysteresis measurement and subtracting the substrate capacitance. The device resistance (R_{device}) at 200 V and substrate resistance were obtained from I-V measurements, as shown in Figure 4.9. The film resistance (R_{MBI}) and the substrate resistance (R_{sub}) are in parallel, so R_{MBI} were calculated from R_{device} and R_{sub} which was measured before deposition of films (Figure 4.9). All measurements were in situ conducted on the same sample in sequence during the annealing process.

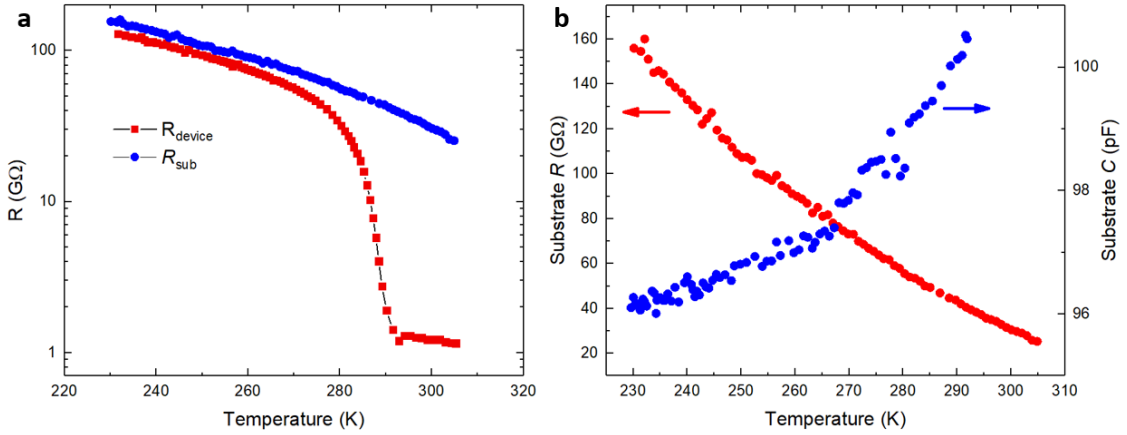

Figure 4.8 (a) The variations of resistance of the device and the substrate measured at 200 V with the increasing temperatures. (b) the substrate resistance and capacitance as a function of temperature. The capacitance of the substrate was measured before the deposition.

It is evident from the data in Figure 4.5c and Figure 4.9a that both the drastic decline in resistance and the sharp increase in capacitance reflect the structural transition in the films. Before the phase transition T_x, the dielectric constant of the amorphous film increases slightly with temperature (Figure 4.5c) which is common in amorphous materials[89]. With higher kinetic energy by thermal excitation, the bound charges in amorphous films are easier to follow the change of the external electric field. During the phase transition, the capacitance increases drastically with temperature due to the much larger dielectric constant of crystalline MBI than that of amorphous MBI. In contrast to crystalline MBI with the long-range order, the polarizability of protons is greatly reduced due to the disordered positions of molecules in amorphous states. After the completion of the phase transition, C_{MBI} decreases as T increases. This is likely due to the prominent ripening of crystals at high temperature. Svinarev's research[88] indicated that the dielectric

constant of single crystal MBI is lower than polycrystal MBI. After the crystalline MBI sample is settled at room temperature (RT) for several days, the capacitance of the MBI film we measured again with the same method increases with the temperature increase (Figure 4.10), which is in agreement with the literature[90]. The reasons for the decline of capacitance with the increase of temperature need more investigation.

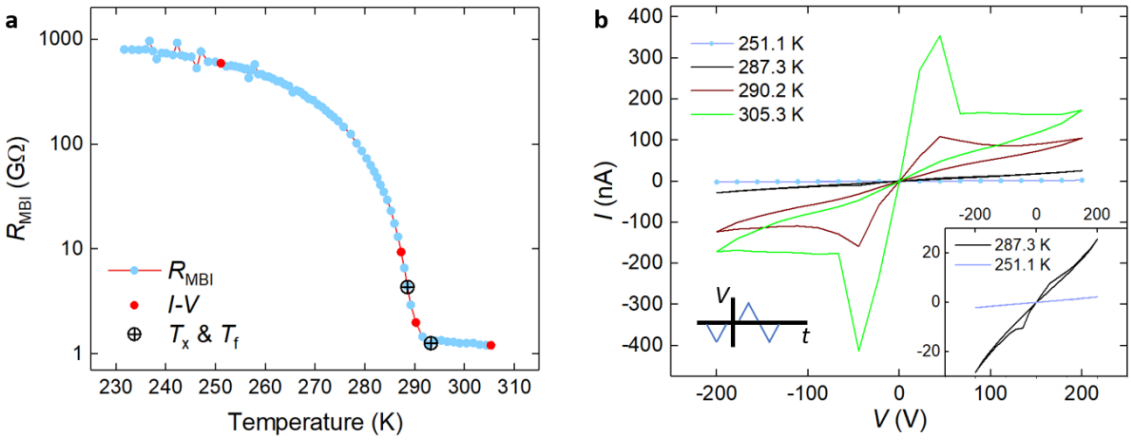

Figure 4.9 (a) Variation of resisitance of the MBI film with temperature during phase transition. The corresponding *I-V* curves at different temperatures are shown in (b). The inset in (b) is the close up view of the 251.1 K and 287.3 K data in (b).

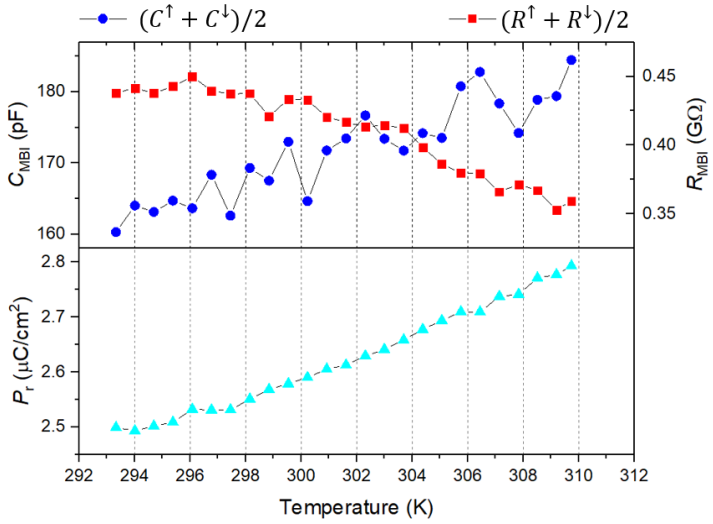

Figure 4.10 Variations of capacitance and resistance of the MBI film with the temperature. Both C_{MBI} and R_{MBI} are obtained by fitting the nonswitching part of double-wave hysteresis loops.

Current–voltage (*I–V*) curves were collected *in situ* from the same sample under a sweeping rate *v* of ≈0.55 V/s (equal to 0.00069 Hz) as temperature increased. In Figure 4.9b, it is notable that the polarization switching current peaks appear at 287.3 K and become more and more prominent with temperature. The temperature range with current peaks is consistent with the range for the phase transition. Below 283 K, most leakage current is from glass because the resistance of amorphous MBI is much larger than that of glass substrate shown (Figure 4.8). The *I-V* curves at low temperatures before crystallization exhibit linear ohmic behaviors in Figure 4.9b inset. The decrease in resistance with increasing temperature for amorphous MBI can be attributed to thermal activation of charge carriers. The resistance of MBI is 4.43 GΩ and 1.26 GΩ respectively at T_x and T_f in Figure 4.9a. Above T_f (293.1 K), most of amorphous materials has transformed to crystals; the film resistance decreases slightly with increasing

temperature.

Morphology of MBI films. After deposition and annealing, MBI films were examined by optical microscope, AFM, and laser scanning microscope in atmosphere at room temperature. MBI films are composed of radially polycrystalline aggregates with an outer spherical envelope (Figure 4.11a), termed as spherulite.[91] In Figure 4.12c, the center of one spherulite is a single crystal which has the largest height. In terms of the spherulitic growth behavior, which is often found in polymer film growth[92], some single crystals primarily nucleate from amorphous film, then grow through the mechanism of small-angle branching, in which numerous needle-like or fibrous crystals spike outward from the nuclei. The fastest growth direction of MBI crystals, which becomes the radial growth direction (Figure 4.11d), is parallel to the crystallographic c-axis, found by synchrotron X-ray diffraction measurements[77]. The needle shape of crystal can be explained by simply considering the effects of the interfacial energy of different crystal planes. The growth of crystal is always inclined to minimize the (orientation-dependent) interfacial energy integrated over the entire surface.[93] Therefore, the fastest growth rate is along the facet direction with the largest interfacial energy. As shown in Figure 4.12a, there are much more Van der Waals bonds between carbon atoms along (001) plane than along (110) plane, so molecules are inclined to packing themselves on the (001) plane with the fastest growth rate.

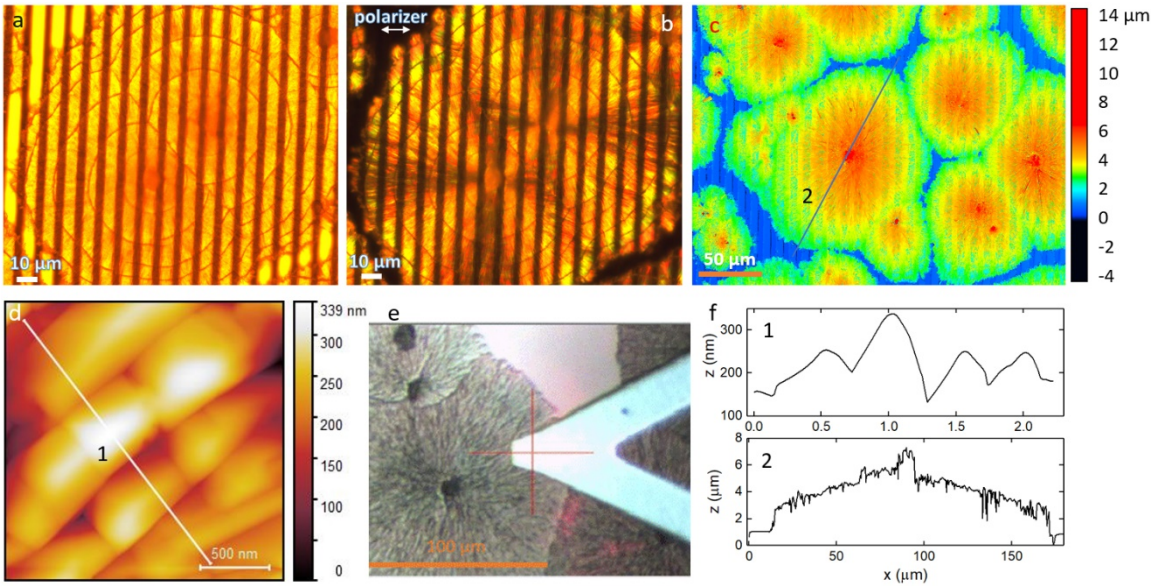

Figure 4.11 Morphology of crystalline MBI films. a-c) MBI crystals deposited on IDE substrate at 236 K, d-e) on Al2O3 substrate at 253 K. a,b) Optical images without and with crossed polarizers. c) Height image of the MBI film by laser scanning. d) AFM image of the assembled spherulite of MBI at the cross position in e). f) Height profiles along the line 1 in d) and line 2 in c).

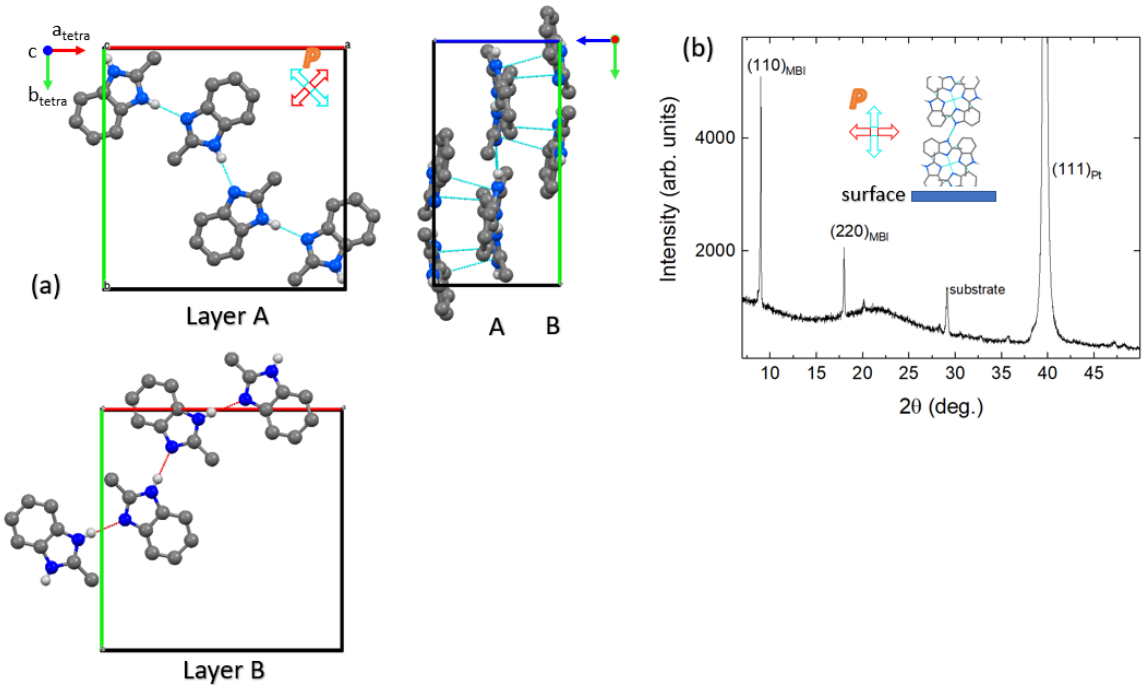

Figure 4.12 (a) Schematic illustration of molecular packing and hydrogen bonding in a MBI crystal lattice. Principal polarization axes (hydrogen bonds) run parrelel to either $[110]_{tetra}$ or the crystallographically equivalent $[1\bar{1}0]_{tetra}$ direction. Light blue dash line represents the short contact with the interatomic distance lower than the sum of Van der Waals radii. b) XRD pattern of the MBI film with out-of-plane diffraction vector. The film thickness is 4.28 μm.

The pseudotetragonal axis (c-axis) in the majority of crystallites is in the plane (Figure 4.12a), which is also indicated by the X-ray diffraction measurement (Figure 4.12b). Two polar axes are either normal to the surface or in the surface plane. The direct reason for the preferred orientation along (110) plane in our films is that the emergent nuclei has much larger in-plane growth rate than the out-of-plane one. MBI crystal itself has largely anisotropic growth rate and the out-of-plane growth is constrained by the lack of molecule transport from its surrounding amorphous phase. On the other hand, the density

of nuclei should be small so that there is enough space for nuclei to intergrow toward each other. Preferred orientation may be a unique characteristic of low-temperature PVD in comparison with other deposition methods. For instance, vapor evaporation at room temperature in air is inclined to deposit crystalline nuclei rather than amorphous molecules on the surface,[29] so it produces more randomly oriented films.[78]

When the sample were observed under cross-polarized microscope (Figure 4.11b), the dimming cross, i.e., the "Maltese Cross" appeared in each spherulite. MBI crystals are uniaxial birefringent materials with the optic axis along c-axis, i.e., the radial direction in Figure 4.11b. Defining α as the angle between the optical c axis of the crystal and the polarizer axis, there will be no transmitted light if β is $n\left(\frac{\pi}{2}\right)$, where n is any integer. And the maximum light strength is expected when $\beta = \frac{\pi}{4} + \frac{n\pi}{2}$. Therefore, the dark rays of the crosses appear in the crystals where the optic axes are either parallel or perpendicular to the direction of polarizer. We note that the surface of crystalized MBI films is very rough with the largest height difference of ≈8 μm for films of thickness 4.28 μm (Figure 4.12f).

Kinetics of the anisothermal amorphous-to-crystalline phase transformation in MBI. Phase transformation is usually treated as a process of nucleation and grain growth, involving two parameters, time (t) and temperature (T). Under constant temperature, the kinetics of the isothermal phase transformation can be described by the Johnson-Mehl-Avrami (JMA) equation[34,85], i.e.,

$$f = 1 - \exp\left[-\left(\frac{t}{\tau}\right)^n\right], \tag{4.10}$$

where f is the fractional degree to which transformation has taken place by time t, n is the

Avrami exponent whose value depends on the characteristics of nucleation and on the dimensionality of the crystal growth, τ is the relaxation time satisfying an Arrhenius-type-dependence upon temperature[94], i.e.,

$$\tau = \tau_0 \exp\left(\frac{E_\mathrm{a}}{k_\mathrm{B}T}\right), \tag{4.11}$$

where τ_0 is a temperature-independent pre-exponential factor, E_a is the activation energy, k_B is the Boltzmann constant. It is easy to use Eq. (4.10) to investigate the isothermal kinetics since there is only one variable. Once temperature varies with time, the situation becomes more complex. When temperature varies linearly with time, i.e., under isokinetic condition ($dT/dt = \mathrm{const}$), the problem can be solved by combining Eq. (4.10), Eq. (4.11) and Eq. (4.12),

$$T = T_0 + k_T t \tag{4.12}$$

$$f(T) = 1 - \exp\left[-\left(\frac{T - T_0}{k_\mathrm{T}\tau_0 \exp\left(\frac{E}{k_B T}\right)}\right)^n\right] \tag{4.13}$$

where T_0 is the initial temperature, k_T the constant rate at which temperature varies with time. In our case, k_T is 0.2 K/min.

Most research[34,95] use the variation of conductivity or capacitance to express the percentage of the crystalline phase. But in cases where conductivity or capacitance has non-linear relationship with temperature, this method cannot accurately characterize the transformation kinetics. Since MBI crystals have ferroelectricity, it seems more appropriate to use normalized remanent polarization to reflect the degree of phase transformation. On the other hand, the remanent polarization of crystals also varies almost linearly with temperature as shown in the range of decreasing temperatures in

Figure 4.5b. So, we firstly fit the relationship $P_r^d(T)$ with a custom function, $P_{\mathrm{r}}^{\mathrm{d}}(T) = 0.2763\exp(0.006261 * T) + 7.315 * 10^{-10}\exp(0.06409 * T)$, as shown in Figure 4.13a inset. All remanent polarization values are normalized to those at 300 K through the equation, $P_r'(T) = P_r(T) * P_{\mathrm{r}}^{\mathrm{d}}(300)/P_{\mathrm{r}}^{\mathrm{d}}(T)$. The crystalline fraction is expressed as, $f = P'_{\mathrm{r}}/P'_{\mathrm{r0}}$, where P'_{r0} is the maximum value among $P'_{\mathrm{r}}(T)$. The relationship $f(T)$ is plotted in Figure 4.13a.

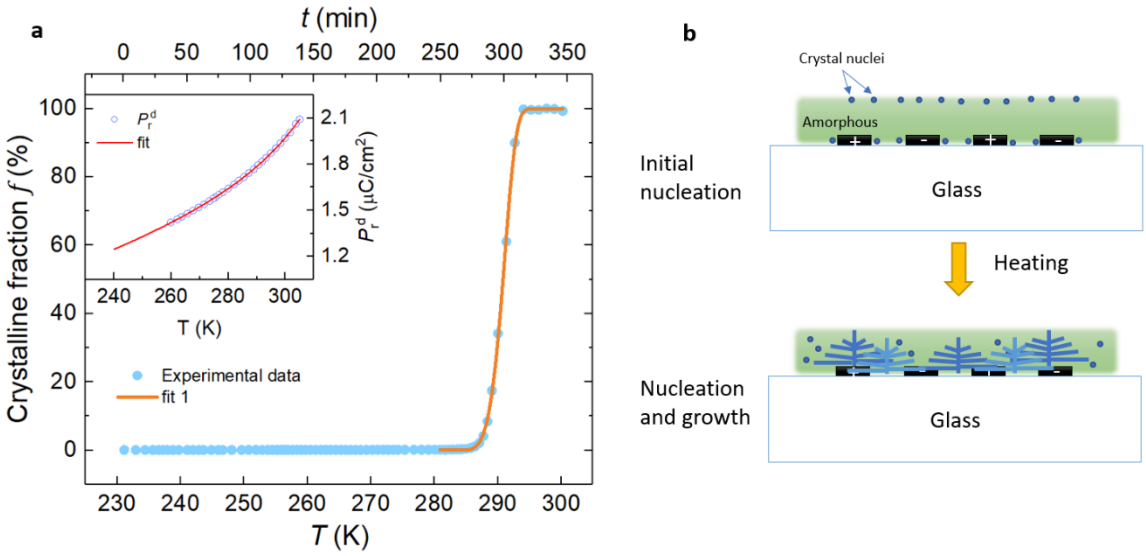

Figure 4.13 (a) Variation of crystalline fraction with temperature during annealing. The inset in (a) is the variation of remanent polarization with temperature after finishing of phase transition, corresponding to the part in decreasing temperature in Figure 4.5b. (b) Schematics of the crystal nucleation and growth from amorphous state.

The transformation behavior with the temperature is fitted using Eq. (4.13) which assumes that the Avrami exponent (n) and the activation energy (E_a) are independent of temperature. The fit in Figure 4.13a is fairly good with the squared norm of the residual of 9.72×10^{-4}. The fit parameters are shown in Table 4.1.

Table 4.2 Fitting parameters of Eq. (4.13) used to describe $f(T)$.

	E_a (eV)	n	T_0 (K)	$k\tau_0$ (K)
Fit 1	0.21	4.21	283.4	0.0021

The activation energy E_a is the minimum kinetic amount of energy which molecules must acquire to organize themselves. Comparing with the activation energy of other materials in Table 4.2, MBI molecules ($C_8H_8N_2$) have very small activation energy (0.21 eV) reflecting the fact it is much easier to crystalize from the amorphous state than inorganics and polymers with big molecules as building units. The parameter τ_0 in the fitting is a pre-exponential factor, which may not produce useful physical insights. T_0 is the theoretical starting temperature for transformation.

Table 4.2 Properties of some amorphous materials

Materials	Crystallization temperature T_x (K)	Activation energy in the amorphous-to-crystalline phase transition (eV)
TaSi2 thin films[95]	573	1.85
$Ge_2Sb_2Te_5$ films[34]	398	3.2
Si films[85]	873	3.8
Rubrene[92] ($C_{42}H_{28}$)	323	0.78
MBI	287	0.21

The Avrami exponent n is useful to probe the transformation process. Avrami et. al developed a general equation for transformation kinetics for three-dimensional growth[32],

$f = 1 - \exp\left[\eta \Upsilon_1 \Upsilon_2 \Upsilon_3 \int_0^t I(t-\tau)^3 \mathrm{d}\tau\right]$, where η is a shape factor, Υ_i the anisotropic growth rate, I the nucleation rate. Eq. (4.13) is a special case deduced from the general equation. If the nucleation rate is a constant, the exponent *n* in Eq. (4.13) should be equal to 4 derived from the general equation. With an increasing nucleation rate, *n* will be larger than 4. In our experiments, the exponent *n* for MBI is 4.2, indicating as temperature increases the nucleation rate is also increasing. On the other hand, initial nucleation occurs preferentially in sites with high interfacial energy or defects and random nucleation will appear after the saturation of these preferential sites. In terms of crystallization of amorphous phase, it has previously been suggested that the initial nucleation occurred in the surface layer in amorphous solid water films and the growth front propagated into deep layers,[25] due to the higher mobility of molecules in the surface layer. Therefore, it is conceivable that MBI's initial nucleation presented in this study may start from the surface layer or the substrate interface shown in Figure 4.13b.

4.4 Conclusions

In summary, this work demonstrates that low-temperature physical vapor deposition in high vacuum is a viable method to fabricate polycrystalline MBI thin films which have preferred orientation along (110) plane and desired in-plane and out-of-plane polarization direction. This study also demonstrates the detailed process of the amorphous-to-crystalline phase transition in organic molecular ferroelectrics. The crystallization temperature of amorphous MBI films is around 287 K. The phase transformation details extracted from the *in situ* electrical measurements including, D-V_{app} loops, remanent polarization, resistance and capacitance provide insights into the anisothermal kinetics of

phase transition in MBI which has a very small activation energy of 0.21 eV. The evolution of ferroelectricity in organics can be naturally extended to other organic ferroelectric materials. The electrical properties and multiple fabrication methods for MBI molecules clearly demonstrate that organic ferroelectrics may provide alternative sources for piezoelectric and ferroelectric devices.

CHAPTER 5 SUMMARY

To conclude, we have discussed the importance of organic ferroelectrics and the phase transition process in the fabrication of organic ferroelectric thin films. This work has brought to attention the growth and characterization of two organic ferroelectric materials, croconic acid (CA) and 2-methylbenzimidazole (MBI). We have investigated the nucleation and growth behavior of croconic acid molecules under different substrate temperatures and the electric field. The nucleation behavior shows that the nucleation rate has a maximum at intermediate temperature, and the electric field shifts the maximum nucleation rate towards the lower temperature. The fabricated CA films have no large-scale ferroelectricity. We have also brought into light the amorphous-to-crystalline phase transition of ferroelectric MBI and its anisothermal kinetics of phase transformation.

Some of the more important conclusions of this work are as follows,

- The nucleation rate of CA clusters has a maximum at intermediate temperature, and the electric field shifts the maximum nucleation rate towards the lower temperature. An analysis using classical nucleation theory suggests that the electric field decreases sublimation temperature of the CA film, increases the wetting angle, and decreases the surface diffusion barrier.
- Low-temperature physical vapor deposition in high vacuum is a viable method to fabricate polycrystalline MBI thin films. The polycrystalline MBI films by low temperature PVD method have preferential (110) texture and desired out-of-plane and in-plane polarization directions.
- The ferroelectricity of MBI thin films emerges from the amorphous-to-crystalline

phase transition. The crystallization temperature for MBI thin films is around 287 K. An analysis of the anisothermal transformation kinetics reveals that the crystallization of MBI molecules has a very small activation energy of 0.21 eV.

Index of Symbols

Symbol	Meaning
a	Jump distance of an atom
A	The electrode area
A_{el}	The electrode area in QCM
$c(n,t)$	The transient concentration of clusters. n is the molecular number in a cluster.
C	Capacitance
C_{glass}	The capacitance contributed by the glass substrate in an IDE device
C_{film}	The capacitance contributed by the film in an IDE device
C_{vacuum}	The capacitance contributed by vacuum in an IDE device
$C(n)$	The equilibrium concentration of clusters.
C_0	The number of atoms per unit volume
C_1	The number of single atoms in the equilibrium system
C^*	The concentration of critical-sized nuclei
d_e	The equivalent diameter of a grain's projected area
d_{D}	Deflection distance
D	Electric displacement field
D_0	Initial electric displacement
D_m	Molecular dipole moment
D_r	The remanent displacement for a leaky capacitor

Symbol	Meaning
E	Electric field
E_a	The activation energy of the reaction
f	The fraction of transformed volume
Δf	The change in resonance frequency
f_0	The resonance frequency of the unperturbed quartz resonator
F	The contact force
F_d	The distribution function
F_q	The frequency constant of the crystal
ΔG	The difference of free energy for a cluster to nucleate
ΔG^*	The nucleation barrier
ΔG_m	The activation energy of atomic/molecular migration
ΔG_V	The difference between free energy of the mother phases and crystal phases per unit volume
h	Planck's constant
I	Steady-state nucleation rate
$J(n,t)$	The transient nucleation rate
k	The spring constant
k_0	Parameter related to nucleation rate
k_B	Boltzmann constant
k_c	A constant
k_T	Heating rate

Symbol	Meaning
k_V	The slope of a triangle waveform voltage
l	The mean free path of molecules in the gas
L_{V}	The latent heat from phase transition
Δm	The change in mass
n	The number of molecules for a cluster
n_d	The dimensionality of domain/grain growth, or the Avrami exponent
n_e	Extraordinary refraction index
n_o	Ordinary refraction index
N_0	The initial number of nucleation sites per unit volume
N_{A}	Avogadro's number
$N(t)$	The number of remaining nucleation sites at time t
N_{n0}	The number of preexisting nuclei
N_{NS}	The number of nonswitched regions
p	The electric polarization for one-dimensional growth of domains
P	Electric polarization
P_r	Remanent polarization
P_s	Spontaneous polarization
$P^h(z)$	The probability distribution function of grain heights
$P_r^d(T)$	The remanent polarization when temperature decreases
P_r'	Normalized remanent polarization

Symbol	Meaning
P'_{r0}	The maximum value among normalized remanent polarization
r	Radius of a spherical nucleus
r^*	Radius of the critical nucleus
R	Resistance
S_i	The area of the elementary region *i*
t	Time
t_0	The characteristic switching time
Δt	Time duration
T	Temperature
T_{f}	The end temperature of the crystallization process
T_{m}	The equilibrium gas-solid transition temperature
T_{max}	The temperature at the largest transition rate
T_{x}	Phase transition (such as crystallization, sublimation) temperature
ΔT	The difference between the actual temperature and the equilibrium phase transition temperature
v	A parameter signifying the decay rate of nucleation sites
v_{c}	The molar volume of the crystal phase
v_{g}	The volume occupied by one gaseous molecule
v_r	The transformed volume of one nucleus
v_n^+	The probability for the attachment of a molecule from the amorphous/gaseous phase to the surface of a crystal of size *n*.

Symbol	Meaning
v^{*+}	The attachment probability of atoms to the critical-sized nucleus
V	The total volume of the material
V_0	Initial voltage
V_{app}	Applied voltage
V_f	The volume occupied per formula unit
V^{α}	The volume of untransformed region
V^{β}	The volume of transformed region
V_e^{β}	The extended volume of transformed region
z	The height of the film/grains/scanner
z_0	The threshold height for identification of grains in AFM images
α	The angle between molecules and the surface,
η	The shape factor
θ	The wetting angle
λ	Height-diameter ratio
λ_f	A frequency factor
λ_n	The aspect ratio
$\Delta\mu$	Nucleation driving force
ξ_i	The time within duration Δt_i
ρ_q	The quartz density
σ	The interfacial energy, or surface energy.

Symbol	Meaning
σ_s	The surface energy of the substrate
σ_i	The surface energy of the substrate–nucleus interface
τ	Relaxation time
τ_0	a temperature-independent pre-exponential factor
τ_i	The waiting time for the elementary region i
τ_N	Induction time for nucleation
τ_t	The period of the triangle-wave voltage
Υ	Isotropic growth rate of one dimension of nuclei
Υ_i	Anisotropic growth rate. $i = 1, 2, 3$
$\phi(\theta)$	The wetting function
ψ	The angle between crystal optic axis and the polarizer axis
ω	A factor related to atomic vibration frequency and the area of the critical nucleus

Bibliography

1. Ye, H. Y. *et al.* Metal-free three-dimensional perovskite ferroelectrics. *Science (80-.).* **361**, 151–155 (2018).
2. Tayi, A. S., Kaeser, A., Matsumoto, M., Aida, T. & Stupp, S. I. Supramolecular ferroelectrics. *Nat. Chem.* **7**, 281–294 (2015).
3. Kobayashi, K. *et al.* Structure-property relationship of supramolecular ferroelectric [H-66dmbp][Hca] accompanied by high polarization, competing structural phases, and polymorphs. *Chem. - A Eur. J.* **20**, 17515–17522 (2014).
4. Sachio Horiuchi, Y. T. Organic ferroelectrics. 357–366 doi:10.1038/nmat2137
5. Horiuchi, S. *et al.* Above-room-temperature ferroelectricity in a single-component molecular crystal. *Nature* **463**, 789–792 (2010).
6. Horiuchi, S. *et al.* Above-room-temperature ferroelectricity and antiferroelectricity in benzimidazoles. *Nat. Commun.* **3**, (2012).
7. Horiuchi, S., Kumai, R. & Tokura, Y. Hydrogen-bonding molecular chains for high-temperature ferroelectricity. *Adv. Mater.* **23**, 2098–2103 (2011).
8. Íñiguez, J., Zubko, P., Luk'yanchuk, I. & Cano, A. Ferroelectric negative capacitance. *Nat. Rev. Mater.* **4**, 243–256 (2019).
9. Lau, K., Liu, Y., Chen, H. & Withers, R. L. Effect of annealing temperature on the morphology and piezoresponse characterisation of poly(vinylidene fluoride-trifluoroethylene) films via Scanning Probe Microscopy. *Adv. Condens. Matter Phys.* **2013**, (2013).
10. Zhai, H. *et al.* In situ polarization and dielectric property measurements of

Pb(Zr0.52Ti0.48)O3 ferroelectric nanocrystals. *Heliyon* **3**, e00313 (2017).

11. Horiuchi, S., Kobayashi, K., Kumai, R. & Ishibashi, S. Proton tautomerism for strong polarization switching. *Nat. Commun.* **8**, (2017).
12. Tokura, Y., Okamoto, H., Koda, T., Mitani, T. & Saito, G. Nonlinear electric transport and switching phenomenon in the mixed-stack charge-transfer crystal tetrathiafulvalene-p-chloranil. *Phys. Rev. B* **38**, 2215–2218 (1988).
13. Mai, M., Ke, S., Lin, P. & Zeng, X. Ferroelectric Polymer Thin Films for Organic Electronics. **2015**, (2015).
14. Savage, A. & Miller, R. C. Temperature dependence of the velocity of sidewise 180° domain-wall motion in BaTiO3. *J. Appl. Phys.* **31**, 1546–1549 (1960).
15. Tagantsev, A. K., Stolichnov, I., Setter, N., Cross, J. S. & Tsukada, M. Non-Kolmogorov-Avrami switching kinetics in ferroelectric thin films. *Phys. Rev. B - Condens. Matter Mater. Phys.* **66**, 1–6 (2002).
16. Hu, W. J. *et al.* Universal ferroelectric switching dynamics of vinylidene fluoride-trifluoroethylene copolymer films. *Sci. Rep.* **4**, 1–8 (2014).
17. So, Y. W., Kim, D. J., Noh, T. W., Yoon, J. G. & Song, T. K. Polarization switching kinetics of epitaxial Pb(Zr0.4Ti 0.6)O3 thin films. *Appl. Phys. Lett.* **86**, 1–3 (2005).
18. Jo, J. Y. *et al.* Domain switching kinetics in disordered ferroelectric thin films. *Phys. Rev. Lett.* **99**, 1–4 (2007).
19. Love, J. C., Estroff, L. A., Kriebel, J. K., Nuzzo, R. G. & Whitesides, G. M. *Self-assembled monolayers of thiolates on metals as a form of nanotechnology*. *Chemical Reviews* **105**, (2005).

20. Elemans, J. A. A. W., Lei, S. & De Feyter, S. Molecular and supramolecular networks on surfaces: From two-dimensional crystal engineering to reactivity. *Angew. Chemie - Int. Ed.* **48**, 7298–7332 (2009).

21. James, P. F. Kinetics of crystal nucleation in lithium silicate glasses. *Phys. Chem. Glas.* **15**, 95–105 (1974).

22. Sreekumar, R. & Padmakumar, R. Crystallization of Amorphous Alloys. *Synth. Commun.* **27**, 777–780 (1997).

23. Jenniskens, P. & Blake, D. F. Crystallization of Amorphous Water Ice in the Solar System. *Astrophys. J.* **473**, 1104–1113 (1996).

24. Porter, D. A., Easterling, K. E. & Sherif, M. Y. *Phase transformations in metals and alloys*. *Phase Transformations in Metals and Alloys, Third Edition* (Routledge, 2009).

25. Yuan, C., Smith, R. S. & Kay, B. D. Surface and bulk crystallization of amorphous solid water films: Confirmation of "top-down" crystallization. *Surf. Sci.* **652**, 350–354 (2016).

26. Jiang, Y. *et al.* Growth of organic crystals via attachment and transformation of nanoscopic precursors. *Nat. Commun.* **8**, (2017).

27. Kashchiev, D. Solution of the non-steady state problem in nucleation kinetics. *Surf. Sci.* **14**, 209–220 (1969).

28. Zeldovich, Y. B. On the theory of new phase formation: cavitation. *Acta Physicochem. USSR* **18**, 1 (1943).

29. Krikorian, E. & Sneed, R. J. Nucleation, growth and transformation of amorphous and crystalline solids condensing from the gas phase. *Astrophys. Space Sci.* **65**,

129–154 (1979).

30. Miller, R. C. & Savage, A. Motion of 180°domain walls in metal electroded barium titanate crystals as a function of electric field and sample thickness. *J. Appl. Phys.* **31**, 662–669 (1960).

31. Merz, W. J. Domain formation and domain wall motions in ferroelectric BaTiO3 single crystals. *Phys. Rev.* **95**, 690–698 (1954).

32. Christian, J. W. *The Theory of Transformations in Metals and Alloys*. (Elsevier Science, 2002).

33. Avrami, M. Kinetics of phase change. II Transformation-time relations for random distribution of nuclei. *J. Chem. Phys.* **8**, 212–224 (1940).

34. Te, S. & Alloys, T. The Mechanism of the Amorphous-to-Crystalline Transition. **36**, 1451–1459 (2000).

35. Parsajoo, C., Kauffmann, J.-M. & Elkaoutit, M. *Biosensors for drug testing and discovery*. *Biosensors for Medical Applications* (Elsevier Masson SAS., 2012).

36. Prater, C. B., Maivald, P. G., Kjoller, K. J. & Heaton, M. G. Probing nano-scale forces with the atomic force microscope. *R&D Mag.* **37**, 63 (1995).

37. Geisse, N. A. AFM and combined optical techniques. *Mater. Today* **12**, 40–45 (2009).

38. Surtchev, M., Magonov, S., Zayats, S. & Wall, M. The Characterization of Polymer Blends Using a Combined Raman-AFM Microscope. *Appl. notes 52664* 2–5

39. Keller, S., Mouaziz, S., Boero, G. & Brugger, J. Microscopic four-point probe based on SU-8 cantilevers. *Rev. Sci. Instrum.* **76**, 1–4 (2005).

40. Kanagawa, T. *et al.* Anisotropy in Conductance of a Quasi-One-Dimensional Metallic Surface State Measured by a Square Micro-Four-Point Probe Method. *Phys. Rev. Lett.* **91**, 1–4 (2003).

41. Cui, W. *et al.* An in situ electrical transport measurement system under ultra-high vacuum. *Rev. Sci. Instrum.* **91**, (2020).

42. Das, S. C., Shahee, A., Lalla, N. P. & Shripathi, T. A simple and low cost Sawyer-Tower ferro-electric loop tracer with variable frequency and compensation circuit. *54th DAE Solid State Phys. Symp. Vol.* **54**, 3–4 (2009).

43. Stewart, M., Cain, M. G. & Hall, D. Ferroelectric Hysteresis Measurement & Analysis. *NPL Rep. C.* 1–57 (1999).

44. Fukunaga, M. & Noda, Y. New technique for measuring ferroelectric and antiferroelectric hysteresis loops. *J. Phys. Soc. Japan* **77**, 4–8 (2008).

45. Fukunaga, M. & Noda, Y. Improvement of the double-wave method for ferroelectric hysteresis loops and its application to multiferroic euMn2O5. *J. Korean Phys. Soc.* **55**, 888–892 (2009).

46. Hall, D. B., Underhill, P. & Torkelson, J. M. Spin coating of thin and ultrathin polymer films. *Polym. Eng. Sci.* **38**, 2039–2045 (1998).

47. O'Malley, S. M. *et al.* Matrix-assisted pulsed laser deposition of croconic acid, a diprotic organic ferroelectric. *Appl. Phys. A Mater. Sci. Process.* **105**, 635–641 (2011).

48. Horiuchi, S. & Tokura, Y. Organic ferroelectrics. *Nat. Mater.* **7**, 357–366 (2008).

49. Usher, B. F. The contribution of kinetic nucleation theories to studies of Volmer-Weber thin film growth. *Appl. Surf. Sci.* **22**–**23**, 506–511 (1985).

50. Hu, L. *et al.* Space-Charge-Stabilized Ferroelectric Polarization in Self-Oriented Croconic Acid Films. *Adv. Funct. Mater.* **28**, 1–9 (2018).

51. Jiang, X. *et al.* Room temperature ferroelectricity in continuous croconic acid thin films. *Appl. Phys. Lett.* **109**, 102902 (2016).

52. Liu, X., Cai, Z., Liu, S., Peng, J. & Zhu, M. Effect of roughness on electrical contact performance of electronic components. *Microelectron. Reliab.* **74**, 100–109 (2017).

53. Jo, P. S. *et al.* Controlled topology of block copolymer gate insulators by selective etching of cylindrical microdomains in pentacene organic thin film transistors. *Adv. Funct. Mater.* **18**, 1202–1211 (2008).

54. Zettlemoyer, A. C. *Nucleation*. (Marcel Dekker, 1969).

55. Guo, H. *et al.* Growth diagram of La0.7Sr0.3MnO3 thin films using pulsed laser deposition. *J. Appl. Phys.* **113**, 234301 (2013).

56. Zhang, T. H. & Liu, X. Y. Nucleation: What happens at the initial stage? *Angew. Chemie - Int. Ed.* **48**, 1308–1312 (2009).

57. Sakai, M., Iizuka, M., Nakamura, M. & Kudo, K. Thin film transistors with oriented copper phthalocyanine crystals fabricated by physical vapor deposition under DC electric field. *Jpn. J. Appl. Phys.* **43**, 2362–2365 (2004).

58. Parmar, D. S. & Jalaluddin, A. K. Electric-field-induced nucleation: A phenomenon used for determining the boundary of stability of liquids. *J. Phys. D. Appl. Phys.* **8**, 971–982 (1975).

59. He, F. & Hopke, P. K. Experimental study of ion-induced nucleation by radon decay. *J. Chem. Phys.* **99**, 9972–9978 (1993).

60. Saban, K. V, Thomas, J. & Varghese, G. The influence of electric field on the nucleation of NaCl crystals. *Indian J. Phys.* **76**, 355–359 (2002).

61. Braga, D., Maini, L. & Grepioni, F. Crystallization from hydrochloric acid affords the solid-state structure of croconic acid (175 years after its discovery) and a novel hydrogen-bonded network. *CrystEngComm* **3**, 27 (2004).

62. Zhang, Z. *et al.* Redox reaction induced Ostwald ripening for size- and shape-focusing of palladium nanocrystals. *Chem. Sci.* **6**, 5197–5203 (2015).

63. Nanev, C. N. *Theory of Nucleation*. *Handbook of Crystal Growth: Second Edition* **1**, (Elsevier B.V., 2014).

64. James, P. F. Kinetics of crystal nucleation in lithium silicate-glasses. *Phys. Chem. Glas.* **15**, 95–105 (1974).

65. Kashchiev, D. *Nucleation*. (Elsevier Science, 2000).

66. Markov, I. V. *Crystal Growth For Beginners: Fundamentals Of Nucleation, Crystal Growth And Epitaxy (2nd Edition)*. (World Scientific Publishing Company, 2003).

67. Tabor, D. *Gases, liquids and solids: and other states of matter*. (Cambridge University Press, 1991).

68. Hooper, J., Kunkel, D. A., Zurek, E. & Enders, A. Interplay between Hydrogen Bonding, Epitaxy, and Charge Transfer in the Self-Assembly of Croconic Acid on Au(111) and Ag(111). *J. Phys. Chem. C* **119**, 26429–26437 (2015).

69. Bateni, A. *et al.* Effect of electric fields on contact angle and surface tension of drops. *J. Colloid Interface Sci.* **283**, 215–222 (2005).

70. Kua, J., Lauhon, L. J., Ho, W. & Goddard, W. A. Direct comparisons of rates for

low temperature diffusion of hydrogen and deuterium on Cu(001) from quantum mechanical calculations and scanning tunneling microscopy experiments. *J. Chem. Phys.* **115**, 5620–5624 (2001).

71. Ranea, V. A. *et al.* Water dimer diffusion on Pd{111} assisted by an H-bond donor-acceptor tunneling exchange. *Phys. Rev. Lett.* **92**, 1–4 (2004).
72. De Knoop, L. *et al.* Electric-field-controlled reversible order-disorder switching of a metal tip surface. *Phys. Rev. Mater.* **2**, 1–6 (2018).
73. Alexander, L. F. & Radacsi, N. Application of electric fields for controlling crystallization. *CrystEngComm* **21**, 5014–5031 (2019).
74. Ghosh, M. Nucleation of charged droplets; An ion-atmosphere model. *RSC Adv.* **4**, 45275–45285 (2014).
75. Mandal, T., Garg, A. & Deepak. Thin film transistors fabricated by evaporating pentacene under electric field. *J. Appl. Phys.* **114**, (2013).
76. Mohapatra, S. *et al.* Robust ferroelectric properties of organic croconic acid films grown on spintronically relevant substrates. *Mater. Adv.* **1**, 415–420 (2020).
77. Noda, Y. *et al.* Few-Volt Operation of Printed Organic Ferroelectric Capacitor. *Adv. Mater.* **27**, 6475–6481 (2015).
78. Balashova, E. V., Krichevtsov, B. B., Svinarev, F. B., Zaitseva, N. V. & Pankova, G. A. Structural and dielectric properties of organic ferroelectric 2-methylbenzimidazole. *J. Surf. Investig.* **12**, 233–239 (2018).
79. Yuan, Y., Jiang, X., Poddar, S. & Xu, X. Electric-field assisted nucleation processes of croconic acid films. *CrystEngComm* (2019).
80. Igreja, R. & Dias, C. J. Analytical evaluation of the interdigital electrodes

capacitance for a multi-layered structure. *Sensors Actuators, A Phys.* **112**, 291–301 (2004).

81. Igreja, R. & Dias, C. J. Dielectric response of interdigital chemocapacitors: The role of the sensitive layer thickness. *Sensors Actuators, B Chem.* **115**, 69–78 (2006).

82. Mazurin, O. V. Problems of compatibility of the values of glass transition temperatures published in the world literature. *Glas. Phys. Chem.* **33**, 22–36 (2007).

83. Kim, J. H., Jang, J. & Zin, W. C. Thickness dependence of the glass transition temperature in thin polymer films. *Langmuir* **17**, 2703–2710 (2001).

84. Moynihan, C. T., Easteal, A. J., Wilder, J. & Tucker, J. Dependence of the glass transition temperature on heating and cooling rate. *J. Phys. Chem.* **78**, 2673–2677 (1974).

85. Lee, J. N., Lee, B. J., Moon, D. G. & Ahn, B. T. Effect of deposition temperature on the crystallization mechanism of amorphous silicon films on glass. *Japanese J. Appl. Physics, Part 1 Regul. Pap. Short Notes Rev. Pap.* **36**, 6862–6866 (1997).

86. Fryer, D. S. *et al.* Dependence of the glass transition temperature of polymer films on interfacial energy and thickness. *Macromolecules* **34**, 5627–5634 (2001).

87. Paquin, F., Rivnay, J., Salleo, A., Stingelin, N. & Silva, C. Multi-phase semicrystalline microstructures drive exciton dissociation in neat plastic semiconductors. *J. Mater. Chem. C* **3**, 10715–10722 (2015).

88. Svinarev, F. B., Balashova, E. V. & Krichevtsov, B. B. Dielectric properties of self-assembled spherulite films of organic ferroelectric 2-methylbenzimidazole.

Ferroelectrics **543**, 167–174 (2019).

89. Chandel, N., Imran, M. M. A. & Mehta, N. Comprehensive studies of temperature and frequency dependent dielectric and a.c. conducting parameters in third generation multi-component glasses. *RSC Adv.* **8**, 25468–25479 (2018).

90. Balashova, E. V. *et al.* Polarization switching, dielectric, structural and elastic properties of 2-Methylbenzimidazole crystals and films. *Ferroelectrics* **538**, 74–82 (2019).

91. Shtukenberg, A. G., Punin, Y. O., Gunn, E. & Kahr, B. Spherulites. *Chem. Rev.* **112**, 1805–1838 (2012).

92. Park, S. W. *et al.* Amorphous-to-crystalline phase transformation of thin film rubrene. *J. Phys. Chem. B* **114**, 5661–5665 (2010).

93. Einstein, T. L. *Equilibrium Shape of Crystals*. *Handbook of Crystal Growth: Second Edition* **1**, (2014).

94. Louis, E. & García-Cordovilla, C. kinetics of anisothermal phase transformations. *J. Appl. Phys.* **57**, 2975–2976 (1985).

95. Tien, T., Ottaviani, G. & Tu, K. N. Temperature dependence of structural and electrical properties of Ta-Si thin alloy films. *J. Appl. Phys.* **54**, 7047–7057 (1983).